Dual-Band Power and Communication Antennas for Wireless Brain-Computer Interfaces

Apoorva Sharma

A dissertation
submitted in partial fulfillment of the
requirement for the degree of

Doctor of Philosophy

University of Washington
2019

Reading Committee:
Matthew S. Reynolds, Chair
Joshua Smith
Robert Darling

Program Authorized to Offer Degree:
Electrical and Computer Engineering

University of Washington

Abstract

Dual-band power and communication antennas for wireless brain-computer interfaces

Apoorva Sharma

Chair of the Supervisory Committee:
Matthew S. Reynolds
Department of Electrical and Computer Engineering

Implanted biomedical devices such as wireless brain computer interfaces (BCIs) for neural recording and stimulation face two key challenges: (1) remaining powered over a long duration and (2) communicating with an external system with sufficient bandwidth in an unconstrained environment without data dropouts. A viable solution to solve these problems is to supply power to the BCI device via inductive coupling at the high-frequency (HF) band (13.5 MHz) and to have data communication at the ultrahigh-frequency (UHF) band (902–928 MHz). To fulfill these requirements, design of dual-band (HF and UHF) antennas for BCI and external devices are needed. Designing HF and UHF antennas together in a small printed circuit board (PCB) size (area of ≈ 0.002 m^2) is a challenging task due to (1) the relatively long wavelengths of HF (≈ 22 m) and UHF bands (≈ 0.3 m), (2) the desire to minimize the specific absorption rate (SAR), (3) the wide bandwidth required in the communication band, and (4) the need to minimize unwanted interference between the power and communication systems.

This thesis presents two BCI antenna systems: (1) a novel electrically-small dual-band implant antenna (27 mm diameter) to be embedded in the dura layer (≈ 1 cm below the skin's surface) with an external antenna (85 mm diameter) in proximity (few millimeters) to the skin's surface, and (2) a dual-band BCI antenna (55 mm diameter) designed to be installed on the top of non-human primate's (NHP) head, with an external antenna located inside the top wall of the housing cage. The antennas were tested initially using a saline tissue proxy. Later, the implant antenna was tested inside the chicken muscle. With an implant depth of 11 mm and an air gap of 5 mm, the power link has a 17 % measured power transfer efficiency in the HF band, inclusive of matching component losses, and the UHF communication link has 38 dB insertion loss over the 902–928 MHz band using saline solution. In chicken muscle UHF communication link has 7.5 dB lower insertion loss as compared to saline solution.

Head-stage antennas designed for large NHPs were tested inside a metal housing cage. Wireless communication inside the cage is a challenging task as the metal walls form a reverberating cavity, creating dense multipath, resulting in many deep nulls that impair the communication channel. Later in the thesis, *in-vivo* recordings were performed on an anesthetized pigtail macaque (Macaca nemestrina), to validate the performance of wireless backscatter uplinks. The monostatic backscatter data uplink using ceramic BCI antenna, designed for NHPs, was successfully validated inside the cage, exhibiting 0 % packet error ratio (PER) for 23 of 25 measurement location points, at a data rate of 6.25 Mbps, and PER greater than 5 % at two measurement location points due to the presence of deep nulls inside the cage. These experimental results showed high data rate communication with low PER, in the presence of significant multipath. In this work, the highest data rate achieved to uplink the recorded neural signals of an anesthetized pigtail macaque to the external system from the proposed head-stage antenna system is 25 Mbps.

The success of the antenna designs presented in this thesis open an opportunity to

utilize wireless BCI systems in the future for human clinical applications (for example, in neural-recording and deep-brain stimulation for people with Parkinson's disease and other neurological disorders), and for neuroscience research on awake, freely moving animals.

TABLE OF CONTENTS

LIST OF TABLES

TABLE **Page**

LIST OF FIGURES

FIGURE **Page**

Acknowledgment

The present thesis is the result of a collective effort of many people involved at different stages. I was inspired by their kind cooperation and support. I would like to express my gratitude to all of them. First and foremost, I take this opportunity to express my sincere gratitude to my advisor Prof. Matt Reynolds for giving me the opportunity to work on exciting projects all the time, from biomedical devices to millimeter wave imaging to RFID and long-range communications using transmission line. His scholarly advice helped me at each and every stage of the thesis. I am thankful to Electrical and Computer Engineering Department, University of Washington for acknowledging me from time to time and for giving me the chance to present my work at several ocassions.

The project described in the thesis was supported in part by Award Number EEC-1028725 from the National Science Foundation. The content of this thesis and the idea behind the antenna designs are solely my responsibility and do not necessarily represent the official views of the National Science Foundation. I would also like to thank Profs. Eberhard E. Fetz, Steve I. Perlmutter, Azadeh Yazdan-Shahmorad, and the team at the Washington National Primate Research Center for providing sample neural recordings and access to the NHP cage. Thanks to everyone in my research lab, Andreas Pedross-Engel, Daniel Arnitz, Claire Watts, Alexandra Pike, Alex Hoang, James Rosenthal, Sandamalli Devadithya, Eleftherios Kampianakis, Jose Arenas, Xiaojie Fu, and Thang Phu. I feel a deep sense of gratitude to my husband Varun Chawla without whose emotional and unwavering support it would not have been possible to finish this journey. Having a newborn baby in the last year of my Ph.D. with multiple things going on like a Google internship, completing experiments, writing the thesis was really tough but I finally made it through with the support of my husband, parents, sister, and friends.

CHAPTER 1

INTRODUCTION

1.1 Motivation

With the technological advancements that have been made in the area of electrophysiological recording of single cortical neurons in awake monkeys [8], a new understanding of neuronal control of muscular movements has developed. As a result, neuroscientists have been able to relate neuronal firing rates to various movement parameters [9, 10, 11, 12] and measure the extra-cellular activity of individual neurons and neural ensembles. These changes have led to the development of neural prosthetics referred to as brain-computer interfaces (BCIs). In BCI, neural signals are measured by a signal acquisition system on the test subject (e.g. a non-human primate (NHP)) and then transferred to an external computer where the neural data is analyzed and translated into commands for external activities like control of a robotic limb. BCI devices have several applications in biomedical industry, such as: (1) short-term epilepsy prognosis using electroencephalography (EEG) [13], (2) classifying expressions of sadness and happiness [14], (3) controlling wheelchairs based on neural activity [15], (4) controlling robotic mechanical limbs to help people with paralysis or amputations [16], and (5) monitoring the brain development of humans and animals [17, 18]. BCIs can also enable the future paradigms of electronic telepathy by enabling humans to control digital devices with their thoughts, and, perhaps eventually, allowing people to perform brain-to-brain communication [19].

1.2 Need for wireless BCI systems

In conventional BCI systems, wires are used to connect the BCI device to an external computer for power and data transfer. For such devices the relationship between neural activity and physical behavior can only be achieved by constraining the movement of the subject, which therefore limits the long-term functionality/usability of such devices. There are other several issues with wired BCI systems that demand the design of wireless alternatives:

- Risk of infection inside the brain [20],
- Limited to laboratory experiments and are not suitable for everyday life applications [17],
- Time-consuming setups and adjustments that cannot be made easily by the user [17],
- Mechanical problems can injure animals and reduce longevity [21],
- The wiring itself can produce misleading correlations between movement parameters and neural activities [9].

Antennas are the most critical aspect of wireless BCI systems and are discussed in this work.

1.3 Objectives

To enable fundamental neuroscience research on awake, freely moving animals, BCIs must be able to wirelessly stream neural data across multiple channels for several days in an unconstrained environment without data drop-outs [22, 23]. A BCI system should also have the ability to charge through wirelessly eliminating the need for heavy and bulky batteries to provide energy [24, 25]. The development of wireless BCI systems will hopefully lead to an unbiased understanding of the relationship between neural activity and movement through continuous recording from freely-moving animals. These wireless BCI requirements drive the design of biomedical antennas.

In this thesis, we explored following two real-world environments where biomedical antennas can be used to improve device performance : (1) short-range communication/WPT between implanted and the external devices, and (2) communication/WPT between the external device and the head-mounted BCI device designed for NHPs. The proposed BCI systems contain high frequency (HF) loop antenna designed for WPT based on inductive coupling and ultra high frequency (UHF) antenna for backscatter communication.

1.3.1 Why HF band for WPT?

For WPT the optimal choice of operating frequency in an implanted device is a function of the size of the implanted system as well as the electromagnetic (EM) properties of the tissue in which it is embedded [26, 27]. For neural recording and stimulation in larger rodents or primates, with implants $\approx 1\text{cm}^3$, transferring WPT in the HF spectrum (e.g., 13.56 MHz) represents a good compromise between antenna size and efficiency. In this work, WPT antennas are designed at 13.5 MHz. Another advantage of using the HF spectrum is of long penetration depth resulting in minimal EM absorption in biological tissues [28].

1.3.2 Why UHF band for data communication?

Although it would be convenient to use the HF spectrum for data communication too. The HF spectrum cannot be used for efficient communication because of its limited 14 KHz industrial, scientific and medical (ISM) bandwidth. In this work, the UHF band (902–928 MHz) is utilized for data communication based on backscatter technique, instead of conventional radio since backscatter devices do not require power hungry active RF amplifiers and oscillators to generate a communication carrier wave (CW). This technique allows small-form-factor systems with high data rates (>96 Mbps) [29] at orders of magnitude less power consumption when compared to conventional, commercially-available radio standards like Bluetooth Low Energy and WiFi (IEEE 802.11n) [30]. In backscatter-based devices, a time-varying impedance is applied to the antenna, which modulates the amplitude and phase of the incident CW, and scatters the modulated signal. Other communication alternatives exist (e.g., ultrasonic [31] and ultra-wideband [32]), but the high data rate, simplicity, and small size of backscatter communication systems make them an attractive choice for wireless BCIs.

1.4 Short-range WPT and communication between implant and external systems

In this work, an implant antenna is designed to be embedded in the dura layer and an external antenna capable of communicating with the implant within a distance of a few centimeters. The antenna can be fit in a cap which the user can wear on their head such that the external antenna is in close proximity to the head's skin. This kind of setup enables the use of BCI systems for everyday life applications, outside the laboratory environment as shown in Fig. 1.1 (a).

The practicability of implanted BCI systems for long distance WPT and communication (as shown in Fig. 1.1 (b)), where the external antenna is located at a distance of a few meters from the implant antenna, is unknown because of the complexity in link budget. This work is suggested for future work and is not covered in this thesis.

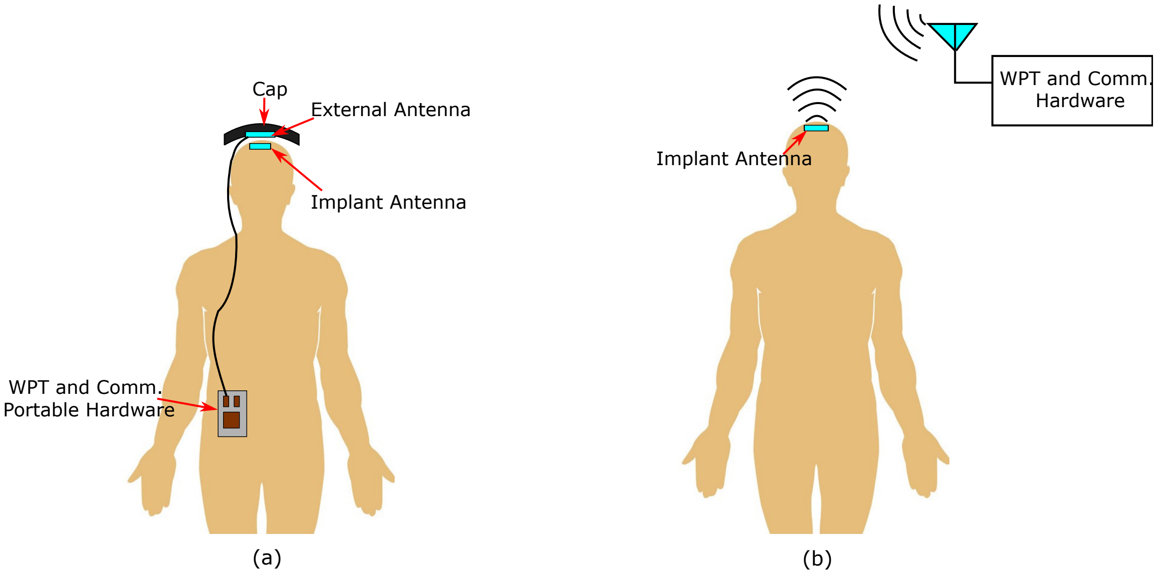

Figure 1.1: Two possible applications of implanted wireless BCI systems. (a) Short-range WPT and communication. (b) Long range WPT and communication.

1.4.1 Dual-band implantable antenna challenges

Implanted dual-band (HF and UHF) antennas are challenging to design for many reasons:

- **Need to make compact** : Typically, implanted devices [33, 34] have volumes on the order of a few mm^3 to a few cm^3 limited by allowable tissue displacement, and a power budget on the order of μW to mW limited by tissue heating. Long wavelengths at HF ($\approx$ 22 m) and UHF bands ($\approx$ 0.3 m) complicate the design of co-planar HF and UHF antennas in a small PCB size (volume $\approx$ few cm^3).
- **Need to maximize data** : The trade-off for designing electrically-small antennas is poor antenna radiation efficiency and narrow bandwidth. However, a wide bandwidth

would be required to support high data rates and to incorporate more recording or stimulation channels. In addition to that, EM wave absorption in biological tissues results in reduced coupling efficiency between external and implanted devices.

- **Need to minimize heat** : The desire to minimize specific absorption rate (SAR) and accompanying tissue heating from EM absorption, to prevent tissue damage. In the US, wireless BCI systems need to be designed for SAR below 1.6 W/Kg measured in 1 gram of tissue sample for human exposure [35].
- **Need to minimize signal interference** : Port-to-port mutual coupling between the co-planar WPT and communication antennas should be minimized to prevent unwanted interference between the power and communication signals. Additionally, biological signals of interest often have very low amplitude (e.g. neural spikes are $\approx$ <100 μV), so the antennas should not interfere with sensitive measurement electronics.
- **Need to protect** : Encapsulation is needed for the protection of tissues from corrosion and impurities. A layer of encapsulation can change antenna properties like resonant frequency, and bandwidth. Hence, it is essential to model the encapsulation layer while designing the antenna for simulations.

1.5 WPT and communication inside a metal housing cage

Another BCI application proposed in this thesis is to provide efficient wireless communication for enabling neuroscience research on awake, freely moving large NHPs inside a metal housing cage. The block diagram is shown in Fig. 1.2.

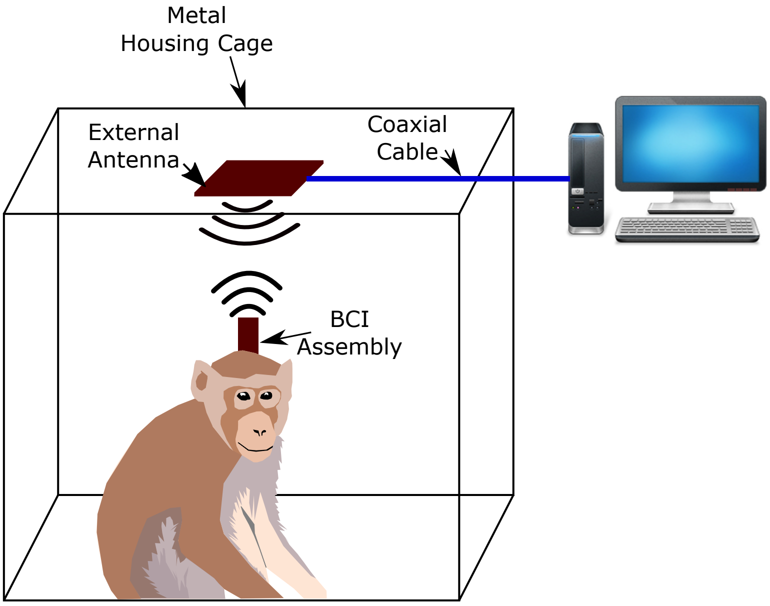

Figure 1.2: Block diagram of wireless BCI system on awake, freely moving animals. *Desktop image is licensed under CC CC BY-NC-ND and monkey image credit to James Rosenthal.*

1.5.1 Challenges with BCI systems in metal housing cage due to reverberant cavity

Enabling communication inside a metal housing cage is a challenging task as the metal walls form a reverberating cavity in which EM waves bounce back and forth, creating dense multipath fading. This phenomenon results in many deep nulls in the communication channel which can destructively interfere with the backscattered signal. There is extensive literature on characterizing multipath channels in urban, indoor office, and industrial environments [36, 37, 38, 39]. To the best of my knowledge, experiments performed in this work, to characterize the channel transfer function for UHF band inside the commonly utilized NHP housing cage made up of metal grids, is the first work of its kind.

1.6 Steps for designing wireless BCI antennas

In this thesis, BCI antennas were designed using the following methodology:

- Estimation of the material properties of biological tissue or tissue proxy using statistical models like Debye or Cole-Cole models,
- Creation of a numerical phantom in EM simulation software with calculated dielectric properties for each biological layer,
- Antenna design based on the requirements of BCI systems,
- Optimization of antenna dimensions using local/global algorithms, e.g., genetic algorithm,
- EM simulations for the estimation of bandwidth, insertion loss, power transfer efficiency, and SAR,
- Fabrication and encapsulation,
- Testing of the antenna systems and *in-vivo* neural recordings.

1.7 State of the art

1.7.1 Literature on WPT antennas

In the past, many researchers have worked separately on powering biomedical devices based on WPT via inductive coupling as shown in Table 1.1 and wireless BCI communication as shown in Table 1.2, and in [40]. Literature review suggests that, WPT can be performed for frequency ranges from few MHz to GHz.

The antenna design proposed in [41] designed at 0.8 MHz, is most efficient but has the largest size. The design mentioned in [46] at frequency 400 MHz has the smallest area with a low WPT efficiency of -27 dB. The antenna design mentioned in [26] at 13.5 MHz has a small

Table 1.1: Literature on biomedical antennas for WPT

Reference	Center Frequency (MHz)	Implant size (mm)	Application	Gap between. external & implant antennas (mm)	Link efficiency (dB)
Sharma [1]	**13.5 & 915**	**Board diam. 25**	**WPT/ Backscatter comm.**	**15**	**-7.6 dB**
Knecht [41]	0.8	diam. 70	WPT	20	-0.2
Jow [42]	1	diam. 20	WPT	10	-3.85
Jow [42]	5	diam. 20	WPT	10	-0.7
Zargham [26]	13.5	diam. 10	WPT	10	-1.4
Kiani [43]	13.5	diam. 10	WPT	5	-8.5
Zargham [44]	160	2 × 2.18	WPT	10	-20
Björninen [45]	400	6.5 × 6.5	WPT	16	-16
Song [46]	400	1 × 1 × 1	WPT	10	-27
Driscol [47]	1000	2 × 2	WPT	15	-31

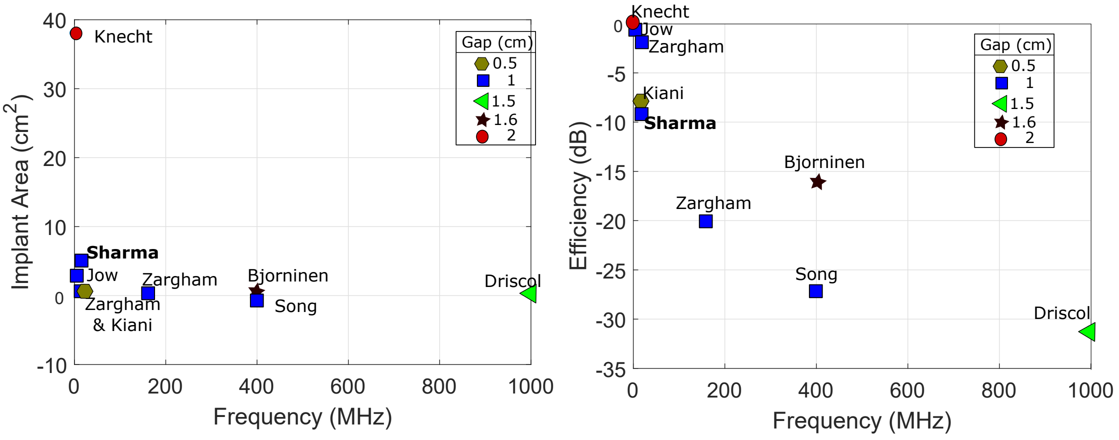

Figure 1.3: Comparison of WPT antennas based on the references mentioned in Table 1.1. Design mentioned in Sharma [1] has small HF antenna size as well as good efficiency.

antenna diameter of 10 mm, and has an efficiency of -1.4 dB, for an air gap of 10 mm. The dual-band implant antenna proposed in this work [1], is an ideal balance of small size and good efficiency. From Table 1.1 and Fig. 1.3, it can be concluded that the antenna's efficiency largely depends on the coil area, the frequency, and the gap between external and implant antennas. As a result, it is challenging to design small antennas for WPT with good efficiency at low-frequency bands. The disadvantage of designing antennas at higher frequency bands is that the WPT link efficiency decreases with the increase in frequency due to the increased path loss and increased EM absorption in biological tissues.

Table 1.2: Literature on biomedical antennas for wireless communication

Reference	**Center Frequency (MHz)**	**Implant size (mm)**	**Application**	**Separation gap (mm)**	$\lvert S_{21} \rvert$ **(dB)**
Sharma [1]	**13.5 & 915**	**Board Diam. 25**	**WPT/ Backscatter comm.**	**15**	**-30 dB @ 915 MHz**
Bahrami [48]	2450 & 6850	10 × 9	Comm.	4	-20 dB @ 2450 MHz -38 dB @ 6850 MHz
Liu [49]	402 & 2400	22 × 23 × 1.27	Comm.	50	-32 dB @ 2400 MHz -34 dB @ 402 MHz
Duan [50]	403 & 2450	13.4 × 16 × 0.83	Comm.	20	-30 @ 403 MHz & -22 @ 2450 MHz
Song [46]	950	1 × 1 × 1	Backscatter comm.	3	-25 @ 915 MHz

1.7.2 Literature on implantable antennas for data communication

The literature review on implantable antennas for wireless communication is shown in Table 1.2. For communication, the medical device radiocommunications service (MICS) 402–405 MHz band and the 2.4 GHz ISM band are common choices in the literature. However, with the constrained bandwidth, it becomes increasingly more difficult to send high data rates. The 2.4 GHz band has higher ISM bandwidth of 100 MHz but suffers from higher path loss resulting in lower link efficiency compared to the MICS band. In this thesis, the UHF band (902–928 MHz) is chosen for communication because of the following reasons: (1) wider bandwidth (26 MHz) as compared to MICS band, (2) capable of supporting data rates from tens to hundreds of Mbps, and (3) lower path loss compared to 2.4 GHz.

Table 1.3: Literature on biomedical antennas for WPT and communication

Reference	**Center Freq. (MHz)**	**Implant size (mm)**	**Application**	**Separation gap (mm)**	**WPT Link efficiency (dB)**	**Comm. Data rate (Mbps)**
Sharma [1]	**13.5 & 915**	**Diam. 25**	**WPT/ Backscatter comm.**	**15**	**-7.6**	**5**
Young [51]	4 & 433	Diam. 6	WPT/ Comm.	20	–	0.005
Bjorninen [34]	400	6.5 × 6.5 × 0.0002	WPT/ Comm.	16	-22	–
Muller [52]	300	Diam. 6.5	WPT/ Comm.	10	-1.5	1
Mestais [53]	13.5 & 400	diam. 50	WPT/ Comm.	200	–	0.45
Das [54]	403 & 1525 & 2425	20.5 × 31 × 0.05	Comm./ WPT/ housekeeping	55	-31.35	–
Talla [55]	13.5 & 915	Diam. 20	WPT/ Comm.	10	-0.97	0.16
Simard [56]	1 & 13.56	Diam. 24	WPT/ Comm.	5	-2.21	4.16
Yeager [57]	1500	0.5 × 0.25	WPT/ Comm.	1	-6.1	1

1.7.3 Literature on WPT and data communication antennas

There is some literature on dual-band antenna systems for WPT and communication. However, it is surprising that so few systems integrate WPT and communication. For example, work mentioned in [51] describes an implantable system for WPT at 4 MHz and data communication at 433 MHz for a freely moving mouse inside a plastic cage that has a limited data rate of 5 kbps. WPT and neural recording can both be achieved using a single antenna system, similar to the work mentioned in [52], where the received power is 3× higher than the required power of the implanted integrated circuit (IC), but with a limited recording rate of 1 Mbps.

It is hard to achieve high data rate and efficient WPT at the same frequency band, using a single BCI antenna, because WPT systems based on inductive coupling require high quality factor (Q) narrow-band antennas [58]; however, broadband antenna systems are required for high data rates [59]. Many papers have demonstrated the idea of WPT and communication systems using discrete antennas without integrating them onto a single BCI printed circuit board (PCB) [46]. Other standard literature is based on dual or triple frequency bands using a single antenna [52, 54]. The dual-band implant antenna system proposed in this work [1], balances these two needs, with a good WPT efficiency of -7.6 dB and communication uplink with a data rate of 5 Mbps, for a separation distance of 15 mm, the highest data rate compared to the literature mentioned in this section.

1.8 Original contributions

The original contributions of the author to date are as follows:

- **Design of dual-band external and implant antenna devices :** To the best of my knowledge, the proposed design is the first ever dual-band (HF and UHF), co-planar antenna system for implanted neural recording and/or stimulation devices. The implant antennas are designed on a 25 mm diameter and 3 mm thick PCB surrounded by a thin layer of bio-compatible silicone encapsulate. The external antennas are designed on an 85 mm diameter and 3 mm thick PCB. Proposed antennas are designed for low SAR and low port-to-port mutual coupling between HF and UHF devices. Related work published in [1] and a patent in [60].

- **WPT and backscatter communication using dual-band external and implant antenna devices :** The pre-recorded neural signals from the implant device were successfully uplinked towards the external device with a data rate of 5 Mbps using saline solution. The HF antennas were able to deliver 1.33 mW towards the implant device with an efficiency of 17 %. The communication link is shown to have a 0 % PER at an implant depth of 2.5 cm and less than 0.91 % up to 3 cm. The insertion loss measured in saline solution at UHF band was 7.5 dB higher as compared to the loss measured in chicken muscle. We expect better communication link in animals as compared to saline, due to lower resistive losses in the protein and fat content of animal tissues. We found comparable insertion loss at 13.5 MHz using saline solution and chicken muscle as biological tissues are almost transparent at 13.5 MHz. Related work published in [61, 62].

- **Design of dual-band external and head-stage antenna devices for NHPs :** To the best of my knowledge, the proposed antenna designs are the first ever dual-band (HF and UHF) BCI antenna system for large NHPs inside a reverberant cavity. The BCI antenna PCB is a two-layer board designed on a 55 mm diameter, 1.6 mm thick FR-4 dielectric. This PCB was designed to fit inside a 3.7 cm long, 5.6 cm inner diameter Teflon cap connected to 8.5 cm long titanium (Ti) tube enclosure which is fabricated to be mounted on the top of the skull of an NHP. In this work, two UHF BCI antennas were designed: (1) a narrow-band ceramic antenna with high gain, and (2) a wide-band μSP antenna. Related work published in [63].

- **UHF antenna characterization inside reverberant housing cage and backscatter communication inside the cage:** To the best of my knowledge, the proposed work is the first ever characterization of the channel transfer function inside a reverberant housing cage. A measured 3 dB channel mean bandwidth of 6.5 MHz with an insertion loss from 14 to 37 dB was achieved at 126 surveyed locations within the cage volume using the ceramic antenna, and a measured 23.8 MHz mean bandwidth was achieved using the wide-band μSP antenna with an insertion loss from 21 to 42 dB. Experimental results show that despite the significant multipath inside the reverberant cage environment, efficient backscatter communication is possible. The relationship between usable bandwidth and $|S_{21}|$ dB in the cage was observed to be similar to mode-stirred reverberant chambers. Related work published in [63].

- ***In-vivo* measurements using anesthetized pigtail macaque in a benchtop setup :** Neural recordings were uplinked successfully to the external system with a data rate of 6.25 Mbps using differential quadrature phase shift keying (DQPSK) from a head-stage ceramic antenna, and 25 Mbps from a head-stage wide-band μSP antenna. Summary of *in-vivo* measurements is shown in Table 1.4. Related work published in [64] along with a paper under review [65].

Table 1.4: *In-vivo* testing using anesthetized pigtail macaque

BCI head stage antenna	**Distance between external and head-stage antennas (cm)**	**-10 dB BW of BCI antenna in free space (MHz)**	**BCI antenna dimensions (cm × cm × cm)**	**BCI antenna gain (dBi)**	**Data rate achieved (Mbps)**
Ceramic Antenna	30	1	2.5 × 2.5 × 2.5	-0.4	6.25
μSP Antenna	35	12.5	1.27 × 0.92 × 0.28	-13.6	25

1.9 Dissertation organization

The remainder of this document is organized as follows:

- Chapter 2 discusses EM wave propagation in a lossy medium along with the discussion of issues such as tissue heating that result from exposing biological bodies to EM waves. The same chapter covers the estimation technique of dielectric properties of different biological materials (e.g., brain, skin) based on Cole-Cole and Debye models.

- Chapter 3 presents dual-band (HF and UHF) implant and external antenna devices for humans/NHPs. The HF band is for WPT and the UHF band is for backscatter communication. The chapter discusses the need for dual-band BCI implant systems as well as background on backscatter communication and WPT. The remainder of the chapter focuses on the design parameters and simulation results of implant and external antennas. In addition to that, encapsulation techniques for implantable systems are covered. The chapter concludes measurement results from implanted antenna in saline solution and chicken muscle.

- Chapter 4 presents dual-band (HF and UHF) antenna systems for large NHPs inside a reverberant metal housing cage, which is an electromagnetically challenging environment for wireless communication. This chapter presents simulation as well as measurement results of UHF antenna characterization inside the reverberant cage. The chapter is further extended to *in-vivo* measurements in a benchtop setup using an anesthetized pigtail macaque at the Washington National Primate Research Center.
- Chapter 5 is the conclusion and proposal for future work.

1.10 List of publications to date

All publications to date are included below.

1.10.1 Patents

1. **A. Sharma** and B. White “Antenna Pattern Shaping Techniques for Mobile Devices”, Filed.
2. **A. Sharma** and M. S. Reynolds “Broadband Single Wire Transmission Line Coupler and Launcher Structures,” U.S. Provisional Patent Application No. 62/445,986.

3. **A. Sharma**, E. Kampianakis, and M. S. Reynolds, “Antenna Elements, Implanted Devices, and Systems for Communication With Implanted Devices,” International Patent Application No. PCT/US2017/016573.

1.10.2 Peer reviewed journals

1. J. Rosenthal, **A. Sharma**, E. Kampianakis and M. S. Reynolds, "A 25 Mbps, 12.4 pJ/bit Backscatter Data Uplink for the NeuroDisc Brain Computer Interface" in IEEE Transactions on Biomedical Circuits and Systems (Under review).

2. **A. Sharma**, E. Kampianakis, J. Rosenthal, A. Pike, A. Dadkhah and M. S. Reynolds, “Wide-band UHF DQPSK Backscatter Communication in Reverberant Cavity Animal Cage Environments”, in IEEE Transactions on Antennas and Propagation (**To be published in the special issue on wireless healthcare biotechnology**).

3. **A. Sharma** A. T. Hoang, F. Dowla, F. Nekoogar and M. S. Reynolds, “An Electrically Small, 16.5 m Range, ISO18000-6C UHF RFID Tag for Metal Cylinder Mounting”, in IEEE Journal of Radio Frequency Identification, vol. 2, no. 2, pp. 49-54, June 2018.

4. X. Fu, A. Pedross-Engel, D. Arnitz, C. M. Watts, **A. Sharma** and M. S. Reynolds, “Simultaneous Imaging Sensor Tag Localization, and Backscatter Uplink Via Synthetic Aperture Radar”, in IEEE Transactions on Microwave Theory and Techniques, vol. 66, no. 3, pp. 1570-1578, March 2018.

5. **A. Sharma**, A. T. Hoang and M. S. Reynolds, “A Coplanar Vivaldi Style Launcher for Goubau Single Wire Transmission Lines”, in IEEE antennas and Wireless Propagation Letters, vol. 16, pp. 2955-2958, 2017.

6. **A. Sharma**, A. T. Hoang and M. S. Reynolds, "Long Range Passive UHF RFID Using a Single Wire Transmission Line," in IEEE Sensors Journal, vol. 17, no. 17, pp. 5687-5693, Sept. 1, 2017.

7. E. Kampianakis, **A. Sharma**, J. T. Arenas, and M. S. Reynolds, "A Dual-Band Wireless Power Transfer and Backscatter Communication Approach for Real-Time Neural/EMG Data Acquisition", in IEEE Journal of Radio Frequency Identification, vol. 1, no. 1, pp. 100-107, March 2017.

8. **A. Sharma**, A. Pedross-Engel, D. Arnitz, C.M. Watts, D.R. Smith and M. S. Reynolds, "A K-Band Backscatter Fiducial for Continuous Calibration in Coherent Millimeter-Wave Imaging," in IEEE Transactions on Microwave Theory and Techniques, vol. PP, no. 99, pp. 1-8, 2017.

9. **A. Sharma**, E. Kampianakis, and M. S. Reynolds, "A Dual-Band HF and UHF Antenna System for Implanted Neural Recording and Stimulation Devices," in IEEE antennas and Wireless Propagation Letters, vol. 16, pp. 493-496, 2017.

1.10.3 Conferences

1. J. Rosenthal, **A. Sharma**, E. Kampianakis and M. S. Reynolds, "A 6.25 Mbps, 12.4 pJ/bit DQPSK Backscatter Wireless Uplink for the NeuroDisc Brain-Computer Interface," in IEEE Biomedical Circuits and Systems Conference (BioCAS), Cleveland, OH, USA, 2018, pp. 1-4.

2. E. Kampianakis, **A. Sharma**, J. T. Arenas, and M. S. Reynolds, "A Dual-Band Wireless Power Transfer and Backscatter Communication Approach for Implantable Neuropros-

thetic Devices,” in IEEE International Conference on RFID, Phoenix, AZ, pp. 67-72, 2017. **Won best poster award and the nomination for best paper award.**

3. X. Fu, **A. Sharma**, E. Kampianakis, A. Pedross-Engel, D. Arnitz and M. S. Reynolds, "A low cost 10.0-11.1 GHz X-band microwave backscatter communication testbed with integrated planar wide-band antennas," in IEEE International Conference on RFID, Orlando, FL, pp. 1-4, 2016.

4. **A. Sharma**, A. Syed and A. R. Harish, "Slotted slim RFID tag antenna for metallic applications," in Indian Antenna Week (IAW), Kolkata, pp. 1-4, 2011.

5. **A. Sharma**, A. Syed and A. R. Harish, "Miniature slotted RFID tag antenna for metallic objects," in International Conference on Communications and Signal Processing (ICCSP), Kerala, pp. 353-357, 2011.

6. **A. Sharma** and A. Syed, "Non-linearity between frequency bands and segmentations of meander antennas," in IEEE Region 8 International Conference on Computational Technologies in Electrical and Electronics Engineering (SIBIRCON), Listvyanka, pp. 279-283, 2010.

CHAPTER 2

EM WAVE PROPAGATION IN A BIOLOGICAL TISSUE

2.1 Introduction

A biological body is a complex mix of different biological tissues, e.g., white matter of the brain, blood vessels, bone cortical, fat, muscle, etc. Each biological tissue has different dielectric properties, which can be estimated from statistical fitting models like the Cole-Cole or Debye models [66]. When an EM wave propagates through a lossy medium, the wave is attenuated, reducing the signal inside the medium. The EM wave propagation inside the biological tissue varies with different parameters like frequency of operation, the geometry and age of the biological tissue, and the polarization of the incident wave. The continuous exposure of biological tissue to EM waves can damage biological tissue. Therefore, it is essential to study EM wave characteristics in the lossy medium. EM wave characteristics can be calculated numerically using wave equations or can be estimated with the help of 3D EM simulation software using a CAD model of a biological body designed in software (commonly known as a numerical phantom). Depending on the application, the numerical phantom can be modeled as a homogeneous structure or a heterogeneous structure as shown in Fig. 2.6. The heterogeneous phantom is an anatomically detailed model of several dielectric layers arranged in a complex manner. In this work, proposed antennas are designed using homogeneous phantoms because they are easy to design, are faster to simulate, and are an effective technique when the location of the biomedical implant is unknown in the body.

This chapter discusses the following topics: (1) the effects of EM exposure to biological tissue, (2) EM wave propagation in a lossy medium based on Maxwell's equation and the wave equation, (3) an estimation of the dielectric properties of biological tissues based on the Cole-Cole model, and (4) details about numerical phantoms.

2.2 Specific Absorption Rate (SAR)

Direct exposure to an EM wave can cause thermal damage to the biological tissue. The absorption of EM energy in a body depends on the duration of exposure and radiation strength [67]. The rate at which the EM field is absorbed by biological tissue is given by the SAR and is measured in watts per kilogram (W/Kg). SAR can be measured using highly sensitive temperature and electric field probes, or it can be estimated using time-domain 3D EM software tools which is much faster and cheaper [2]. SAR is calculated by averaging the rate of absorption in 1 gram or 10 gram of a human tissue sample. In this work, CST time-domain simulation is used to estimate SAR in tissue phantoms. Fig. 2.1 is an example of EM wave absorption inside a homogeneous phantom from a cell phone.

Mathematically, SAR can be written as

$$SAR = \frac{1}{V}\int \frac{\sigma(r)|E(r)|^2}{\rho(r)} dr = c\frac{\Delta T}{\Delta t} \tag{2.1}$$

where $\sigma(r)$ is the electrical conductivity of the tissue, $E(r)$ is the RMS electric field inside the

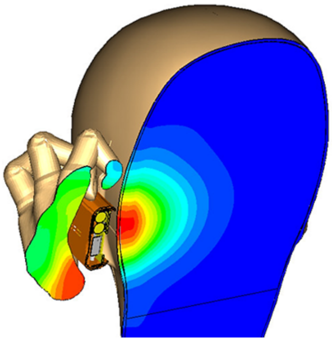

Figure 2.1: Example showing simulated SAR calculated at 1.8 GHz from a cell phone. In this image red color represents peak absorption and blue represents least absorption *(image taken from [2])*.

tissue, $\rho(r)$ is the tissue density, V is the volume of the tissue, c is the specific heat capacity of the tissue, Δt is the change in time, and ΔT is the change in tissue temperature.

2.2.1 Importance of SAR limitation

Temperature rise due to RF absorption exceeding $1^{\circ}-2^{\circ}C$ in the human tissue can cause adverse health effects like heat stroke, heat exhaustion, and ultimately tissue damage [68]. As mentioned in [69] SAR value of 4 W/kg can cause tissue temperature to rise by 1° C. In the United States (US), according to the FCC, the SAR level inside biological tissue should be at or below 1.6 W/kg calculated by averaging a mass of 1 gram of tissue that is absorbing most of the signal [35]. This limitation suggests that the on/in-body wireless devices should be designed for SAR value smaller than 1.6 W/kg to be viable for long-term use.

2.2.2 SAR vs frequency

When a plane wave is incident on a human body, the body acts as an antenna and resonates at a specific frequency. For example, a human body on the conductive ground behaves like a monopole antenna [70]. Multiple experiments and simulations were performed previously, to estimate the behavior of SAR with respect to frequency and it was concluded that the SAR increases until resonant frequency is achieved and then drops after the resonance. The work mentioned in [70] showed that maximum SAR absorption occurs at 65 MHz, 85 MHz, 110 MHz, and 155 MHz for the adult, 10-year-old, five-year-old, and one-year-old phantoms, respectively, under isolated conditions (Fig. 2.2). The resonant region can be calculated approximately for the human height of 0.36 – 0.4 × λ, where λ is the wavelength [71]. Fig. 2.2 suggests that the SAR at 13.5 MHz (HF band) is smaller than the SAR at 915 MHz (UHF band) in biological tissues. Hence, SAR was one of the critical parameter taken into consideration for designing UHF antennas.

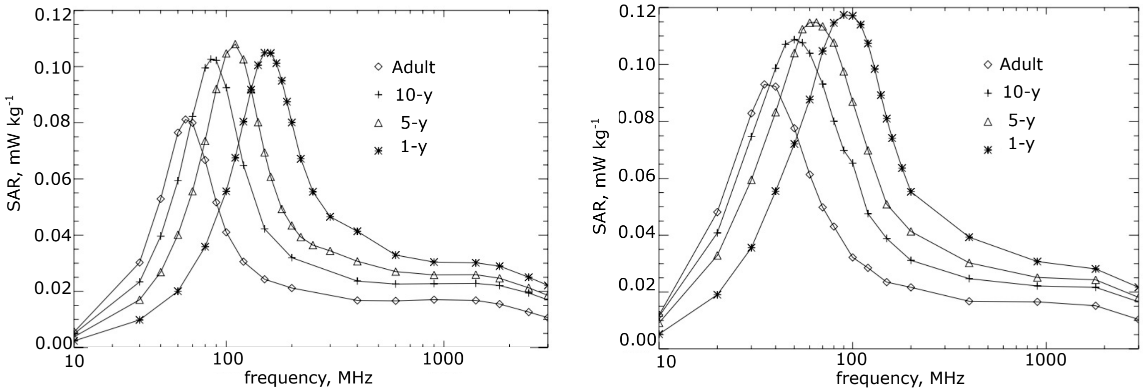

Figure 2.2: The whole-body averaged SAR for the adult, 10-year-old, 5-year-old and 1-year-old phantoms for the incident electric field of 1 V m^{-1} (rms). (Left) Phantom under isolated conditions. (Right) Phantom on the ground. (*image taken from [3]).*

2.3 EM wave propagation in a lossy medium

The permittivity (ϵ) and permeability (μ) are the two main electrical properties of a dielectric material. These two parameters vary with tissue type in a biological system as well as with the frequency of the incident EM wave. In order to describe EM waves in biological tissues, the loss tangent, penetration depth, wave impedance, and attenuation must be understood.

The relative permeability (μ_r) is a complex quantity which can be written as

$$\mu_r = \frac{\mu}{\mu_\circ} = {\mu_r}' - j{\mu_r}'' \tag{2.2}$$

where μ is the permeability of a material, $\mu_\circ$ is the permeability of free space, ${\mu_r}'$ is the real part of the relative permeability. For biological tissue, ${\mu_r}'$ is assumed to be negligible, similar to the permeability of free space and does not change with the frequency [72], ${\mu_r}''$ is a measure of the magnetic losses and does not occur in biological tissues [73].

The relative complex permittivity (ϵ_r) can be written as

$$\epsilon_r = \frac{\epsilon}{\epsilon_\circ} = {\epsilon_r}' - j{\epsilon_r}'' \tag{2.3}$$

where ϵ is the permittivity of the material, $\epsilon_\circ$ is the permittivity of free space, ${\epsilon_r}'$ is the real part of permittivity also known as the dielectric constant, ${\epsilon_r}''$ is out-of-phase loss that occurs due to dielectric damping of vibrating dipole moments and conductive loss [74]. The electrical damping of most of the biological tissues can be assumed to be zero due to the dominance of conductive currents [75]. The out-of-phase loss can be written as

$${\epsilon_r}'' = \frac{\sigma}{\epsilon_o \omega} \tag{2.4}$$

where σ is the total conductivity of the material and ω is the angular frequency.

2.3.1 Estimation of loss tangent

The loss tangent, $\tan(\delta)$ is defined as

$$\tan(\delta) = \frac{\epsilon''}{\epsilon'} \tag{2.5}$$

If $\tan(\delta)$ is zero, then the material is lossless. For example, dry air has zero loss tangent. When the loss tangent is high it implies that the EM absorption in the material would be high. Loss tangent can be derived from Ampere's circuital law which can be written as

$$\nabla \times \overrightarrow{H} = \frac{\partial \overrightarrow{D}}{\partial t} + \overrightarrow{J} \tag{2.6}$$

where $\nabla\times$ is the curl, $\overrightarrow{H}$ is the magnetic field strength, $\overrightarrow{J}$ is the conduction current density, and $\overrightarrow{D}$ is the electric flux density. The conduction current and electric flux density are related to electric field intensity ($\overrightarrow{E}$) and can be written as [74]

$$\overrightarrow{J} = \sigma \overrightarrow{E} \tag{2.7}$$

$$\overrightarrow{D} = \epsilon_0 \epsilon_r \overrightarrow{E} \tag{2.8}$$

From Eqns. 2.7 and 2.8, Eq. 2.6 can be modified to

$$\nabla \times \overrightarrow{H} = j\omega\epsilon_0\epsilon_r \overrightarrow{E} + \sigma \overrightarrow{E} = j\omega\epsilon_0 \left[\epsilon_r - j\frac{\sigma}{\omega\epsilon_0}\right] \overrightarrow{E} \tag{2.9}$$

The overall complex permittivity obtained from Eq. 2.9 can be written as

$$\epsilon = \epsilon_o \left[\epsilon_r - j\frac{\sigma}{\omega\epsilon_o}\right] \tag{2.10}$$

Using Eq. 2.10 the loss tangent can be derived as

$$\tan(\delta) = \frac{\epsilon''}{\epsilon'} = \frac{\sigma}{\omega\epsilon_o\epsilon_r} = \frac{\omega\epsilon_r'' + \sigma}{\omega\epsilon_r'} \tag{2.11}$$

We can see from Eq. 2.11 that the loss tangent increases as the conductivity of a material increases.

2.3.2 Estimation of attenuation and phase constant using wave equation

Wavelength and penetration depth in a media are related to the propagation constant and the attenuation constant. These constants can be derived from Maxwell's equation

$$\nabla \times \overrightarrow{E} = -\frac{\partial \overrightarrow{B}}{\partial t} = -j\omega\mu_0\overrightarrow{H} \tag{2.12}$$

where $\overrightarrow{B}$ is the magnetic flux density.

From wave equation [76]

$$\nabla \times \nabla \times \overrightarrow{E} = \nabla(\nabla \cdot \overrightarrow{E}) - \nabla^2\overrightarrow{E} \tag{2.13}$$

where $\nabla \cdot \overrightarrow{E} = 0$ for a source free region [74].

Eq. 2.13 can be modified to

$$\nabla \times \nabla \times \overrightarrow{E} = \nabla \times (-j\omega\mu_o\overrightarrow{H}) = -j\omega\mu_o\nabla \times \overrightarrow{H} \tag{2.14}$$

Combining Eqs. 2.13 and 2.14 gives

$$\nabla^2\overrightarrow{E} + \omega^2\mu_o\epsilon_o\left[\epsilon_r - j\frac{\sigma}{\omega\epsilon_o}\right]\overrightarrow{E} = 0 \tag{2.15}$$

Eq. 2.15 is the Helmholtz equation [77] from which the wave number k can be derived as

$$k = \omega\sqrt{\mu_o\epsilon_o\left[\epsilon_r - j\frac{\sigma}{\omega\epsilon_o}\right]} \tag{2.16}$$

The propagation constant γ can be written as

$$\gamma = \alpha + j\beta = jk = j\omega\sqrt{\mu_o\epsilon_o\left[\epsilon_r - j\frac{\sigma}{\omega\epsilon_o}\right]} \tag{2.17}$$

where α is the attenuation constant which is 0 for a lossless medium, and β is the phase constant in rad/m. Constants α and β can be derived as

$$\alpha = \frac{\omega}{c_o}\sqrt{\frac{\epsilon_r}{2}\sqrt{1+\left[\frac{\sigma}{\omega\epsilon_o\epsilon_r}\right]^2}-1} \tag{2.18}$$

$$\beta = \frac{\omega}{c_o}\sqrt{\frac{\epsilon_r}{2}\sqrt{1+\left[\frac{\sigma}{\omega\epsilon_o\epsilon_r}\right]^2}+1} \tag{2.19}$$

where c_o is the speed of light in vacuum.

2.3.3 Estimation of wavelength

Using Eq. 2.19, the wavelength (λ_m) of EM signal in a lossy medium can be written as

$$\lambda_m = \frac{2\pi}{\beta} = \frac{2\pi c_o}{\left(\omega\sqrt{\frac{\epsilon_r}{2}\sqrt{1+\left[\frac{\sigma}{\omega\epsilon_o\epsilon_r}\right]^2}+1}\right)} \tag{2.20}$$

Eq. 2.20 suggests that the wavelength dependents on the operating frequency, material conductivity, and permittivity of the media.

2.3.4 Depth of penetration

When EM wave is incident on the surface of a material, a portion of the wave is reflected back and a portion propagates into the material and gradually attenuates. The distance at which the signal power density decreases by a factor of $1/e$ or by 36.8 % is called penetration depth [74, 78].

The penetration depth (δ_p) can be written as

$$\delta_p = \frac{1}{\alpha} = \frac{c_0}{\left(\omega\sqrt{\frac{\epsilon_r}{2}\sqrt{1+\left[\frac{\sigma}{\omega\epsilon_0\epsilon_r}\right]^2}-1}\right)} \tag{2.21}$$

Above equation suggests that the penetration depth dependents on the operating frequency, the conductivity and the permittivity of the material. Penetration depth decreases with the increase in frequency. More details are mention in Section 2.4.3. This behaviour suggests that lower frequency signals can travel longer inside a dielectric material without significant attenuation.

2.3.5 Wave impedance in the medium

The wave impedance $Z(\omega)$ is a ratio of the electric and magnetic fields and can be defined as [74]

$$Z(\omega) = \frac{E(\omega)}{H(\omega)} = \sqrt{\frac{\mu_o}{\epsilon}} \tag{2.22}$$

where $E(\omega)$ is the electric field and $H(\omega)$ is the magnetic field.

Placing complex permittivity term from Eq. 2.10 in Eq. 2.22 gives the relationship between the wave impedance, the dielectric property, and the frequency

$$Z = \sqrt{\frac{\mu_o}{\epsilon_o\left[\epsilon_r - j\frac{\sigma}{\omega\epsilon_o}\right]}} \tag{2.23}$$

where Z is the wave impedance. From Eq. 2.23 we can conclude that the EM wave has lower impedance inside biological tissues as compared to the impedance in free space, although this impedance is different depending on the tissue. Hence, an antenna matched for one specific tissue will lead to impedance mismatch losses for other tissues, thus reducing the antenna's radiation efficiency.

2.4 Dielectric properties of biological tissue

EM wave propagation in a biological system depends on the frequency, the body's physiological parameters, the dielectric permittivity, and the polarization of the incident wave. If the dielectric property of each tissue layer is known, the parameters such as penetration depth and attenuation can be determined. Hence, it is essential to estimate the dielectric property of biological tissues from the statistical models like Cole-Cole or Debye equations. These equations are based on the experimental data of biological tissues mentioned in [79].

2.4.1 Permittivity vs frequency

Fig. 2.3 shows that the permittivity varies with respect to frequency [80]. In the presence of electric fields, materials exhibit a variety of resonance phenomena. Fig. 2.3 represents the variation of relative permittivity as a function of frequency, which can be divided into four zones: ionic, dipolar, atomic, and electronic. Ionic conduction ranges from low frequencies up to MHz. In this zone, the displacement of ions occurs in the presence of electric fields.

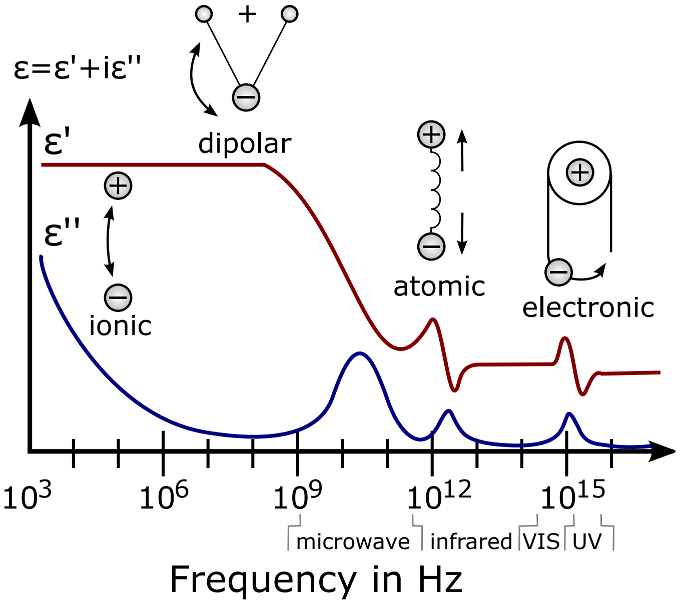

Figure 2.3: Permittivity as a function of frequency *(image taken from [4]).*

The dipolar zone ranges from MHz to GHz. In this region, dipoles become polarized in the direction of the applied field. The atomic zone occurs from the GHz to the infrared region. Atomic polarization occurs when neighboring positive and negative ions stretch under an applied electric field. Electronic polarization occurs in neutral atoms when an electric field displaces the nucleus cloud with respect to the surrounding electrons [81].

2.4.2 Tissue property estimation using Cole-Cole model

The permittivity of biological tissues can be efficiently estimated over a wide range of frequencies from the Cole-Cole model. The Cole-Cole model can be written as

$$\epsilon(\omega) = \epsilon_\infty + \frac{\Delta\epsilon}{1 + (j\omega\tau)^{1-a}} \tag{2.24}$$

$$\Delta\epsilon = \epsilon_s - \epsilon_\infty \tag{2.25}$$

where $\epsilon(\omega)$ is the permittivity which is a function of frequency, $\Delta\epsilon$ denotes the magnitude of the dispersion, ϵ_s is the static permittivity calculated at the lowest frequency, ϵ_∞ is the permittivity when the frequency approaches infinity (ω -> ∞), j=$\sqrt{-1}$, τ is the relaxation time which is the time required for the signal to reduce by 1/e or 36.8 % from its initial value, a describes broadening of the dispersion ($0 < a < 1$), and ω is the frequency [82, 83]. For the simplification of calculations ϵ_∞ can be assumed as 2.5 for bone and 3.5 for all other tissues for the frequency range of 1 MHz to 20 GHz [84].

2.4.3 Biological tissue permittivity used in this work

In this work, biological EM simulations were performed using CST MWS. For simulations, we used CST's built-in biological tissue library for biological tissue material properties. Fig. 2.4

(a) and Fig. 2.4 (b) shows real and imaginary permittivity, respectively, of different tissues for the frequency range of 1 MHz to 1000 MHz obtained from CST's material library.

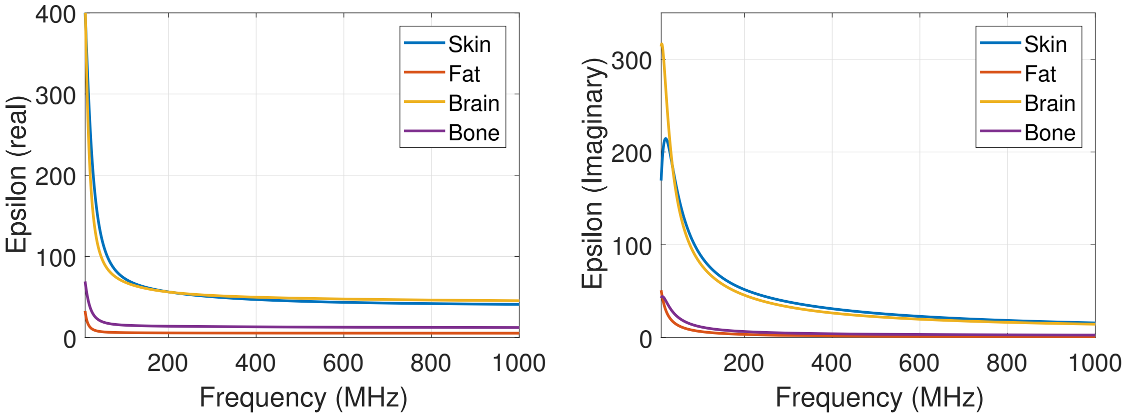

(a) (b)

Figure 2.4: (a) Simulated real permittivity of different biological layers for the frequency range of 1 MHz to 1000 MHz. (b) Simulated imaginary permittivity for the frequency range of 1 MHz to 1000 MHz.

In general, tissues with higher water content have higher real and imaginary permittivity since the water has high dielectric constant and high conductivity. As shown in Fig. 2.4, fat has the lowest real part of permittivity as compared to other layers since the water content is relatively small and is almost constant from 100 MHz to 1000 MHz. The skin and the brain have high permittivity because of high water content in the tissues.

Eq. 2.10 suggests that the imaginary part of the complex permittivity is proportional to the conductivity of the material. As shown in Fig. 2.4 (b), bone and fat have a low imaginary part of permittivity while skin and brain tissues have a very high imaginary part which is due to the high conductivity [85]. Therefore, significant attenuation of EM signals in the brain and skin is expected as compared to fat and bone at HF and UHF bands.

The values of loss tangent, penetration depth, and wave impedance for different layers are mentioned in Tables 2.1, 2.2, and 2.3 at 13.5 MHz, 915 MHz, and 2.45 GHz, respectively [86].

Table 2.1: Loss tangent, penetration depth and wavelength in human tissues at 13.5 MHz

	Loss tangent	**Penetration Depth (m)**	**Wavelength (m)**
Brain (Grey Matter)	1.64	0.31	1.12
Fat	3.45	0.9	4.27
Bone (Cortical)	1.97	0.81	3.16
Skin (Wet)	2.87	0.26	1.17

Table 2.2: Loss tangent, penetration depth and wavelength in human tissues at 915 MHz

	Loss tangent	**Penetration Depth (m)**	**Wavelength (m)**
Brain (Grey Matter)	0.35	0.04	0.04
Fat	0.18	0.24	0.13
Bone (Cortical)	0.22	0.09	0.12
Skin (Wet)	0.36	0.04	0.04

Table 2.3: Loss tangent, penetration depth and wavelength in human tissues at 2.4 GHz

	Loss tangent	**Penetration Depth (m)**	**Wavelength (m)**
Brain (Grey Matter)	0.27	0.02	0.02
Fat	0.14	0.12	0.05
Bone (Cortical)	0.25	0.05	0.04
Skin (Wet)	0.27	0.02	0.02

From Tables 2.1 - 2.3, it is clear that penetration depth decreases with higher frequencies and is smaller for tissues with higher water content (i.e. brain and skin). The attenuation of the signal in biological tissues reduces the efficiency of the overall communication system.

2.5 Estimation of dielectric properties of saline solution using Debye first order model

In this work, saline solution is used as a tissue proxy for testing of the implant antennas since it is easier to make in the laboratory. Saline solution is a homogeneous phantom whose conductivity and permittivity changes with frequency. The dielectric properties of a saline proxy are calculated using Debye first order model [87], which can be written as

$$K = \epsilon_\infty + \frac{\epsilon_s - \epsilon_\infty}{1 - j2\pi\tau f} + j\frac{\sigma}{2\pi\epsilon_0 f}, \tag{2.26}$$

where K is the dielectric constant, ϵ_s is the static dielectric constant of the solvent calculated at lowest frequency and ϵ_∞ is calculated at the highest frequency , τ is the relaxation time, ϵ_0 is the dielectric constant of free space which is 8.854×10^{-12}, σ is the ionic conductivity and f is the frequency of operation. Static dielectric, and relaxation time can be calculated using following equations [88],

$$\epsilon_s(T, N) = \epsilon_s(T, 0)\alpha(N) \tag{2.27}$$

and

$$2\pi\tau(T, N) = 2\pi\tau(T, 0)b(N, T) \tag{2.28}$$

where T is the water temperature in $^\circ C$, and N is the normality of the solution.

Eqns. 2.27 and 2.28 are valid for $0 \leq T \leq 40\ ^\circ C$ and $0 \leq N \leq 3$ [87]. The normality N can be calculated as

$$N = S(1.707 \times 10^{-2} + 1.205 \times 10^{-5} S + 4.058 \times 10^{-9} S^2) \tag{2.29}$$

where S is the salinity in parts per thousand and is valid for $0 \leq S \leq 260$.

The $\alpha(N)$, $b(N, T)$, and $\epsilon_s(T, 0)$ mentioned in Eqns. 2.27 and 2.28 can be obtained from the following equations [88]

$$\alpha(N) = 1 - 0.2551N + 5.151 \times 10^{-2} N^2 - 6.889 \times 10^{-3} N^3 \tag{2.30}$$

$$\epsilon_s(T, 0) = 87.740 - 0.4008T + 9.398 \times 10^{-4} T^2 - 1.410 \times 10^{-6} T^3 \tag{2.31}$$

Eq. 2.31 shows that the static dielectric constant varies with temperature. Hence, the environment and temperature of the tissue are essential when performing experiments.

$$b(N,T) = 0.1463 \times 10^{-2} NT + 1 - 0.04896N - 0.02967N^2 + 5.644 \times 10^{-3} N^3 \tag{2.32}$$

The relaxation time of water can be written as [87]

$$2\pi\tau(T,0) = 1.1109 \times 10^{-10} - 3.824 \times 10^{-12} T + 6.938 \times 10^{-14} T^2 - 5.096 \times 10^{-16} T^3 \tag{2.33}$$

In this work, ϵ_∞ is taken as 4.9 as mentioned in [89]. The conductivity of saline solution mentioned in [87] can be written as

$$\begin{aligned}\sigma(T,N) = \sigma(25,N)[1 - 1.962 \times 10^{-2}\Delta + 8.08 \times 10^{-5}\Delta^2 - \Delta N(3.020 \times 10^{-5} + 3.922 \times 10^{-5}\Delta + \\ N(1.721 \times 10^{-5} - 6.584 \times 10^{-6}\Delta))]\end{aligned} \tag{2.34}$$

where $\Delta = 25 - T$. The ionic conductivity at 25 $^\circ C$ can be written as

$$\sigma(25,N) = N(10.394 - 2.3776N + 0.68258N^2 - 0.13538N^3 + 1.008610^{-2}N^4) \tag{2.35}$$

Once ionic conductivity, relaxation time, frequency, temperature, and static dielectric constants are known, we can estimate dielectric constant of saline solution.

The saline solution used for the testing of antennas in this work, contains the following recipe: 0.91 grams of sodium chloride (NaCl) per liter of distilled water [90]. For this recipe, the normality was estimated as 0.0155. Complex permittivity obtained from Eq. 2.26 is 72.2 - j19.69 calculated at 25 °C and at 915 MHz. This permittivity value was used in the simulations. The real part of permittivity of the brain is around 55, and dura is 68.6 at 915 MHz.

The complex permittivity of saline solution (0.91 grams of NaCl per liter of distilled water) with respect to solution temperature is shown in Fig. 2.5. THis suggests that the permittivity varies a lot with the temperature. Hence, all the experiments should be performed at the same temperature.

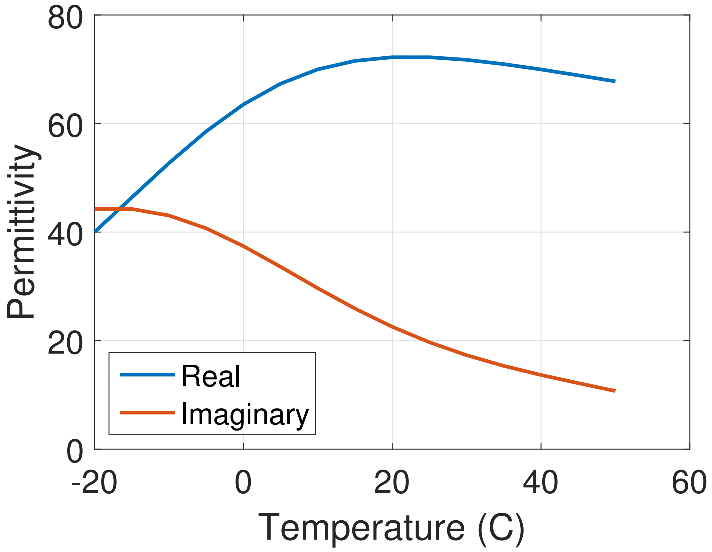

Figure 2.5: Variation of permittivity with respect to saline solution temperature.

2.6 Why biological EM simulations?

In this work, biological simulations were utilized because of the following reasons:

- Invasive experiments on human body is difficult and almost impossible for such preliminary work,
- From simulations we can estimate antenna parameters like SAR, electric/magnetic field distributions, radiation properties and surface current. These parameters are complicated to calculate from theoretical equations.

2.7 Numerical phantoms and electromagnetics modeling

The biological body is an electromagnetically complex structure that consists of various biological tissues such as skin, bone, and internal organs. Numerical methods such as finite element method (FEM) or finite integral technique (FIT) are used to characterize electromagnetic interactions between the biomedical device and the biological body.

2.7.1 Types of numerical phantoms

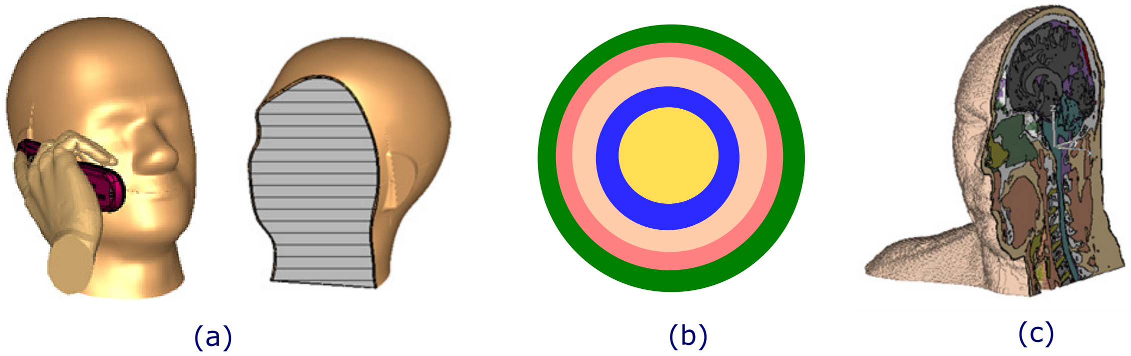

Figure 2.6: Types of numerical phantoms. (a) Homogeneous model *(image taken from "head and hand - mobile phone" example in CST MWS)*. (b) Layered model. (c) Heterogeneous model *(image taken from CST's "visible human model dataset")*.

A biological numerical phantom can be designed in three ways:

- The homogeneous model, as shown in Fig. 2.6 (a), sometimes called Specific Anthropomorphic Mannequin (SAM) [91], contains a uniform material that represents the average material properties of the biological body. The advantage of using the SAM model is that the simulation can be performed with a low memory system and can be simulated with a low number of mesh cells.

- The second type of biological model is the layered model [92], as shown in Fig. 2.6 (b), contains several layers of homogeneous materials like skin, fat, muscle, or brain. In general, layered models are designed in the shape of rectangular boxes or spheres. The layered model contains more features than the homogeneous SAM model and is more accurate for the estimation of EM field behavior inside the phantom.

- The third type of model is called the heterogeneous model, as shown in Fig. 2.6 (c), is an anatomically detailed three-dimensional representation of the biological bodies [93].

Those CAD models are based on CT, MR, and cryosection images [94]. The disadvantage of using a heterogeneous model is that the model requires a high-end computer or GPU and is mesh extensive i.e. simulations often require extensive run-time and memory. This kind of model is preferred when the fixed position of a biomedical device is known inside a biological body.

2.7.2 Numerical phantoms used in this work

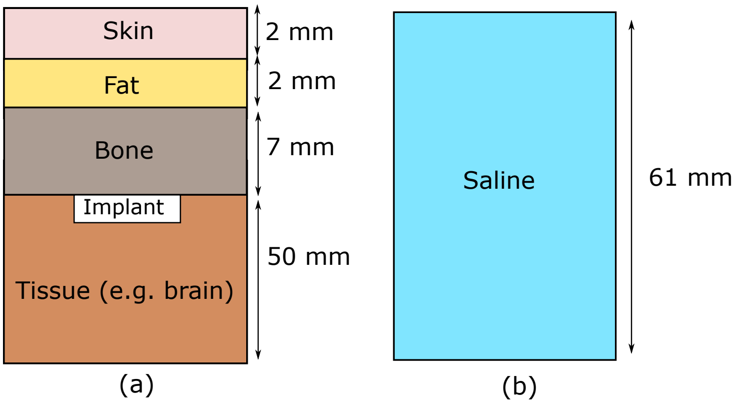

Figure 2.7: Numerical phantoms used in this work for simulations. (a) Four layer model. (b) Homogeneous saline model.

In this work, two types of biological CAD models are used for the simulation:

1. **A four-layered model** : This model contains skin, fat, bone, and tissue layers (Fig. 2.7(a)). The four-layer model was used due to the following reasons: (a) the position of the implant is unknown in the biological body, (b) the model is easy to design and simulate, (c) the simulation does not require a high-end computer or GPU, and (d) the simulation is not mesh extensive. A CST inbuilt bio-library was used to import material properties of each layer.

2. **A homogeneous saline model** : The saline homogeneous model is designed to compare the experimental results of antennas performed using a saline solution (0.91 grams

of NaCl per liter of distilled water) serving as tissue proxy (Fig. 2.7(b)). Simulated implant performance in saline and four-layered model is presented in Section 3.14 along with measured performance in the saline solution.

2.8 Conclusion

This chapter discusses the behavior of the EM wave in lossy media and the hazardous effects of direct exposure of the EM wave towards biological bodies. A rise in temperature due to RF absorption in the biological tissue can cause adverse health effects, and ultimately results in tissue damage. Hence, it is essential to design biomedical devices with low SAR.

Equations for the wave attenuation, penetration depth, and wavelength inside the lossy medium are presented in the chapter. The dielectric properties of biological tissues and of the saline solution are presented in the chapter based on Cole-Cole model and Debye model, respectively. From the Cole-Cole model, the tissues with higher water content (e.g. skin) have a higher dielectric constant as compared to the tissues with lower water content (e.g. fat and bones). The imaginary part of permittivity is higher for the tissues with higher water content, e.g., the imaginary permittivity of bones and fat are smaller as compared to the skin and brain tissue [85]. Therefore, a large attenuation of EM signals in the brain and skin is expected as compared to the fat and bones. The biological body is a complicated structure, hence, for faster but nonetheless accurate estimations, 3-D simulation software is preferred. In this chapter, various types of numerical phantoms are presented for the simulations and the advantages and disadvantages of each type are discussed.

CHAPTER 3

ANTENNA SYSTEMS FOR IMPLANTABLE WIRELESS DEVICES

*The chapter is an adapted version of [1, 61, 62].

3.1 Introduction

This chapter presents a dual-band (HF (13.5 MHz) and UHF (902–928 MHz)) antenna system for implanted neural recording and/or stimulation devices. The system consists of implanted and external antennas that are capable of supporting frequency bands for WPT and data communication while being as compact as possible. The implant antenna is designed to be embedded in the dura layer inside a human's head that is approximately 1 cm below the skin surface. The external antenna is designed to be fit in a cap which the user can wear on their head such that the external antenna is within a few millimeters to the head's skin.

The dual-band implant device presented in this work is designed to prevent interference between the WPT and communication systems while also inducing low SAR to avoid tissue heating. The implant antenna is a three-layer PCB in which the middle layer is the ground plane. This three-layer stack-up permits electronics to be placed on the back side of the antenna to minimize the total volume of the implant. The internal ground layer is required to reduce signal coupling between the antenna and the electronics. The implanted device is encapsulated in a 1 mm thick bio-compatible silicone on all sides to avoid PCB corrosion and to protect biological tissue from PCB impurities. The overall size of the implanted device is 27 mm diameter and 3 mm thickness, including a thin layer of encapsulation. The 27 mm diameter constraint is driven by a collaborator who informed us that this is the smallest dimension that could be cut into a human skull during interventional epilepsy surgeries [95]. The external antenna device is designed on a two-layer PCB whose outer diameter is 85 mm and 3 mm thickness. The top layer is utilized for the antennas, and the bottom layer for the matching components and the antenna feeds. A photo of the fabricated antennas and a layered block diagram are shown in Fig. 3.1.

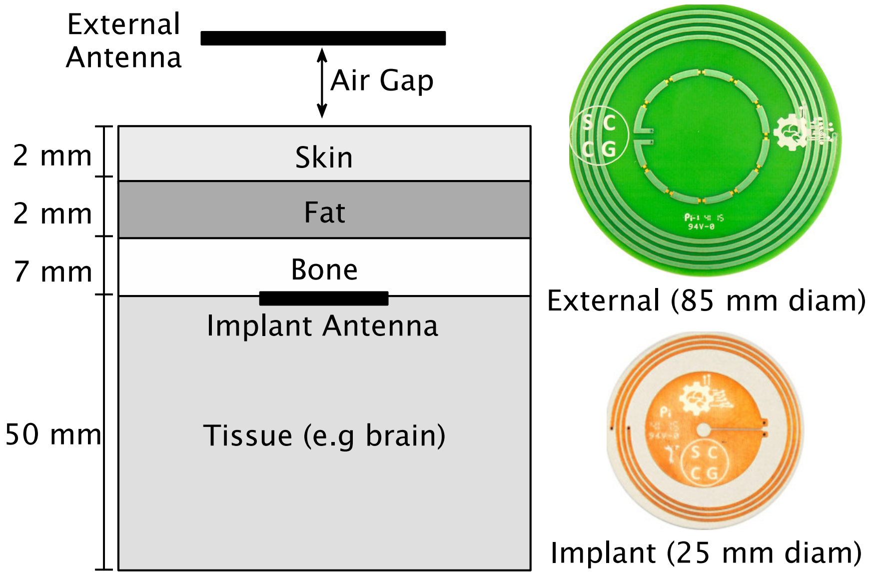

Figure 3.1: (Left) 4- layer model showing location of the implant and the external antennas. (Right) Photo of fabricated external and implant antennas. Encapsulation layer not present in antenna images.

The implant antenna was simulated inside the four-layer bio-model, with the external antenna in close proximity to the bio-model, as shown in Fig. 3.1, using time- and frequency-domain solvers (CST Inc). This layered model is a common design in the literature, which has been used to design prior neural implants [52]. The implant antenna system was fabricated and tested using saline solution and chicken muscle. From the experiments, parameters such as HF loop efficiency, UHF antenna bandwidth, and transmission coefficients, were obtained.

3.2 The implant antenna: challenges

The system requirements which make designing an implant antenna challenging are explained below:

1. **Implant size :** The shape and size of implant antenna depend mainly on its location in biological body, and the amount of tissue displacement [96, 97] which limits the applicability of single antenna type around multiple organs. Typically, implanted devices [33, 34] have volumes on the order of a few mm^3 to a few cm^3, limited by allowable tissue displacement.

2. **Wide bandwidth and high data rates :** Requirements of the communication bandwidth increase with the number of supported electrodes; given reasonable assumptions about sampling rate and resolution, data rates into the tens to hundreds of Mbps are required for high-density probes with dozens of electrodes [98]. The system bandwidth and the data rate are related to each other and can be obtained from the Nyquist formula.

$$C = 2 \times B \times log_2(M) \tag{3.1}$$

where C is the channel capacity in bits per second, B is the bandwidth, and M is the number of symbols used in the communication. Eq. 3.1 implies that for high data rates, communication systems should have high bandwidth. On the other hand, the "Chu-Harrington limit" describes that it is a challenging task to design an efficient small-sized implant for a wide bandwidth [99]. This limit is written as

$$Q = \eta\left(\frac{1}{(ka)^3} + \frac{1}{ka}\right) \tag{3.2}$$

where k=$2\pi/\lambda$ is the wave number, λ is the wavelength, a is the smallest radius of the sphere enclosing the antenna, η is the efficiency, Q is the quality factor which is inversely proportional to the antenna bandwidth ($Q \propto 1/B$). The "Chu-Harrington" limit suggests that for a given antenna efficiency the quality factor must increase and the bandwidth must decrease with a reduction in antenna size.

3. **Radiation efficiency :** Electrically-small antennas have low radiation efficiency due to low radiation resistance. The relationship between radiation resistance (R_r) and radiation efficiency (η) can be written as

$$\eta = \frac{R_r}{R_r + R_l} \tag{3.3}$$

where R_l is the ohmic resistance and R_r is is directly proportional to the antenna length [100]. Furthermore, biological tissues reduce the overall radiation efficiency because conductive tissue absorbs the EM waves. More details about EM absorption in biological tissues are mentioned in Section. 2.3.4.

4. **Encapsulation material :** It is necessary to package the implantable device to protect the device from corrosion and to protect tissues from device impurities [101]. The material used for encapsulation must be biocompatible and non-toxic. Commonly used encapsulation materials are titanium, platinum, and silicone [102]. Antennas

should be encapsulated in a dielectric material instead in a metal enclosure. It is essential to simulate implant antenna along with an encapsulation layer, since the layer of encapsulation can change antenna resonance, gain, or bandwidth.

5. **Low SAR requirements:** Biomedical antennas should be designed for SAR smaller than the FCC limit, to avoid tissue heating (Refer to Section. 2.2 for more details).

6. **Small mutual coupling:** The HF and UHF implant antennas should be designed for small mutual port-to-port coupling to avoid unwanted signal interference between them and to increase the signal-to-noise ratio.

3.3 Why develop a dual-band implant?

In this work, the HF band antenna is designed to supply power to the implant via inductive coupling. This HF band was chosen for WPT due to the minimal interaction of EM waves with a biological tissue because of long wavelength (≈ 20 m) resulting in a high link efficiency between external and the implant antenna systems.

Due to the insufficient ISM bandwidth (14 KHz) available in the HF spectrum and for high data rates, communication links in the 915 MHz or 2.4 GHz band are the two standard choices in the ISM frequency bands. The 915 MHz band has a bandwidth of 26 MHz while the 2.4 GHz band has 100 MHz bandwidth. The advantage of designing an antenna at 2.4 GHz is that good antenna radiation efficiency can be achieved for smaller antenna size due to its shorter wavelength as compared to designing the antenna at 915 MHz band. However, path loss increases with the increase in frequency, which increases the insertion loss between the external antenna and the implant antenna. In this work, the 915 MHz UHF band was chosen for the communication because of sufficient bandwidth and smaller path loss as compared

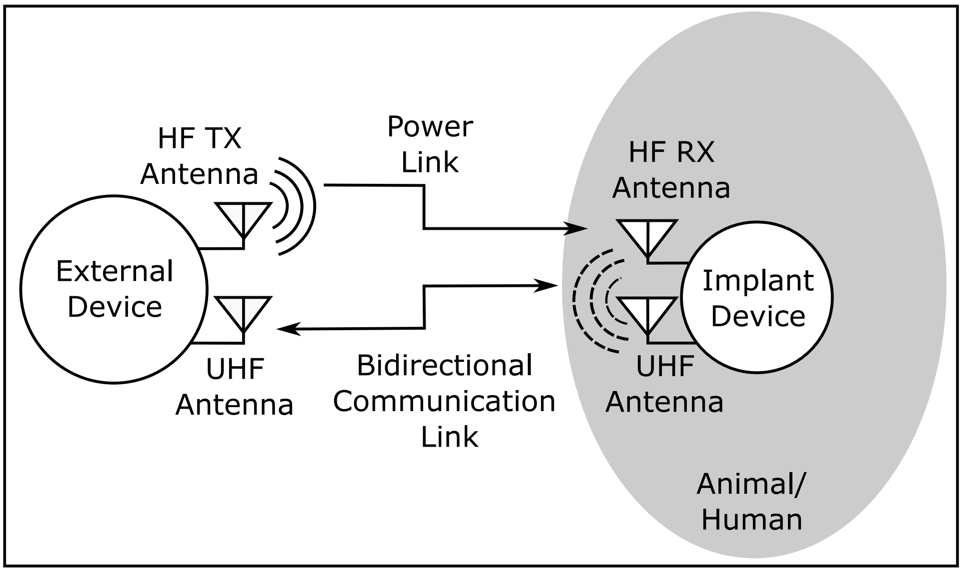

Figure 3.2: Block diagram showing dual-band power and communication system concept.

to the 2.4 GHz band. The block diagram of the dual-band implant system proposed in this work, is shown in Fig. 3.2.

3.4 Implant PCB requirements

The outer diameter of the implantable device is limited by the dimension of the electrocorticography (ECoG) electrode array used in interventional epilepsy surgeries [95]. The electrode grids were constructed using exposed platinum-iridium pads that were 2.4 mm in diameter and embedded in silastic (AdTech, Racine, WI). Two arrangements of electrode grids are used in epilepsy surgeries performed by one of our collaborators [95]. The spacing between the adjacent grids is 10 mm in one electrode array while the electrode spacing in the other grid is 7 mm. The grid mentioned in the two arrangements is either set in an 8 × 8 array or a 4 × 8 array.

In the 4 × 8 array with 7 mm grid spacing, the minimum implant dimension that can be designed is for the board diameter of 28 mm. This 28 mm is the smallest dimension of the skull flap. The implant PCB presented in this work is based on the smallest skull flap.

To fit the implantable device inside the smallest skull flap, the implant was designed on a PCB that was 25 mm in diameter and surrounded by a thin (approximately 1 mm) layer of encapsulation, resulting in an overall width of 27 mm.

3.5 Wireless power transfer (WPT)

A BCI system should have an ability to charge wirelessly to eliminate the need for heavy and bulky batteries and to prevent surgeries to replace them [103]. This is possible by replacing the battery with small antennas and charging the implant device from the external device using EM waves based on near-field (non-radiative) or far-field (radiative) technique [104].

Far-field technique: Far-field WPT is based on propagating EM waves [105]. This technology can transmit power over long distances through directive or omnidirectional transmitting antennas. The fundamental problem limiting far-field WPT is of free-space path loss. The divergence of the EM beam in free-space causes the power available to the receiver to decrease at a rate of $1/d^2$, where d is the range between the transmitter and receiver antennas.

Near-field technique: Near-field WPT can be utilized to transfer power efficiently for short distances up to a few centimeters [105]. This can be achieved using two methods: (a) inductive loops based on magnetic field coupling, and (b) parallel plate capacitors, using electric field coupling. Inductive WPT systems are more common than capacitive WPT systems because of higher efficiency.

The simplified block diagram of inductive WPT system is shown in Fig. 3.3. At the RF transmitter side, AC signal is converted to a magnetic field through self-resonating inductive loop. This magnetic field is then coupled into the nearby inductive receiver loop. The receiver loop is connected to the rectifier which converts AC voltage to DC voltage and supplies DC voltage to the load.

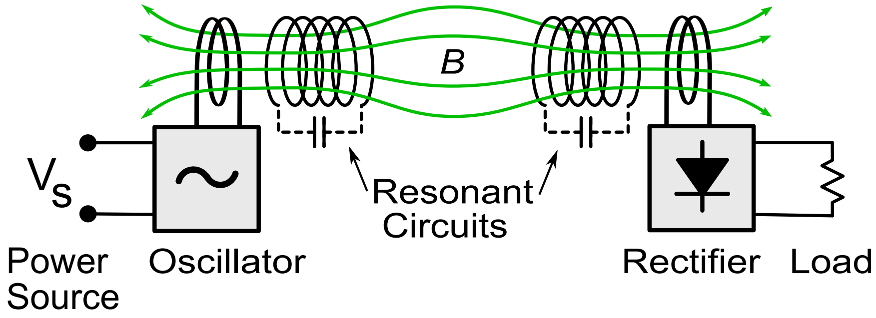

Figure 3.3: Block diagram of inductive WPT system (*image source: CC0 1.0 Universal Public Domain Dedication format [5]*).

3.6 Backscatter communication

In this work, antennas are designed for backscatter communication. The concept of backscatter communication is widely known through radio frequency identification (RFID) technology. A block diagram of backscatter communication is shown in Fig. 3.4.

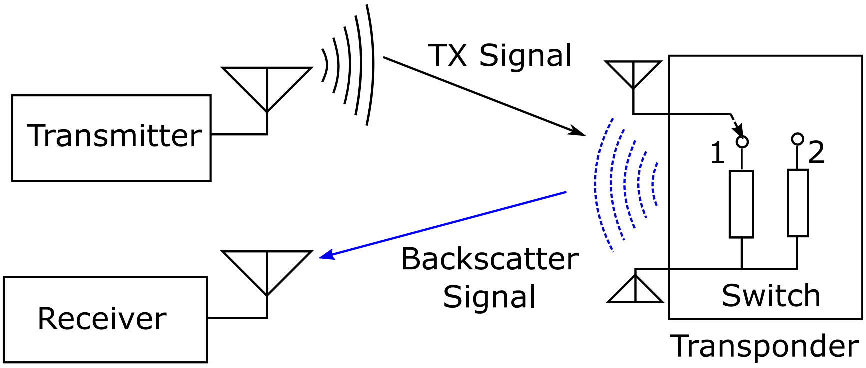

Figure 3.4: Block diagram of the backscatter communication.

In backscatter-based devices, a time-varying impedance is applied to the antenna, which modulates the amplitude and phase of the incident CW by changing the radar cross-section (RCS) [106, 107, 108]. The RCS is the effective area through which the EM field is reflected from the backscatter antenna to the receiver antenna and can be written as

$$\Delta\sigma = \frac{\lambda^2}{4\pi} G_B^2 |\Gamma_{L1}^* - \Gamma_{L2}^*|^2 \tag{3.4}$$

where $\Delta\sigma$ is the differential RCS, G_B is the backscatter antenna gain, Γ_{L1}^* and Γ_{L2}^* are the complex power wave reflection coefficient at the backscatter antenna for the two impedance states ($L1$ and $L2$) of the switch. The reflection coefficient is the ratio of reflected signal to the incident signal and can be derived from

$$\Gamma^*_{1,2} = \frac{Z_{\mathrm{L1,L2}} - Z^*_{\mathrm{B}}}{Z_{\mathrm{L1,L2}} + Z_{\mathrm{B}}} \tag{3.5}$$

where $Z_{L1,L2}$ are complex impedances of the two states of the RF switch, and Z_{B} is the antenna's characteristic impedance.

To maximize SNR of the backscattered signal, it is important to have the largest possible vector distances between the complex impedance states. In theory, maximum scattering reflection coefficients can be achieved through short and open circuits given by $Z_L = 0$ for a short circuit, and $Z_L = \infty$ for an open circuit, which gives $\Gamma_L = -1$ and $\Gamma_L = +1$, respectively. However, in practical scenarios the impedances vary with frequency and often with incident power [109].

3.6.1 Pros and cons of backscatter communication

The advantage of backscatter communication over conventional radios is that the backscatter-based devices do not require power-hungry active RF amplifiers and oscillators to generate a communication carrier. This quality allows backscatter systems to be very small and yet provide high data rates (>96 Mbps) [29] with orders of magnitude less power consumption as compared with Bluetooth Low Energy and WiFi (IEEE 802.11n) [30].

The trade-off with backscatter communication is a less favorable link budget than the conventional radios because the communication carrier from transceiver travels a round-trip path via reflection from the backscatter antenna. As a result, the received signal power at the transceiver side is proportional to $1/d^4$, where d is the distance between the transceiver and the backscatter source, while received signal from the conventional radio is proportional to

$1/d^2$ [110].

3.7 A 85 cm diameter 3 mm thick dual-band external antenna device

The dual-band external antenna device is designed to be placed external to the outermost tissue layer, with a nominal 5 mm air gap between the inner surface of the external antenna and the outer surface of the skin. As shown in Fig. 3.5, the external antenna device has a concentric arrangement of HF (outer annulus) and UHF (inner ring) antenna elements fabricated on a two-layer printed circuit, 85 mm in diameter with 2 mm thick FR-4 substrate and 2 oz copper traces. The bottom layer is utilized for the ground plane, feed, and the matching networks. For the protection of the antenna from the saline solution, the antenna was laminated between 0.4 mm thick Teflon sheets, yielding overall dimensions of 85 mm × 3 mm (diameter × thickness).

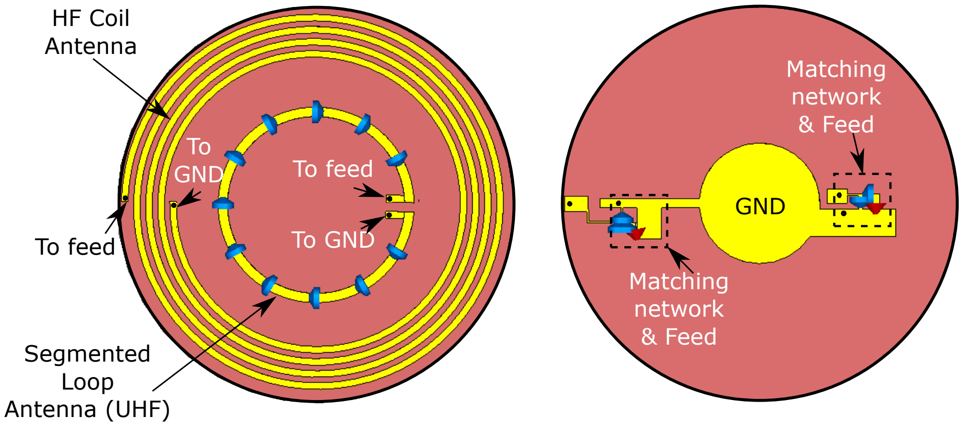

Figure 3.5: Plan views of the external antenna. (Left) Top view showing UHF and HF antennas. (Right) Bottom view showing matching network, feed, and ground plane.

3.7.1 External HF spiral loop antenna for WPT

The HF antenna structure is the simpler of the two antenna structures shown in Fig. 3.5. It consists of a 4-turn continuous spiral loop with outer radius 41.6 mm and inner radius 29.8 mm. A circular spiral shape was chosen because the implant board has a circular outline. The trace width is 1.4 mm and the inter-turn spacing is 1.2 mm. One end of the loop is connected to the ground plane through a conductive via and the other end of the loop is connected to the feed through another conductive via.

The number of turns, width and turn spacing of HF spiral antenna were optimized using the frequency domain solver in CST to fulfill two primary requirements:

- To achieve acceptable coupling efficiency between external and implant loop antennas,
- To maintain minimal surface current coupling between external HF and external UHF antennas.

3.7.2 External UHF segmented loop antenna for communication

For the external UHF antenna, a segmented loop structure was chosen for two reasons:

- Unlike a continuous loop where the circumference is comparable to the guided wavelength, segmented loops can be engineered to yield a relatively uniform magnetic field (H-field) within the diameter of the loop. The simulated H-field plots at 915 MHz across the loop and the segmented loop antennas are shown in Fig. 3.6. In the single turn loop antenna as shown in Fig. 3.6 (a), the H-field is not uniform and most of the field is concentrated around the feed. On the other side, segmented loop antenna as shown in Fig. 3.6 (b) with a comparable loop length has a uniform field distribution across the antenna.

- Each segment of the loop is separated by capacitors, hence the current induced in the UHF loop by the surrounding HF loop can be more easily managed.

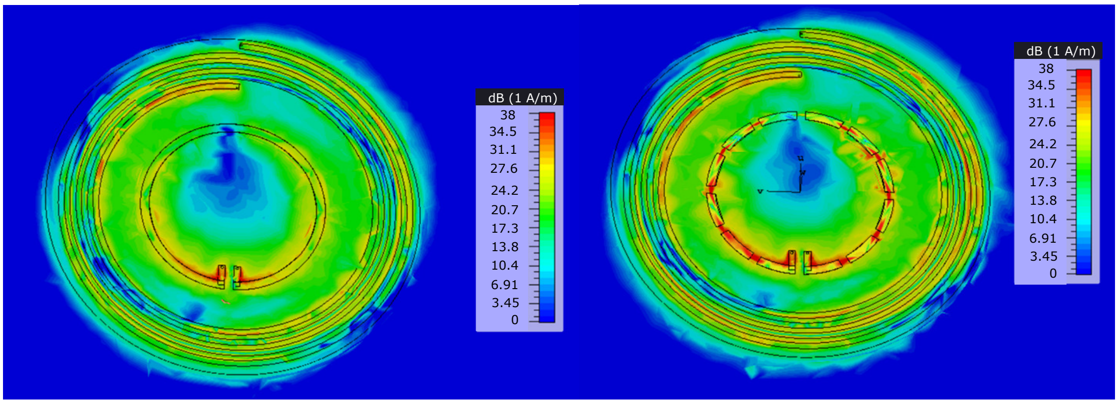

(a) (b)

Figure 3.6: (a) Simulated H-field distribution at 915 MHz across loop antenna. (b) Simulated H-field distribution at 915 MHz across segmented loop antenna.

The segmented loop diameter is 42 mm, with a trace width of 2 mm. In the design, one end of the segmented loop is connected to the ground plane through conductive via and the other end of the loop is connected to the feed through another conductive via. Murata 36 pF lumped capacitors (part number GRM1555C1H360GA01D) were used between each of the 11 segments. The capacitor value was chosen by a parameter sweep in CST to yield a uniform current distribution by compensating the phase shift along the loop, which leads to a more uniform H-field distribution while simultaneously suppressing the radiated E-field component and thus reducing the SAR in the adjacent tissue [111]. Capacitor package parasitics were significant and thus included in the model when performing the parameter sweep.

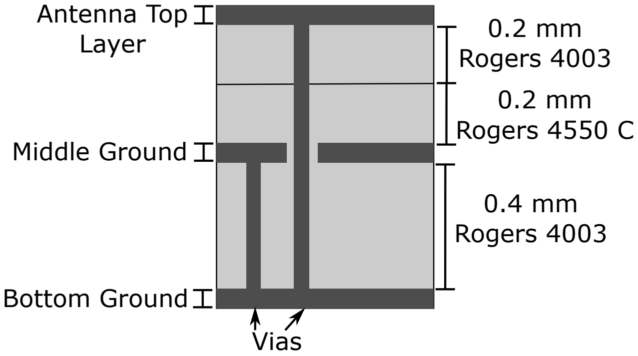

Figure 3.7: Layer stackup of implant antenna.

3.8 A 27 mm diameter 3 mm thick dual-band implant antenna device

As shown in Fig. 3.7, the implanted device consists of three metal layers and three dielectric layers. The top metal layer is used for the HF and UHF antenna structures, while the bottom copper layer is used for the matching components and to accommodate integrated data acquisition electronics. The top view of each metal layer is shown in Fig. 3.8. The middle layer is a ground plane separating the antenna structures on the top layer from the electronics on the bottom layer and helps in reducing interference between them. The implant stack supports both through-vias and blind-vias. Through-vias connect the top layer to the bottom layer at the feed points, and blind-vias tie ground nets on the bottom layer to the inner ground layer without penetrating the top layer.

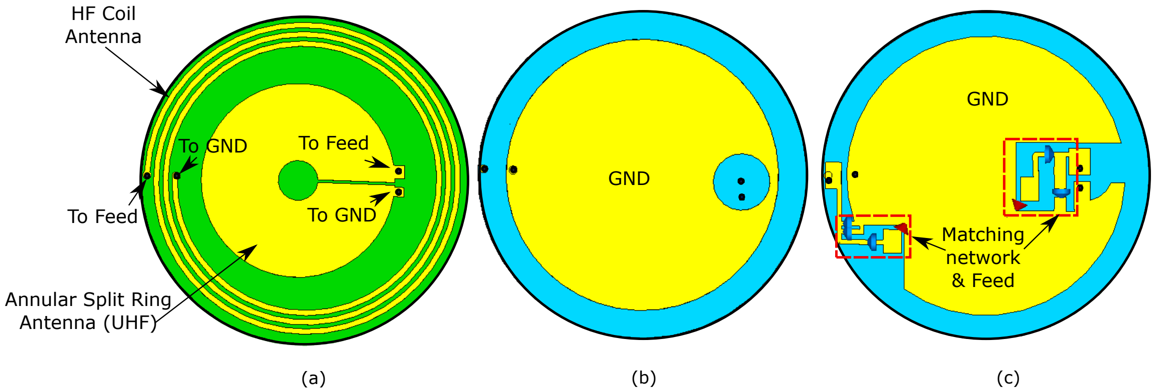

Figure 3.8: Implant PCB. (a) Top layer. (b) Middle layer. (c) Bottom layer.

3.8.1 Implant HF spiral loop antenna for WPT

The implant HF spiral loop antenna forms the outer annulus of the implant antenna similar to the external antenna board. It consists of three turns with inner radius 9.6 mm, outer radius 12.1 mm, trace width 0.4 mm, and inter-turn spacing 0.3 mm. As with the external loop antenna, these parameters were chosen via optimization using CST's frequency domain solver to maximize the efficiency given the lossy dielectrics of the layered bio-model. To obtain resonance at 13.5 MHz, a set of capacitors were connected between the feed and loop antenna as shown in Fig. 3.9.

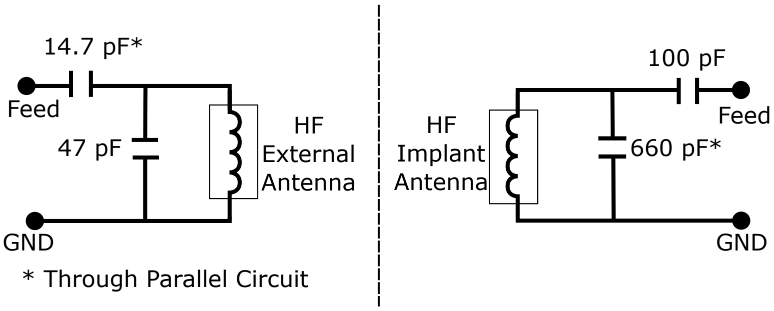

Figure 3.9: HF matching network for external and implant antennas.

3.8.2 Implant UHF split ring antenna for communication

The implanted UHF antenna consists of an annular split ring resonator. The diameter of the ring is 14.6 mm, with an inner circular slot of 1.78 mm diameter. The ring is split along a radius with a split gap of 0.2 mm forming the feed point. The split in the annular ring prevents the ring from forming a shorted turn that would otherwise be tightly coupled to the HF antenna surrounding it. This approach minimizes the unwanted loading and interaction between the HF and UHF antennas.

At 915 MHz simulated realized gain of the split ring antenna was -25 dBi and of the external segmented loop was -4 dBi. The main goals of designing implant and external UHF antennas were to provide short-range near field communication with low SAR and to have low coupling with the adjacent HF coil. Hence, antenna gain is not a significant factor in the design for this work.

As with the external antenna, lumped element matching networks as shown in Fig. 3.10 are employed to reduce the required board area compared to printed (e.g., microstrip) matching elements.

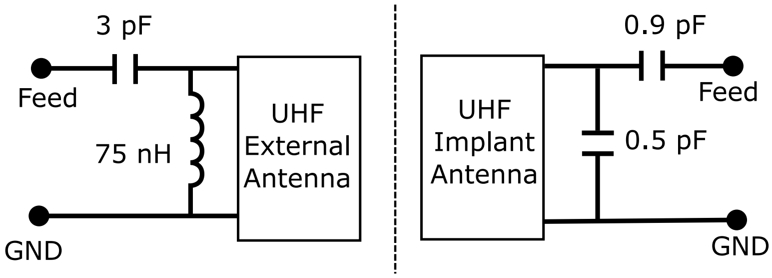

Figure 3.10: UHF matching network for external and implant antennas.

3.9 Interference between implant HF and implant UHF antennas

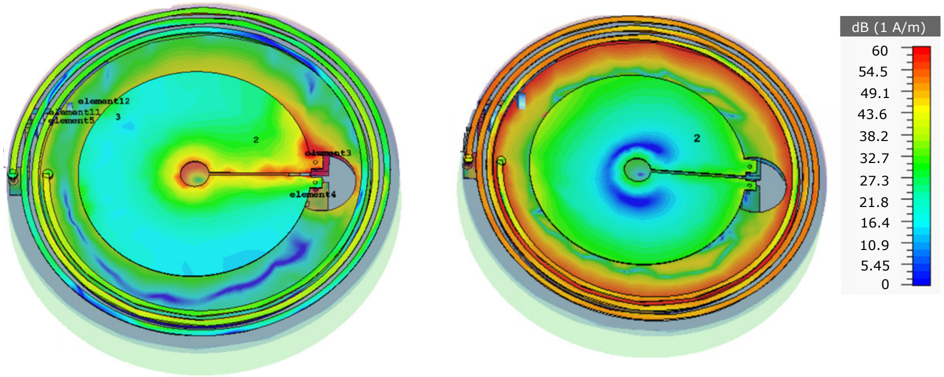

(a) (b)

Figure 3.11: Simulated time domain surface current. (a) Input signal to UHF loop at 915 MHz. (b) Input signal to HF loop at 13.5 MHz.

The implant board is designed to have low interference between HF and UHF antennas. In the UHF annular ring antenna, most of the current stays across the antenna feed and the slot as shown in Fig. 3.11 (a). When the HF loop antenna is excited, most of the surface current flows along the periphery of HF loop antenna as shown in Fig. 3.11 (b) and a very small amount of current (approx. 30 dB less than the peak current) flows to the UHF antenna.

Two methodologies were used to reduce interference :

- To reduce the coupling between two port, the feed of the antennas were placed at the opposite ends of the board,
- Optimal spacing was given between the two antennas, based on an optimization toolbox in CST to reduce surface current coupling.

Measured port-to-port coupling: To check the interference between the antennas, the HF antenna was connected to port 1 of a vector network analyzer (VNA), and the UHF antenna was connected to port 2 through another cable, and the transmission coefficient ($|S_{21}|$ dB) were measured between the antennas. The measured worst-case port-to-port mutual coupling was -43 dB ($|S_{21}|$ dB) in the 902-928 MHz band and -55.6 dB at 13.56 MHz.

3.10 SAR simulation

3.10.1 Simulated SAR at 915 MHz

The time-domain solver module in CST was used to calculate the SAR at the implant site when the external antenna was driven with the maximum expected transmitter power of 20 dBm at a frequency of 915 MHz. The SAR simulations were performed in a four-layer tissue model mentioned in Section 2.7.2. From a SAR point of view, the regulatory limits are driven by the UHF band, as tissue absorption at HF frequencies is much lower. As shown in Fig. 3.12, the peak UHF SAR value was 0.457 W/kg in 1 gram of average mass, which is well below the regulatory limit of 1.6 W/kg for human exposure. This figure also shows that most of the EM absorption occurred in the skin layer (top layer) and brain tissue (bottom layer) as compared to the fat and muscle layers (intermittent layers). This is because skin and brain tissues have higher water content than fat and muscle, which makes them lossier.

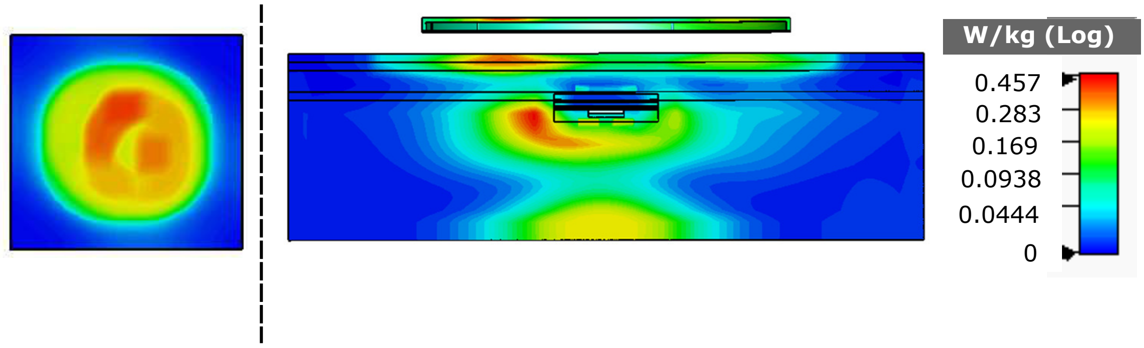

Figure 3.12: Simulated UHF SAR in four-layer bio-model. (Left) Skin-surface top view. (Right) Cross section.

3.10.2 Simulated SAR at 13.5 MHz

At 13.5 MHz, the simulated peak SAR value was 0.0175 W/kg averaged over 1 gram of tissue sample for the peak transmitted power of 30 dBm (Fig. 3.13), which is much smaller than 1.6 W/kg and much smaller than the UHF, as expected.

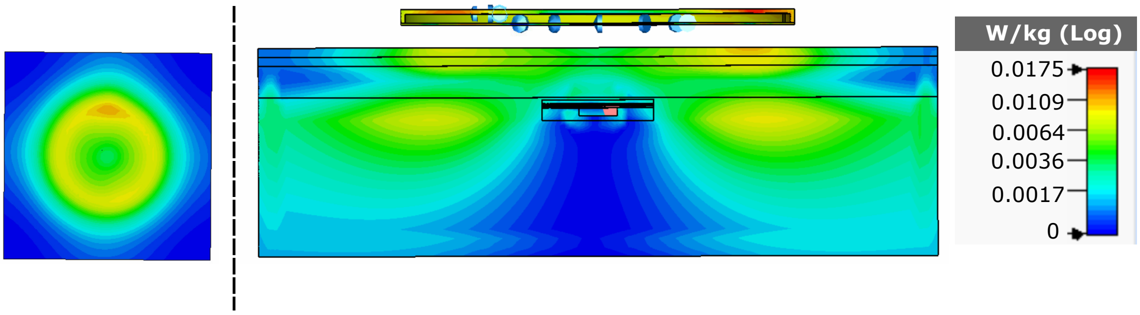

Figure 3.13: Simulated HF SAR in four-layer bio-model. (Left) Skin-surface top view. (Right) Cross section.

3.11 SAR improvement using multi-slot annular ring UHF implant antenna

The simulated SAR was unsymmetrical in biological tissues using annular split ring antenna, as shown in Fig. 3.12. This is because the surface current in implant antenna was concentrated around the area near feed and the slot (Fig. 3.11 (a)). Hence to improve current distribution, multiple slots can be designed on annular ring structure where the slot act as a capacitor. Fig. 3.14 (a) contains eight equally spaced slots in annular ring structure. The surface current is more uniform around the antenna as shown in Fig. 3.14 (b).

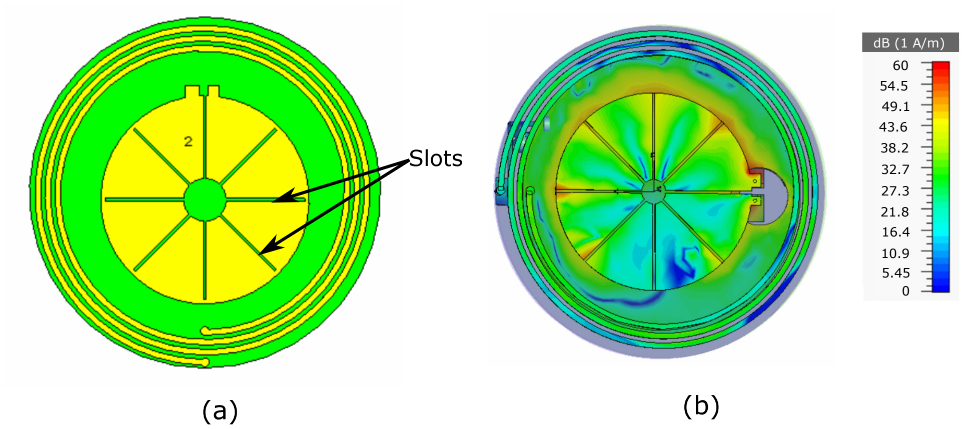

(a) (b)

Figure 3.14: Simulated time domain surface current at 915 MHz. (a) Annular ring structure with single slot. (b) Annular ring structure with multiple slots.

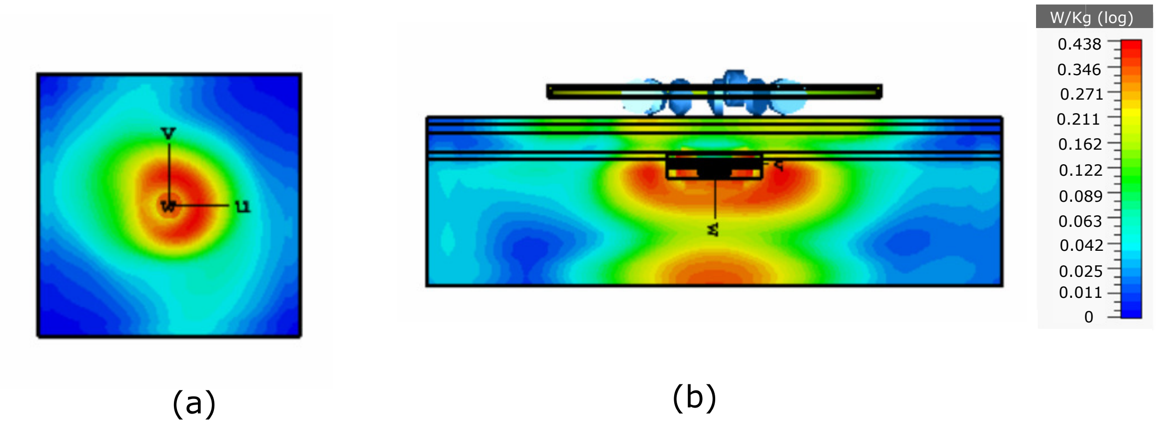

(a) (b)

Figure 3.15: Simulated SAR in four-layer bio-model for in the presense of annular ring structure with multiple slots. (Left) Skin-surface top view. (Right) Cross section.

At 915 MHz, the simulated peak SAR value was 0.44 W/kg averaged over 1 gram of tissue sample for the peak transmitted power of 20 dBm (Fig. 3.15). The SAR is more uniform in biological tissues and is smaller than the annular ring structure with a single slot (Fig. 3.12).

3.12 Encapsulation

Encapsulation is one of the most critical and crucial processes during the manufacturing of biomedical devices, as the encapsulating layer acts as a barrier between biological tissue and the implant device. This barrier is required to prevent leakage current from the implant device from flowing into the biological tissues and to protect human/NHP tissues from the corrosion of implant electronics and from PCB contaminations. The desired properties of an encapsulating material are soft material, long life, transparency for easy inspection, low ionic impurity, and material that can be easily cured and does not require high temperatures.

In this work, the implant PCB board is encapsulated in a biocompatible silicone polymer Dow Corning MDX4-4210. This biocompatible silicone was chosen because of its well-known material properties, long life, low surface tension, hydrophobicity, and excellent thermal stability. As mentioned in [112], the median lifespan of a silicone gel implant is 16.4 years. The adhesion life of silicone is highest when compared to Ag, Al, Cr, Cu, Fe, Ni, Pb, Sn, Ti and Zr, as mentioned in [113].

3.12.1 Encapsulation process

Two important factors to consider while making the encapsulate are as follows:

- Void-free encapsulate is essential as water can condense inside the voids, causing leakage current, and corrosion,

- Clean environment to avoid contamination in the encapsulation.

In this work, the following steps were performed during encapsulation:

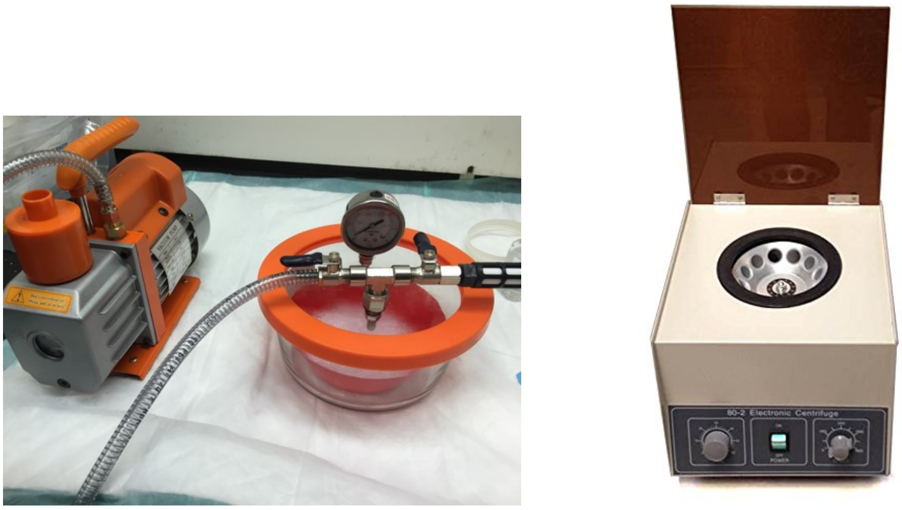

(a) (b)

Figure 3.16: Instruments used during the encapsulation process. (a) Vacuum chamber. (b) Centrifuge.

1. **Mixing:** One part of the curing agent was mixed with ten parts by weight of the base elastomer. The mixture was placed in a centrifuge tube which was then inserted in one of the slots of the Electric Medical Desktop Lab Medical Practice Centrifuge Machine, shown in Fig. 3.16 (b). The centrifuge was used for ten minutes at a rotation speed of 500 rpm. This method was utilized to remove air bubbles from the silicone mixture. If any bubbles remained, this centrifuging was repeated.

2. **Molding and de-airing:** A 27 mm diameter and 5 mm long plastic cylindrical tube closed at one side was used as a mold. A thin layer of silicone mixture was placed inside the mold slowly to avoid additional air bubbles. Then the implant board was set on the top of the silicone mixture with another thin layer of silicone mixture on the top of the implant board.

For a void-free encapsulate it is essential to remove entrapped air. The mold was placed in a 75 qt. vacuum chamber exposed to a vacuum of about 710 mm Hg (28 inches of mercury) for approximately three hours. During this process, the vacuum was released several times to break the bubbles. At the end of the process, the mold was kept stationary for 30 minutes to allow the remaining traces of air to escape from the material.

3. **Curing:** The mold was then removed from the vacuum chamber and placed inside an oven for two hours at a temperature of 55 °C. The end product is shown in Fig. 3.17 with no bubbles in the encapsulate. For testing the lifetime of silicone in the lab, the encapsulated implant board shown in Fig. 3.17 has been placed inside an airtight plastic container containing saline solution since January 2016. The performance of the implant device is same even after three years. This suggests that the silicone is performing as indicated and the devices can be expected to function for long stretches of time.

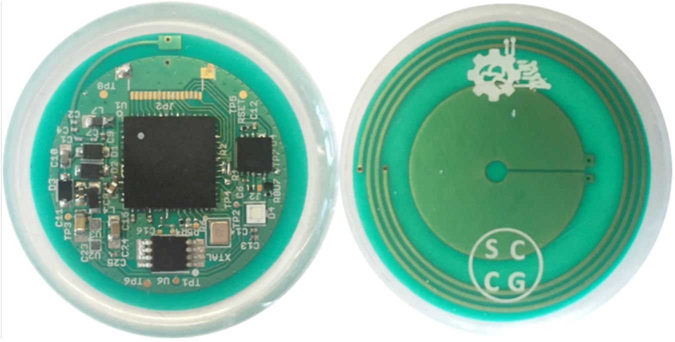

Figure 3.17: Implant PCB along with void-free bio-compatible silicone encapsulate. (Left) Bottom view. (Right) Top view.

3.13 Saline solution test setup

Antenna testing was performed using a plastic cylindrical tank with a diameter of 30.4 cm filled with 3 L of water and 2.73 grams of salt serving as a tissue proxy. The experimental setup is shown in Fig. 3.18. The implant antenna was protected from the saline solution by a thin ($\approx 70\mu$m) latex membrane and submerged to a depth of 1 cm below the surface of the liquid. Later in the experiments, the latex membrane was replaced with the silicone encapsulate. The implant antenna was connected to one port of VNA through a coaxial cable, and the external antenna was connected to other port of the VNA with another coaxial cable.

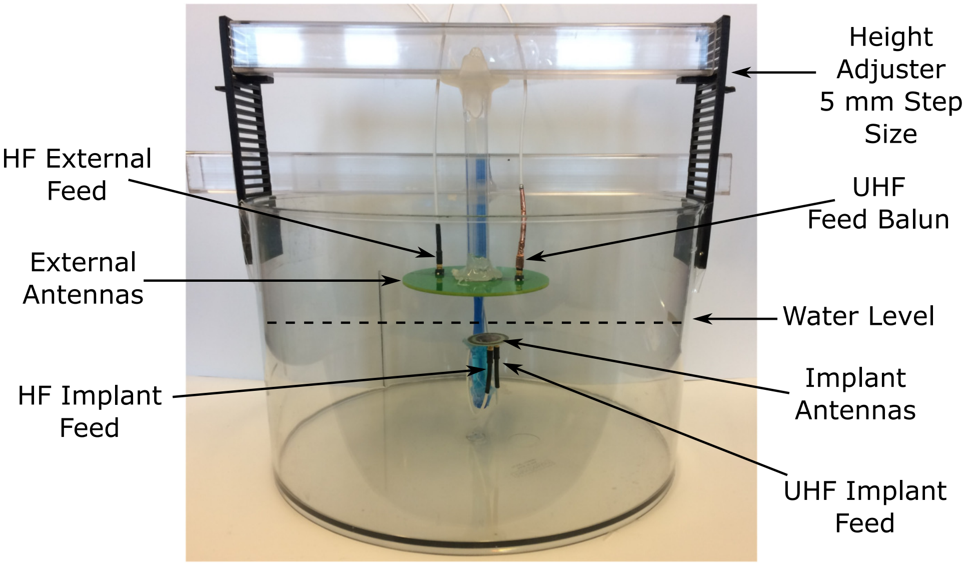

Figure 3.18: Photo of the saline solution experiment.

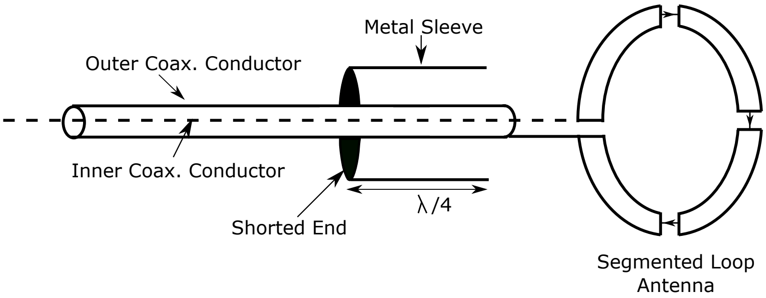

Figure 3.19: Diagram of sleeve balun designed for the external UHF segmented loop antenna.

A quarter wavelength long sleeve balun was designed at 915 MHz for the external segmented loop UHF antenna which was utilized to stop the leakage current flowing to the outer conductor of the coaxial cable. One end of the sleeve was short-circuited to the outer conductor of the coaxial cable, while another end of the sleeve was left open. This creates a high impedance between the sleeve and the outer conductor of the coaxial, which causes choking of the RF signal flowing from the antenna to the outer conductor of the coaxial cable. The block diagram of sleeve balun is shown in Fig. 3.19.

3.14 Saline test measurement results

The distance between the external antenna and the surface of the saline solution, which is referred to as an air gap in this thesis, was varied from 0 cm to 1.5 cm. The implant position was kept constant at 1 cm below the surface of the saline solution.

3.14.1 HF antenna performance

Fig. 3.20 shows S-parameter plots for the HF antennas measured at different air gaps starting from 0 cm to 1.5 cm. In the measurement plots, $|S_{11}|$ dB corresponds to the reflection coefficient for port 1 connected to the external antenna, $|S_{22}|$ dB corresponds to the reflection coefficient for port 2 connected to the implant antenna, and $|S_{21}|$ dB corresponds to the transmission coefficient. From Fig. 3.20 (a), the external antenna matching was poor when the external antenna was at the surface of the saline solution (0 cm air gap) because the external antenna is designed for an air gap between the skin surface and the external antenna. The antenna matching improved with the increase in the air gap. As shown in 3.20 (b), the implant and the external antenna coupling decreased with a larger air gap due to the increased path loss. As shown in Fig. 3.20 (c), the implant HF matching does not vary significantly as the air gap changed from 0.5 to 1.5 cm.

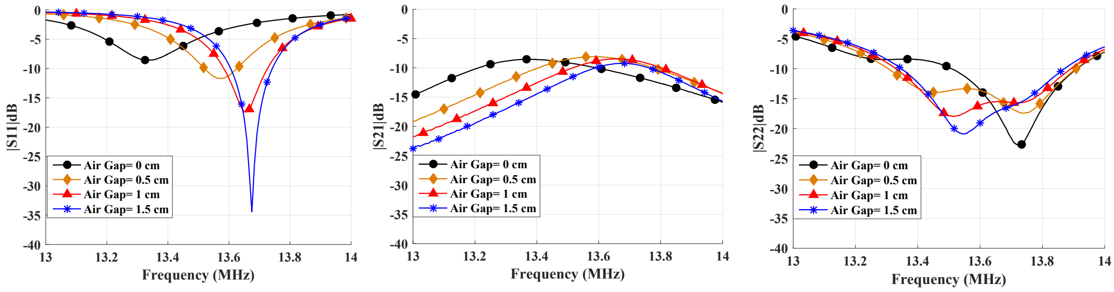

Figure 3.20: Measured performance of HF antenna system. (a) External antenna $|S_{11}|$ dB. (b) External to implant coupling $|S_{21}|$ dB. (c) Implant antenna $|S_{22}|$ dB.

The measured and simulated results in the saline tissue proxy are compared in Table 3.1, along with the simulated results in the saline model and the four-layered bio-model. The bio-model indicates that the expected performance in the layered tissue will be somewhat better than that in the saline tissue proxy due to lower resistive losses in the protein and fat content of the tissue compared to that of the saline solution.

Table 3.1: Measured vs. simulated performance at 5 mm nominal air gap for HF antennas

	Measured (Saline)	**Simulated (Saline)**	**Simulated (Layers)**
Implant -10 dB BW (MHz)	13.3-13.9	13.46-14.02	13.43-13.88
External -10 dB BW (MHz)	13.52-13.62	13.52-13.7	13.47-13.98
Ins. Loss (dB), 13.56 MHz	8	6	6.8

3.14.2 UHF antenna performance

The measured results for UHF antennas showed a trend similar to that of HF antennas mentioned in the above sub-section. For the air gap = 0 cm, the external UHF antenna matching was poor and the antenna matching improved with the increased air gap, as shown in Fig. 3.21 (a). As shown in Fig. 3.20 (b), the implant and the external antenna coupling decreased with the increase in the air gap due to the increased path loss. There is approx. 8 dB reduction in coupling between the antennas from 0.5 to 1.5 cm, measured at 915 MHz.

As shown in Fig. 3.20 (c), the implant matching does not vary significantly as the air gap changed from 0 cm to 1.5 cm.

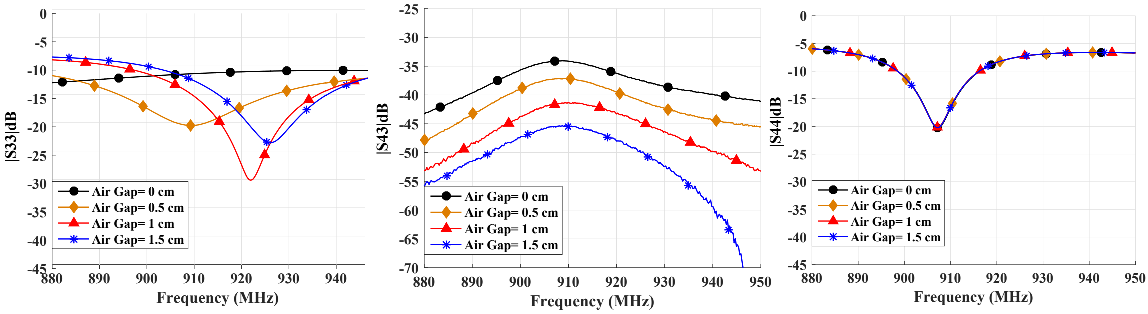

Figure 3.21: Measured performance of UHF antenna system. (a) External antenna $|S_{33}|$ dB. (b) External to implant coupling $|S_{43}|$ dB. (c) Implant antenna $|S_{44}|$ dB.

Table 3.2: Measured vs. simulated performance at 5 mm nominal air gap for UHF antennas

	Measured (Saline)	**Simulated (Saline)**	**Simulated (Layers)**
Implant -10 dB BW (MHz)	898-916	908-916	906-917
External -10 dB BW (MHz)	870-955	891-936	889-932
Ins. Loss (dB), 910 MHz	37.65	38	25.7

The measured and simulated results in the saline tissue proxy at the UHF band are compared in Table 3.2, along with the simulated results in the four-layered bio-model. Similar to the performance of HF antennas (Table 3.1), the simulated insertion loss is smaller for the UHF antennas in bio-layered model as compared to simulated and measured results in the saline tissue.

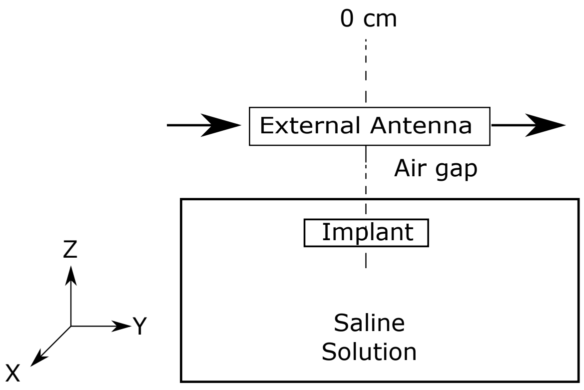

Figure 3.22: Block diagram of the lateral misalignment experiment.

3.14.3 Lateral misalignment

It is essential to examine the performance of the antenna system for different lateral misalignments between the implant device and the external device. In this setup, the external antenna was moved laterally along the Y-axis, while the saline container and the implant were kept stationary. The experimental block diagram is shown in Fig. 3.22. In the setup, 0 cm corresponds to the center of the external PCB aligned to the center of the implant board along the Y and X-axis.

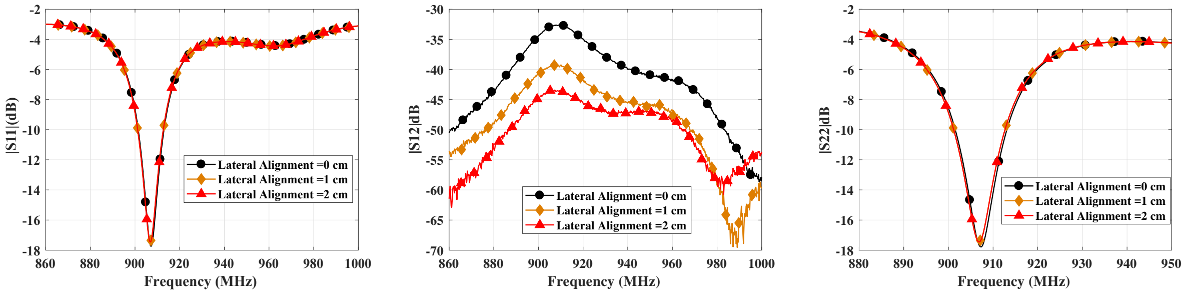

(a) (b) (c)

Figure 3.23: Lateral misalignment at 0.5 cm airgap for UHF antennas. (a) External antenna $|S_{11}|$ dB. (b) External to implant coupling $|S_{12}|$ dB. (c) Implant antenna $|S_{22}|$ dB.

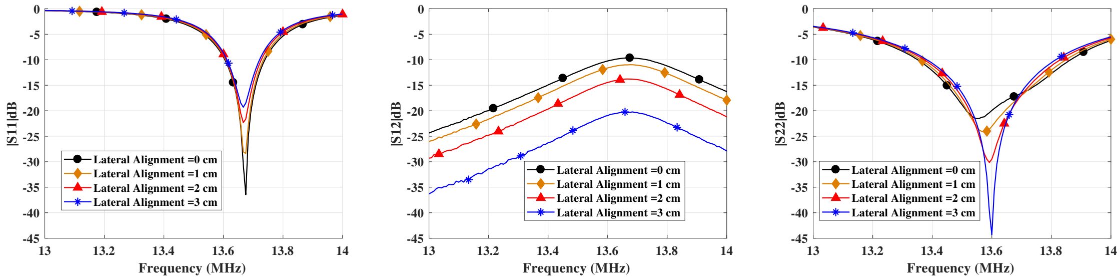

(a) (b) (c)

Figure 3.24: Lateral misalignment at 1.5 cm airgap for HF antennas. (a) External antenna $|S_{11}|$. (b) External to implant coupling $|S_{12}|$. (c) Implant antenna $|S_{22}|$.

From Fig. 3.23 (a) & (c) and Fig. 3.24 (a) & (c), it can be concluded that the matching of the HF and UHF antennas does not change significantly with a lateral misalignment from 0 cm to 3 cm. As shown in Fig. 3.23 (b) and Fig. 3.24 (b), the coupling was reduced by approximately

10 dB from 0 cm to 3 cm. One solution to solve lateral misalignment issue could be to design an array of the external side antennas instead of using a single one, similar to the work shown in [114].

3.14.4 HF power transfer efficiency

The efficiency of the HF wireless power link can be calculated using the transducer gain formula [74]. The transducer gain G_T is the ratio of power delivered to the load P_L, to the power available from the source P_S, and can be derived from

$$G_T = \frac{P_L}{P_S} = \frac{|S_{21}|^2 \times (1-|\tau_S|^2) \times (1-|\tau_L|^2)}{|1-\tau_S \tau_{in}|^2 \times |1-S_{22}\tau_L|^2} \tag{3.6}$$

where

$$\tau_{in} = S_{11} + \frac{S_{12} \times S_{21} \times \tau_L}{1 - S_{22} \times \tau_L} \tag{3.7}$$

In this, $\tau_L = (Z_L - Z_0)/(Z_L + Z_0)$ is the reflection coefficient from the load, $\tau_S = (Z_S - Z_0)/(Z_S + Z_0)$ is the reflection coefficient from the source, Z_0 is the characteristic impedance, Z_L is the load impedance, Z_S is the source impedance, and τ_{in} is the reflection coefficient from the input of the two-port network.

Using Eq. 3.6, HF efficiency can be obtained at different frequencies. Efficiency based on the measurement results is shown in Fig. 3.25. From Fig. 3.25, it can be concluded that the HF power transfer efficiency decreases with an increase in the air gap. The link efficiency values obtained in the experiment were 19 %, 17 % and 11 % at a frequency of 13.5 MHz measured at an air gap of 0 cm, 0.5 cm and 1.5 cm, respectively.

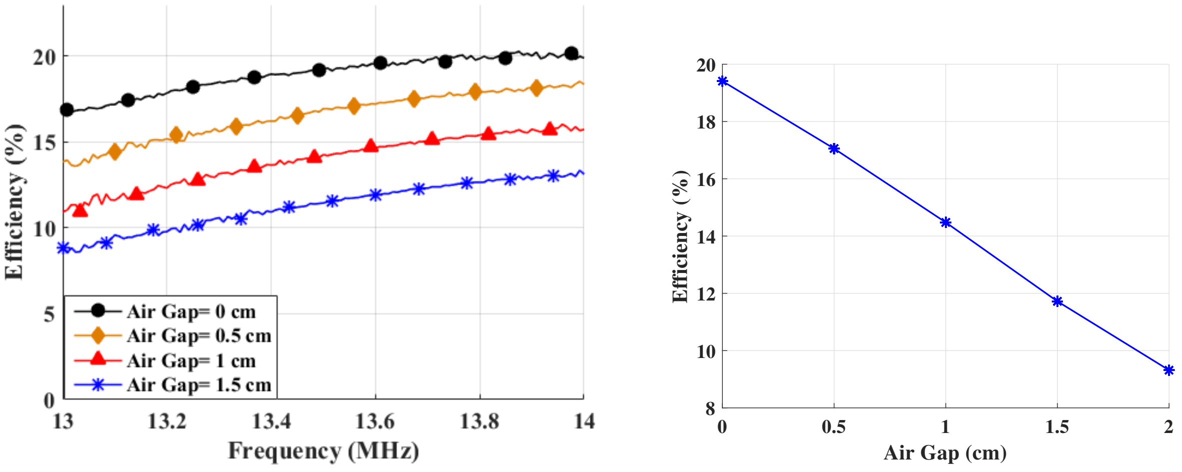

(a)

(b)

Figure 3.25: (a) Measured HF efficiency vs. frequency for different air gaps. (b) Measured HF efficiency vs. air gap.

3.15 Communication experiments in saline solution using pre-recorded neural signals

A benchtop setup was deployed as shown in Fig. 3.26 to characterize the performance of the backscatter communication link. Experiments were performed in collaboration with Eleftherios Kampianakis, using saline solution (0.91 grams of NaCl per liter of distilled water) acting as a tissue proxy in a styrofoam cup filled to the height of 6 cm. The external antenna was placed at an air gap of 0.5 cm from the saline surface. In the setup, a 3D-printed fixture was used to adjust the air gap between the external antenna and the surface of saline solution. The implant antenna was placed fixed at a depth of 1 cm below saline surface. The implant board was connected to a neural/EMG recording IC [115] capable of supporting up to 10 neural and 4 electromyogram (EMG) channels with a sampling rate of 26.10 kHz for the neural channels and 1.628 kHz for the EMG channels. The complete antenna setup was placed in a Faraday cage in order to shield the experiment from external interference and RF electronics.

For neural telemetry, prerecorded neural signals were fed into the implant with an Agilent

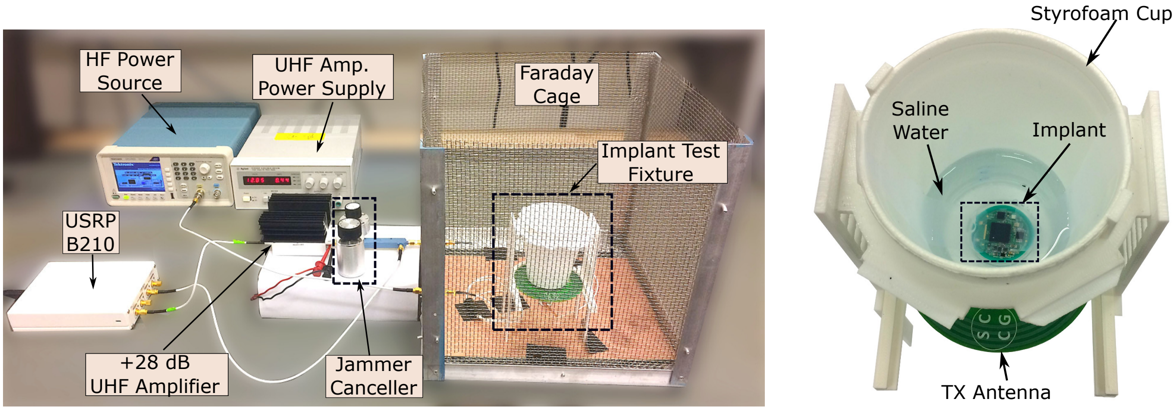

Figure 3.26: (Left) Implanted communication system testbed. (Right) 3D-printed fixture for varying the air-gap and implant depth (*image courtesy of Eleftherios Kampianakis*).

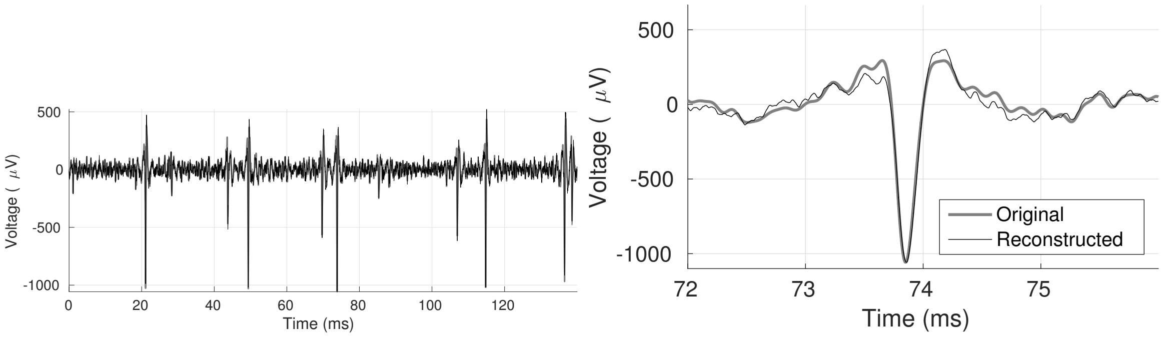

Figure 3.27: Original vs. reconstructed neural signal. (Left) Complete reconstructed and original waveforms. (Right) Zoomed-in depiction of one of the spikes that occur at approx. 74 ms (*image courtesy of Eleftherios Kampianakis*).

33500B arbitrary waveform generator (AWG). These prerecorded neural signals were captured from the forearm area of left primary motor cortex of a monkey Macaca nemestrina by our colleagues under an IACUC approved protocol.

For the validation of communication link, PER measurements were performed which is the ratio of erroneous packets to total transmitted packets. Where the erroneous packet is the packet with two or more bit errors. In this work, a successful communication was achieved from the implant device to the external device with a backscatter uplink rate of 5 Mbps at an implant depth of 1 cm in a saline solution without any data dropouts [61] and PER less than 0.19 % till implant depth of 3 cm for an input power of -91 dBm. PER measurements were first made as a function of available channel power by counting cyclic redundancy check (CRC) errors, after Hamming decoding, from 25000 packets.

The comparison between the pre-recorded signal and the signal obtained from the proposed system are shown in Fig. 3.27. On the left side of the figure, the time domain representation of the entire 130 ms of data is plotted, while on the right a zoomed-in view depicts a single spike. The pre-recorded signal and the reconstructed signal obtained from the proposed implant system are in agreement (as shown in Fig. 3.27 (Right)).

3.16 WPT experiment in saline solution

For WPT, the implant HF antenna was connected to the matching circuit, which was connected to the power rectifier. Details of the power rectifier are mentioned in [61], in which the output was regulated using low-dropout (LDO) regulators to provide 3.3 V and 1.8 V rails. A 3.3 V regulator powers the photo-stimulator and a 1.8 V regulator powers the implant recording IC. A block diagram of a WPT system at the implant side is shown in Fig. 3.28.

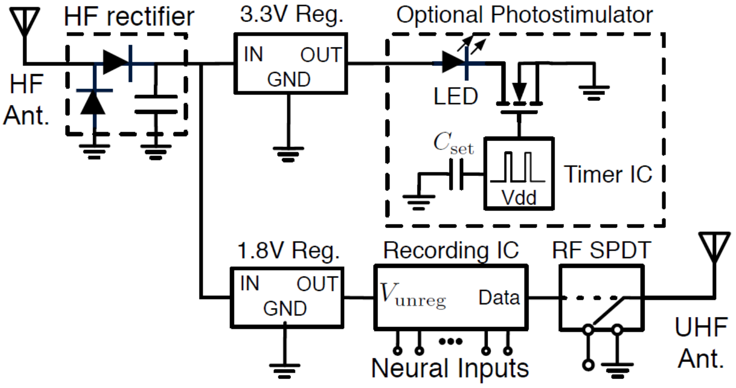

Figure 3.28: Block diagram of a WPT implant (*image courtesy Eleftherios Kampianakis)*.

As shown in Fig. 3.29, the HF loop antenna is capable of turning on the photo-stimulator when the loop antennas were separated at a distance of 4 cm and at a peak input voltage of 20 V from a signal generator connected to the external antenna. In this setup, a human

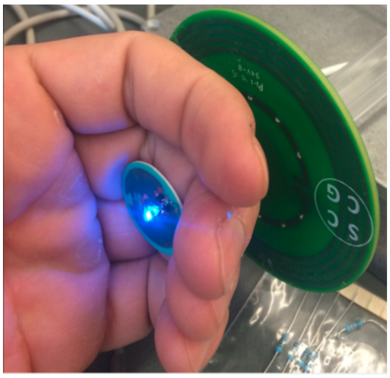

Figure 3.29: WPT experiment.

hand was placed between the external and the implant devices to mimic biological tissue in between them.

3.17 Chicken muscle experimental setup

In the setup, the implant PCB was placed inside a 1 cm thick chicken muscle, and the external antenna system was placed 1 cm away from chicken muscle. The photo of the setup is shown in Fig. 3.30. For the measurement, implant antenna was connected to port 1 of the VNA while the external antenna was connected to port 2. S-parameters were measured for the estimation of the bandwidth and the coupling between the antennas.

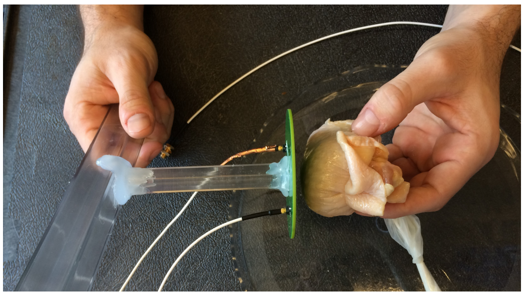

Figure 3.30: Photo of the experimental setup with chicken muscle.

3.18 Chicken muscle measurement results

Fig. 3.31 shows the measurement results with implant antenna in chicken muscle. $|S_{21}|$ dB measured -30 dB at 915 MHz and at -12 dB at 13.5 MHz. However, in the saline experiments, $|S_{21}|$ dB was -37.5 dB and -12 dB at 915 MHz and 13.5 MHz, respectively. We found 7.5 dB better communication link in the UHF band using chicken muscle as compared to the saline solution while HF link remained the same. As expected from the simulation results of saline phantom and a layered model shown in Table 3.2 and Table 3.1, the measured performance in chicken muscle is better than the saline solution at UHF band. The measured results at HF band using saline solution and chicken muscle are comparable due to negligible RF absorption in tissue proxy.

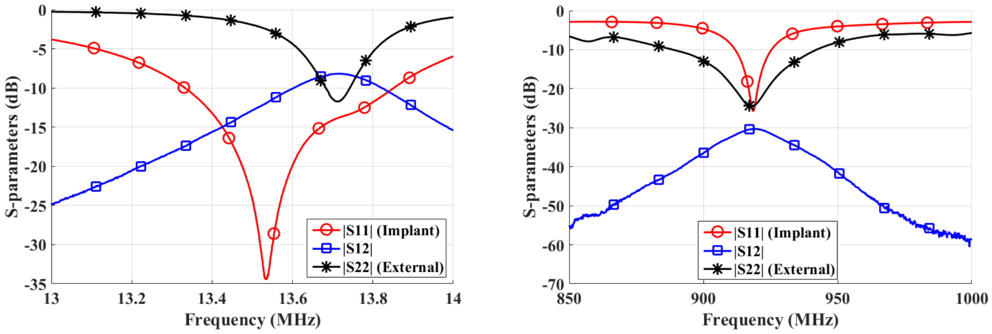

(a) (b)

Figure 3.31: Measured S-parameters from chicken muscle experiment. (a) At HF band. (b) At UHF band.

3.19 Conclusion

In this chapter a dual-band (HF and UHF (13.56 MHz and 902-928 MHz)) antenna system for a chronic implanted neural recording and/or stimulation devices consisting of implant-side and external antennas were presented. The antennas are intended for dual-band systems where power is supplied to the implant via inductive coupling in the HF band, while data is transferred via UHF near-field coupling. The antenna system consists of an implant-side antenna of 27 mm diameter and 3 mm thickness (including silicone encapsulate) which is a constraint by the dimension of the smallest skull flap. The external antenna is designed for the dimensions of 85 mm diameter and 3 mm thickness. The WPT loop antennas and communication antennas were designed and optimized in CST MWS software using the frequency domain solver.

We presented simulation results for the antenna performance and the time-domain SAR in a layered tissue model, as well as the experimental confirmation of the antenna performance in a saline tissue proxy and a chicken muscle. The peak SAR value was 0.457 W/kg at 915 MHz and 0.017 W/Kg at 13.5 MHz in 1 gram of average mass, which is below the regulatory limit of 1.6 W/kg for human exposure. The implant antenna board was designed for low mutual port-to-port interference between implant HF and implant UHF antennas. The measured worst-case port-to-port mutual coupling was -43 dB in the UHF ISM band (902-928 MHz) and -55.6 dB at 13.5 MHz.

With an implant depth of 1 cm and an air gap of 5 mm, the HF power link had a 17 % measured power transfer efficiency using saline solution. The communication link measured at 915 MHz was 7.5 dB better in chicken muscle as compared to saline solution. A successful communication link was achieved using proposed UHF antenna system with a data rate of 5 Mbps at an implant depth of up to 1 cm.

CHAPTER 4

DUAL-BAND ANTENNA SYSTEM FOR LARGE NHPS IN REVERBERANT METAL CAGES

*The chapter is an adapted version of [63, 64, 65].

4.1 Introduction

This chapter presents a dual-band (HF and UHF) antenna system for large non-human primates (NHPs) to enable neuroscience research on animals moving freely in a caged environment. Additionally, we present a characterization of the channel transfer function in a reverberant metal housing cage and an *in-vivo* 16 channel neural recording of an anesthetized pigtail macaque in a benchtop setup. The NHP considered in this work is a pigtail macaque (Fig. 4.1). This species is commonly used in neuroscience experiments [9, 116, 117].

It is challenging to design antennas to operate inside a metal cage. When EM waves propagate inside the cage, waves bounce back and forth from the metal walls, creating dense multipath. Hence,the cage can be considered a reverberant cavity. This phenomenon

Figure 4.1: Image of macaque (image licensed under CC BY-SA 3.0 and taken from [6]).

results in many deep nulls in the communication channel and impairs the backscatter signal, creating a challenge for an antenna to be able to perform efficiently throughout the volume of the cage.

The overall system consists of the following devices: (1) a cage device mounted on the inner top wall of the housing cage, and (2) a BCI device installed external to NHP's head. Both the devices contain HF and UHF band antennas, where HF antennas are for WPT, and UHF antennas are for backscatter communication. The BCI antenna PCB is a two layer board designed on a 1.6 mm thick FR-4 substrate with an outer diameter of 5.5 cm to be fit inside the head-stage canister containing a communication board, battery, and a neural recording chip Neurochip 3 that is the successor to the Neurochip 2 [118]. The BCI antenna device is designed for low SAR to avoid tissue heating and for small port-to-port mutual coupling to prevent unwanted interference between the power and communication systems.

In this chapter, two antennas are proposed for BCI device: (a) ceramic antenna, and (b) a μSP antenna. The μSP antenna has the following advantages over proposed ceramic antenna such as: (1) smaller size, (2) wider bandwidth, and (3) ability to achieve communication with higher data rates. However, better communication link with a lower insertion loss can be achieved from the ceramic antenna due to its higher gain.

4.2 Layout of the housing cage of a pigtail macaque

To understand EM field distribution and channel transfer function inside the cage, we did several experiments in the lower chamber of the housing cage of a pigtail macaque as shown in Fig. 4.2. The cage is divided into two chambers (top and bottom) by a horizontal metal grating. The dimensions of the lower chamber are 93 cm × 93.4 cm × 77 cm (height × width × length). The lower chamber has an 18 cm long metal seat at a height of 15 cm.

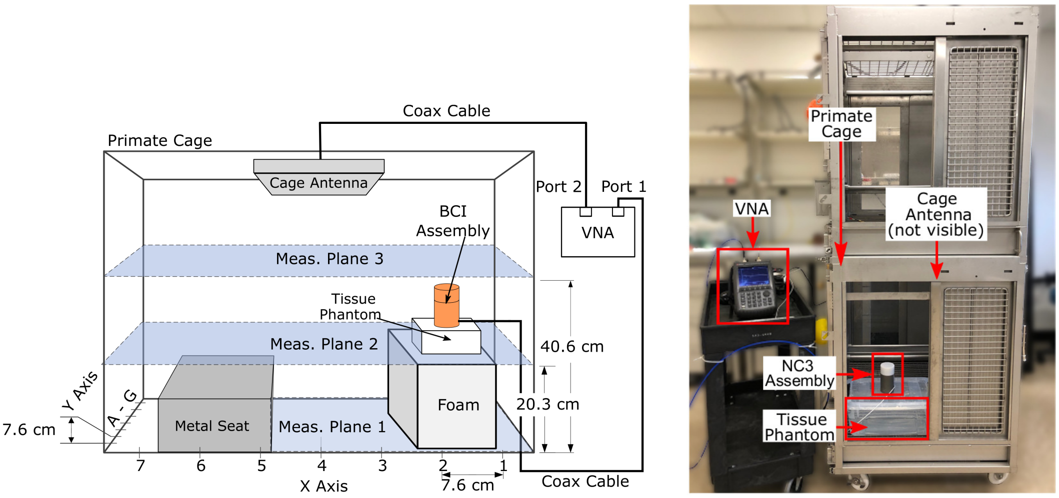

(a)

(b)

Figure 4.2: (a) Block diagram of setup used in lower chamber of the cage *(image courtesy of James Rosenthal)*. (b) Photo of the test setup used to characterize the wireless channel of the NHP cage.

The walls of the cage are built with square metal mesh with a mean grid size of 2.5 cm which is more than 10 × smaller than the shortest wavelength in the UHF band ($\lambda \approx 32.3$ cm) as well as the shortest wavelength of the HF band ($\lambda \approx 220$ cm). Based on the dimensions, the cage walls can be viewed as an impenetrable metal wall for HF and UHF in-band signals. One of the vertical sidewalls of the lower chamber contains 23.4 cm long, 60.7 cm high, clear poly-carbonate window. The EM environment inside the cage is different from fully enclosed Faraday cage, because the length and height of the window are much greater than the wavelength of the UHF band, resulting in leakage of UHF EM waves from the cage to outside. In contrast, EM waves do not leak outside a fully enclosed Faraday cage.

4.2.1 Communication challenges due to reverberant cavity

Several simulations were performed in CST MWS to analyze field distribution inside the cage at different horizontal planes. For simulations, the primate cage was modeled with aluminum material, and the cage-mounted UHF patch antenna was modeled inside the top wall of the cage, as shown in Fig. 4.3. A Sinusoidal signal was provided to the patch antenna as an excitation signal with a peak power of 1 W.

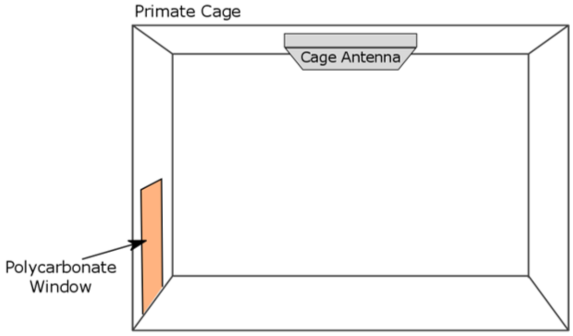

Figure 4.3: Model used in the simulation for the estimation of E-field inside the cage.

Fig. 4.4 shows simulated time-domain E-field plots at 923 MHz along the height of the housing cage, starting from the lower base to the upper metal wall in 11.6 cm increments. The black rectangular line shown in the sub-images corresponds to the cage boundary. Simulation results showed that the E-field distribution and locations of deep nulls vary drastically from one height to another. The randomness of field distribution inside the cage, as shown in the simulation results, suggest that it challenging to design an antenna which performs efficiently throughout the entire volume of the cage. For the case when NHP is inside the cage, the field distribution will be even more chaotic.

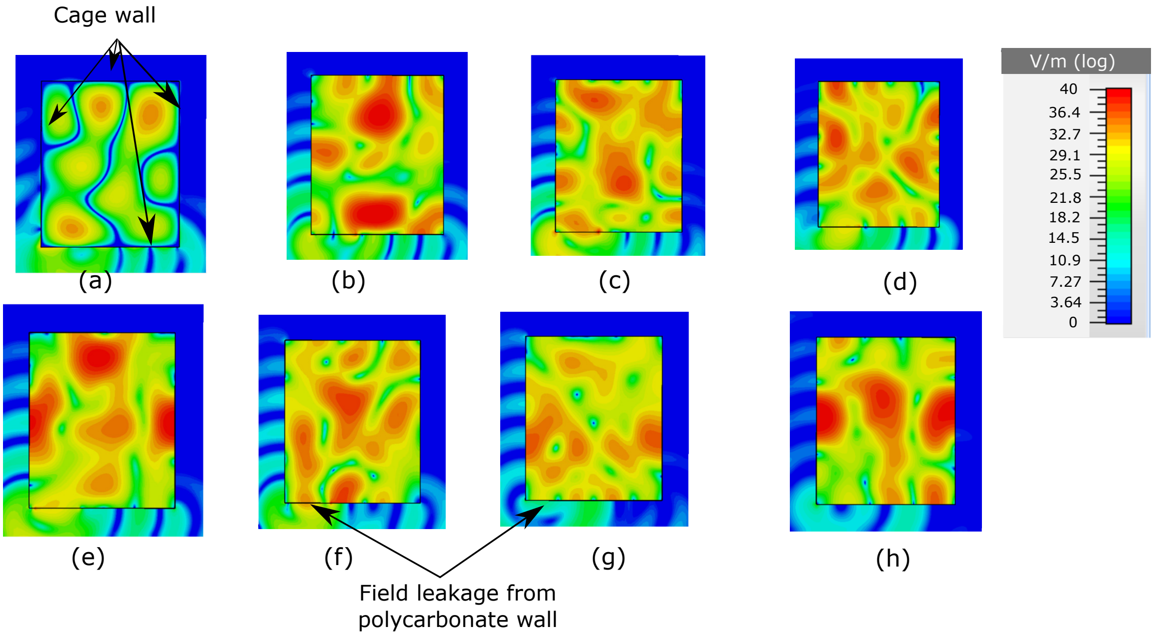

Figure 4.4: Simulated time domain E-field slices at 923 MHz, inside the cage starting from lower base of the cage chamber with the increment height of 11.6 cm up to the top of the chamber.

4.3 Link budget characterization

The round-trip link budget for the backscatter system, shown in Fig. 4.5 can be summarized as follows:

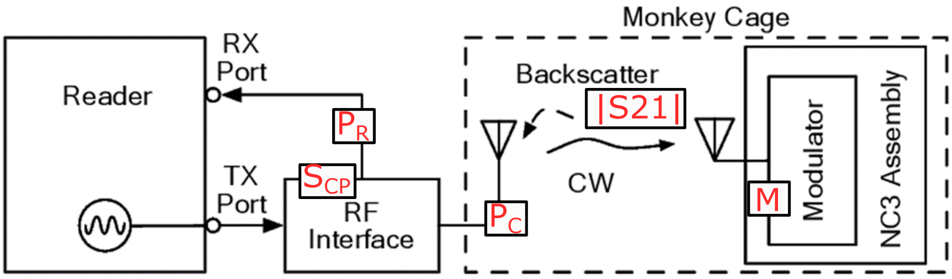

Figure 4.5: Block diagram of the system with link budget parameters *(image courtsey: Eleftherios Kampianakis)*.

$$P_R = P_C + 2 \times S_{21} + M - S_{\text{cp}} \tag{4.1}$$

where P_R is the received power at the cage-side antenna in dBm, P_C denotes the carrier power from the cage antenna, S_{21} is a transmission coeficient which is a function of various parameters (such as frequency, geometry, and electric and magnetic field distribution), M is a modulation factor imposed by the symbol-dependent change in modulator impedance as seen by the BCI antenna (akin to the free-space differential RCS) [119], and S_{cp} denotes the losses involved in the RF interface due to the coupler and cabling.

4.3.1 Link budget in the cage

The RF interface which was designed by Eleftherios Kampianakis and James Rosenthal in [63] indicates measured losses (S_{cp}) of 12 dB and a receiver sensitivity of -86 dBm. Fig. 4.6 (a) shows the measured S_{11} values across the UHF ISM band (902-928 MHz), corresponding to four switching states of the RF switch using a calibrated VNA. The four different switch states form a constellation on the Smith chart which corresponds to the four different symbol phases of the quadrature phase shift keying (QPSK) signal [115]. Modulation factor (M) = 23.9 dB was calculated for the smallest symbol distance present in the constellation.

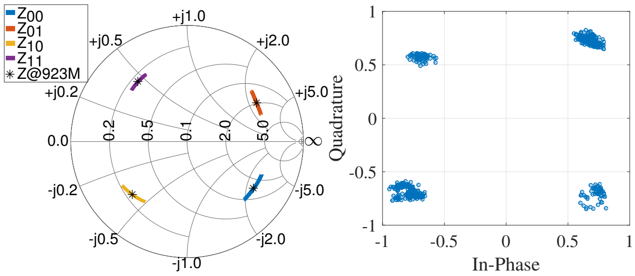

(a) (b)

Figure 4.6: (a) S_{11} measurements of the QPSK backscatter modulator for 4 different impedance states. (b) Symbol constellation recorded over 5,000 symbol periods *(image courtsey: Eleftherios Kampianakis)*.

Based on these calculations and the measured sensitivity of the receiver system, any insertion loss (which is absolute of transmission coefficient S_{21} dB) higher than 30 dB will result in a 100 % PER for a receiver sensitivity of -86 dBm. This suggests that telemetry packets may be lost at the locations inside the cage where the insertion loss is higher than 30 dB. The parameters used for the calculation of the link budget are summarized in Table 4.1.

Table 4.1: Link budget parameters for backscatter communication inside the cage

Parameter	**Value**
Maximum cage-side antenna power (P_C) (dBm)	10
M (dB)	-23.9
Losses in BCI circuit (S_{cp}) (dBm)	12
Receiver sensitivity (dBm)	-86
Calculated S_{21} (dB)	-30

4.4 Cage side antenna system: HF loop antenna and a commercial UHF patch antenna

The following antennas were chosen to be placed inside the top wall of the cage: (a) a commercially available UHF right-hand circularly polarized (RHCP) Laird Technologies S9028PCR patch antenna, and (b) a high-Q printed spiral loop antenna designed for the HF band. Since freely moving animals may stand in any orientation relative to the cage antenna, the circularly polarized antenna is the best choice to reduce signal losses from polarization mismatch. The commercial UHF patch antenna has a -10 dB bandwidth of 26 MHz (902-928 MHz) [120]. The reported antenna gain is 8 dBic with a 70° beamwidth, and its overall dimensions including the plastic casing are 25.8 cm x 25.8 cm x 3.2 cm (length x width x height). ‘WiBotic’ HF transmitter loop antenna is proposed to be used as an HF cage antenna [121].

4.5 Layout of head-stage BCI assembly

The proposed BCI antennas are designed to fit inside a 3.7 cm long, 5.6 cm inner diameter Teflon cap connected to an 8.5 cm long titanium (Ti) tube enclosure fabricated to be mounted on top of NHP's skull. The enclosure contains a communication PCB, a power rectifier PCB, and a neural recording chip Neurochip 3. Together, these are referred to as the BCI assembly in this thesis. A block diagram of BCI assembly is shown in Fig. 4.7.

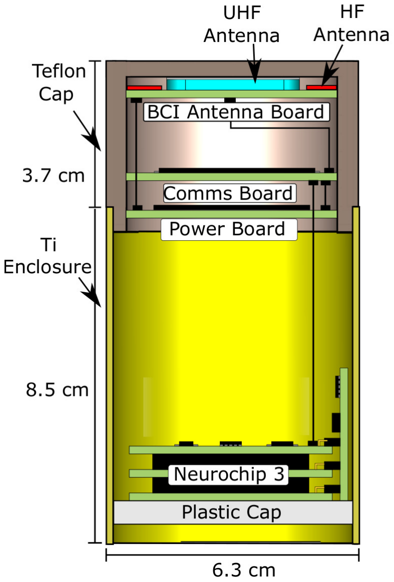

Figure 4.7: Layout of the BCI assembly.

4.6 Design 1: BCI antenna system using narrow-band ceramic UHF patch antenna

The BCI antenna PCB shown in Fig. 4.8 is a two-layer board designed on a 1.6 mm thick FR–4 substrate with an outer diameter of 5.5 cm and 30 μm copper plating. The top side of PCB contains the following: (1) a circularly shaped ground plane with a radius of 1.5 cm bonded to the ground plane of an Abracon APAE915R2540ABDB1-T ceramic patch antenna, and (2) HF loop, outer annulus to the ceramic antenna. The ceramic patch architecture was chosen because of the good trade-off between its small size and high realized gain; its dimensions are 2.5 cm × 2.5 cm × 0.4 cm (length × width × height).

An HF loop antenna was designed outer to the UHF ground with the following design parameters: 4.95 turns, 0.7 mm trace width, and 0.8 mm turn spacing. These parameters were obtained using genetic optimization in a frequency domain solver. The bottom side of the PCB consists of a UHF balun, UMC coaxial connectors, and 82 pF in series to HF loop for self-resonance at 13.5 MHz, as shown in Fig. 4.8 (b).

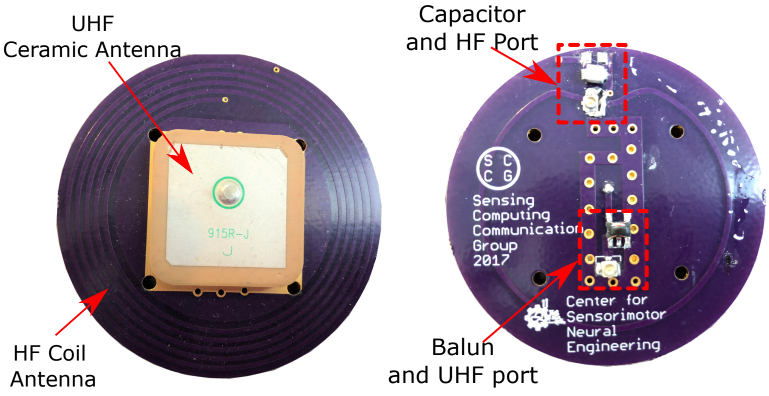

(a) (b)

Figure 4.8: (a) Top view showing the locations of UHF ceramic antenna and HF loop antenna. (b) Bottom view showing the locations of balun, series capacitor to HF loop, and UMC connectors.

4.7 Design 1: BCI antenna simulation results

The performance of the BCI antenna PCB was evaluated using the FEM solver built into CST MWS. Simulations were performed for the BCI antenna PCB placed within the Teflon cap connected to the Ti enclosure, similar to the layout shown in Fig. 4.7. Simulated -10 dB bandwidth of the UHF ceramic antenna is approximately 1 MHz centered at 923 MHz. The maximum simulated realized gain of the ceramic antenna along with the Teflon cap and Ti enclosure, is -0.4 dBi at 923 MHz as shown in Fig. 4.9 (c). The gain of the ceramic antenna is maximum at a plane perpendicular to the antenna and minimum at a plane parallel to it.

Simulated frequency domain surface currents for HF and UHF antennas are shown in Fig. 4.9 (a) and (b). When the HF antenna is excited, most of the surface current is confined

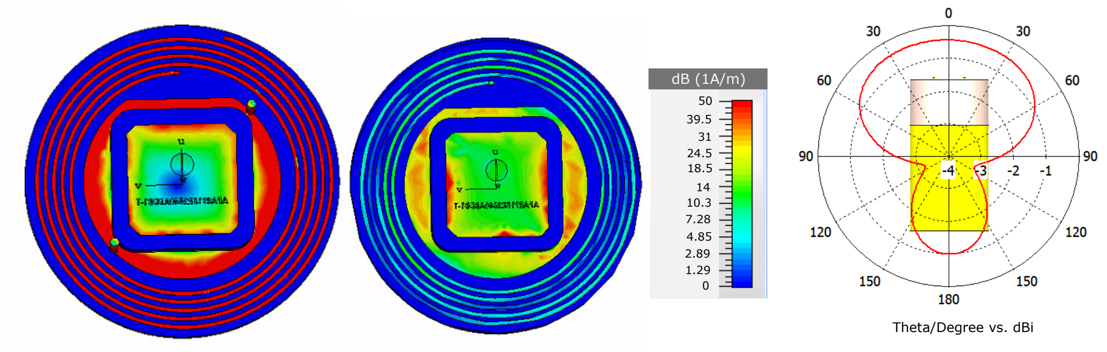

(a) (b) (c)

Figure 4.9: (a) Simulated frequency domain surface current at 923 MHz when the HF loop was excited. (b) Simulated frequency domain surface current at 923 MHz when the ceramic antenna was excited. (c) Simulated ceramic antenna gain at 923 MHz.

in the HF loop and around the edges of the UHF ceramic antenna as well as in the ground plane of UHF antenna due to the proximity of the HF and UHF antennas which is apparent in Fig. 4.9 (a). When the ceramic antenna is excited at 923 MHz, the signal is mostly confined at the edges of the antenna and the ground plane, and very less current flows in the HF coil which is shown in Fig. 4.9 (b).

The measured -10 dB bandwidth of the UHF ceramic antenna ranged from 921.8 to 923.8 MHz. Measured scattering parameters from VNA showed that the HF loop antenna has a harmonic at 923 MHz. To suppress it, a 220 pF capacitor was connected between the feed and the ground to act as a low pass filter (LPF).

4.8 Design 1: BCI antenna PCB measurements

4.8.1 Port-to-port coupling

The HF BCI antenna was connected to port 1 of VNA and UHF ceramic BCI antenna was connected to port 2 of VNA to measure S-parameters. Fig. 4.10 shows the measured results. Ideally, port-to-port coupling should be minimal.

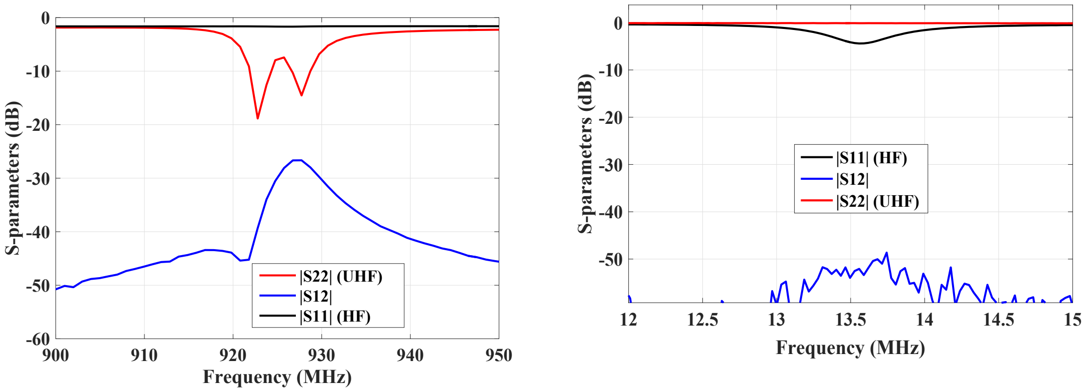

(a)

(b)

Figure 4.10: Measured S-parameters of HF and UHF BCI antennas inside the teflon cap connected to Ti tube.

The measured worst-case port-to-port mutual coupling between BCI HF and BCI UHF antennas was -27 dB ($|S_{21}|$ dB) in the 902 - 928 MHz band and -49 dB at 13.56 MHz when LPF was connected to the loop. Measured port-to-port transmission coefficient was -8 dB in the UHF band when LPF was not connected. Due to LPF, the port-to-port coupling was reduced by 19 dB. Hence, LPF is an essential block in this antenna arrangement.

4.8.2 HF antenna testing in air

The BCI HF loop antenna was tested in free-space using WiBotic's HF loop as a transmitter antenna. An experimental setup is shown in Fig. 4.11. The distance between the HF loop and WiBotic's coil was increased from 7 cm to 15 cm. The measured transmission coefficient at a separation distance of 7 cm was -2.21 dB and -10.8 dB at 15 cm.

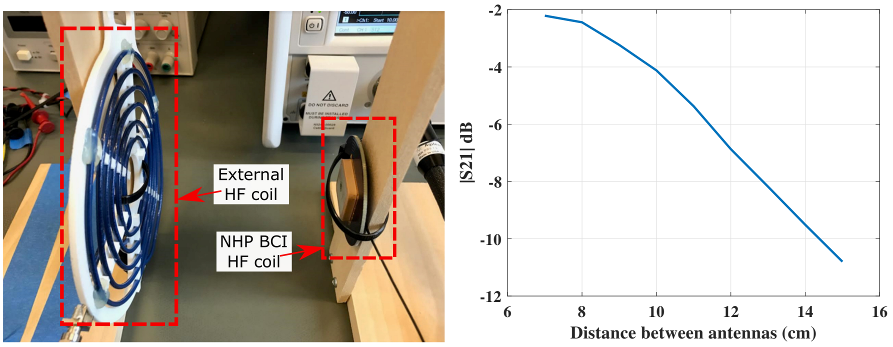

(a) (b)

Figure 4.11: (a) Picture showing the experimental setup. (b) Transmission coefficient $|S_{21}|$ dB from 7 cm to 15 cm separation gap.

4.9 Cage experimental setup for backscatter communication

A 7 kg saline tissue solution was used as a phantom in place of a male pigtail macaque, which weighs 7 kg on average. The phantom is made up of 7 liters of saline solution with 0.91 gram NaCl per liter of distilled water [1] filled in a plastic container with dimensions of 41.8 cm × 27.8 cm × 16.5 cm (length × width × height). The BCI assembly was placed on top of the saline filled plastic container. The BCI antenna was connected to port 1 of a Keysight FieldFox VNA with a coaxial cable, and the cage antenna was connected to port 2 of the VNA with another coaxial cable. These cables were carefully dressed along the metal surfaces of the cage to ensure that the cable placement did not significantly influence the measurement.

BCI antenna performance was measured at multiple locations within the cage. As shown in Fig. 4.2 (a), the cage volume was divided into 3 horizontal measurement planes, labeled 1-3 from bottom to top, with a vertical spacing of 20.3 cm between measurement planes . An RF-transparent Styrofoam block (dielectric constant ≈ 1) was utilized to raise the tissue phantom's height to measurement planes 2 and 3. These measurement planes were, in turn, subdivided into 7.6 cm × 7.6 cm square grids (Fig. 4.12). All measurement positions were conducted in the center of these squares. The edges of each grid line were labeled from 1 to 7 and from A to G for the X-axis and the Y-axis respectively. Thus, the center of the cage corresponds to location D4. Measurement planes 2 and 3 contain 49 measurement locations. However, for measurement planes 1, the experiments were performed from rows A to G along the Y-axis but only from columns 1 to 4 along the X-axis, due to the placement of the metal seat, giving a total of 28 measurement locations.

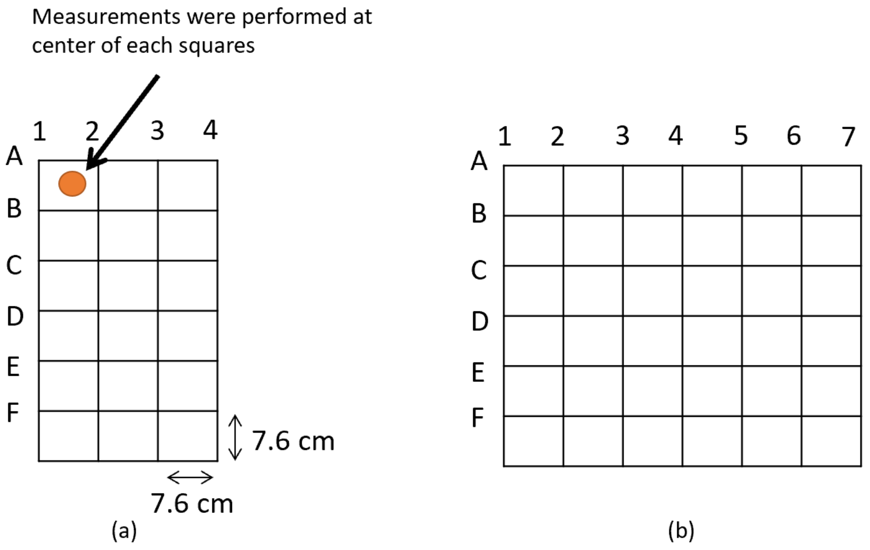

Figure 4.12: (a) Measurement grid for plane 1. (b) Measurement grid for planes 2 and 3. Measurements were performed at the center of each grid.

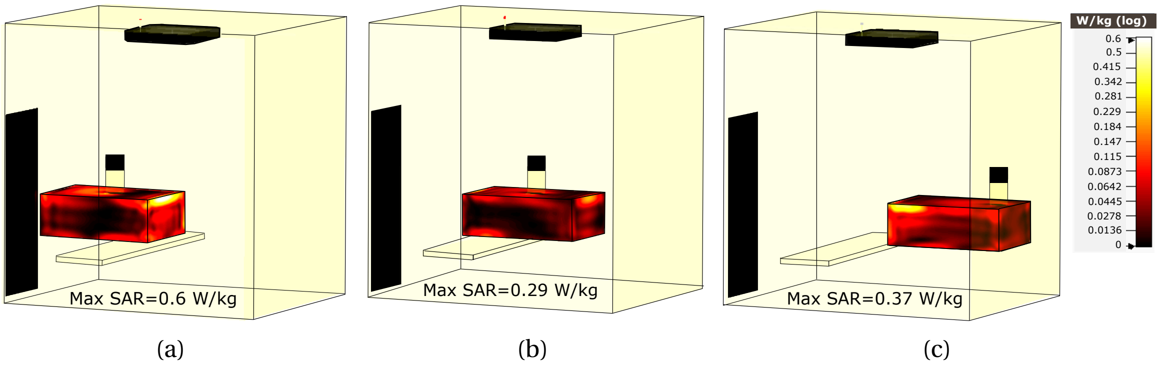

Figure 4.13: Simulated SAR for the input power of 1 W (30 dBm) transmitted from the cage antenna. The peak SAR value obtained from all three positions is well below the regulatory limit of 1.6 W/kg for human exposure.

4.9.1 Design 1: SAR simulation inside the NHP cage

The time-domain solver module built into CST was employed to estimate the SAR on the tissue phantom. The peak SAR for the saline phantom was simulated for locations D1, D4 and D7 at Level 2 for an input power of 1 W (30 dBm). The dielectric properties of saline were calculated using the Debye first order model at room temperature [87]. To our knowledge there is no established SAR measurement procedure for NHPs nor established limits. The SAR in a saline solution model can be considered as worst case due to the higher conductivity of the saline vs. NHP tissue [90]. As shown in Fig. 4.13, the maximum calculated value that was obtained is 0.6 W/kg averaged over 1 gram of saline mass for the input peak power of 30 dBm. This is well below the regulatory limit of 1.6 W/kg for human exposure that is imposed by the FCC in the United States. We expect the actual SAR to be ≈20 dB smaller than the simulated values, because for the actual experiments a 10 dBm peak transmit power was utilized.

4.10 Design 1: cage UHF monostatic uplink experimental results

We performed a two-port calibration of the coaxial cables and VNA prior to measurement. To further mitigate cable effects, we routed the cables away from the direct path between the antennas and perpendicular to the antenna plane as much as possible, routing the cable along the metal cage walls.

4.10.1 Estimation of usable bandwidth and insertion loss

The BCI antenna performance was characterized in terms of its 3 dB bandwidth (MHz), insertion loss (dB), and orientation sensitivity. The insertion loss is the absolution of trans-

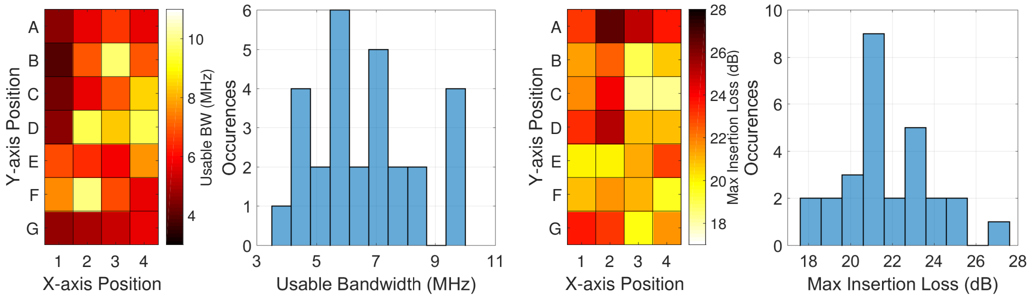

(a) (b) (c) (d)

Figure 4.14: Experimental results using ceramic antenna, at measurement plane 1 showing (a) Heatmap and (b) Histogram of usable bandwidth. (c) Heatmap and (d) Histogram of maximum insertion loss. In all heatmap images, darker colors indicate worse performance.

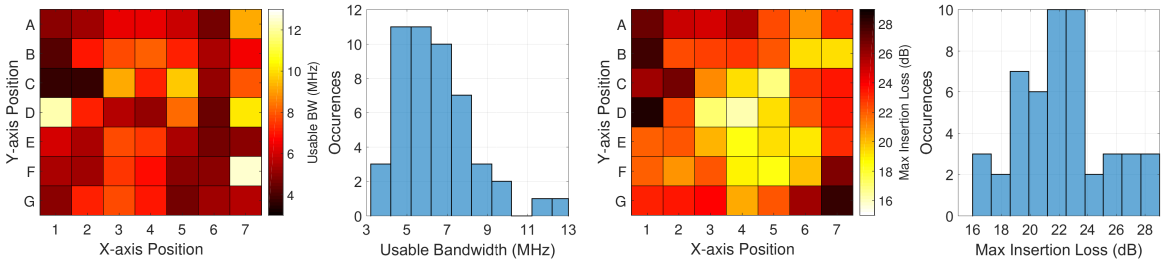

(a) (b) (c) (d)

Figure 4.15: Experimental results using ceramic antenna, at measurement plane 2 showing (a) Heatmap and (b) Histogram of usable bandwidth. (c) Heatmap and (d) Histogram of maximum insertion loss. In all heatmap images, darker colors indicate worse performance.

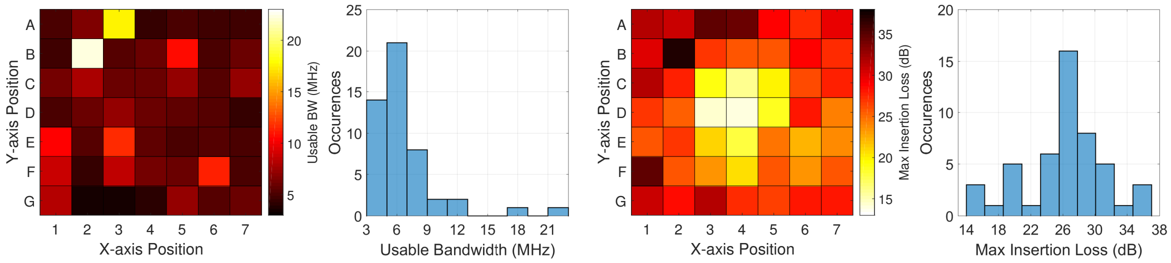

(a) (b) (c) (d)

Figure 4.16: Experimental results using ceramic antenna, at measurement plane 3 showing (a) Heatmap and (b) Histogram of usable bandwidth. (c) Heatmap and (d) Histogram of maximum insertion loss. In all heatmap images, darker colors indicate worse performance.

mission coefficient (S_{21} dB). The bandwidth and the insertion loss were measured at each different measurement location for all three measurement planes. Figs. 4.14 - 4.16 shows the aggregated results where darker colors indicate smaller bandwidths or higher insertion loss. The mean 3 dB bandwidth (which is considered to be the "Usable" bandwidth) was found to be 6.56 MHz, 6.50 MHz, and 6.70 MHz for measurement planes 1, 2, and 3, respectively. The maximum insertion loss inside the 3 dB bandwidth was measured at 27.6 dB, 28.7 dB, and 37 dB for measurement planes 1, 2, and 3, respectively. Due to the cavity effects, the 3 dB bandwidth across all 126 measurement locations varied from 3.4 MHz to 22 MHz, and the best and worst case insertion loss were 14 dB and 37 dB, respectively.

Table 4.2: Summary of measured results inside the cage using ceramic antenna as BCI antenna.

Parameter	**Value**
Mean bandwidth (measurement plane 1) in MHz	6.5
Worst case insertion loss (measurement plane 1) in dB	-27.6
Mean bandwidth (measurement plane 2) in MHz	6.5
Worst case insertion loss (measurement plane 2) in dB	-28.7
Mean bandwidth (measurement plane 3) in MHz	6.7
Worst case insertion loss (measurement plane 3) in dB	-37

4.10.2 Verification of link budget

To evaluate end-to-end performance of the system throughout the entire volume of the cage, we conducted PER measurements by collecting a total of 10^6 packets at 25 measurement locations inside the cage. Fig. 4.17 shows collected data overlaid on the measured insertion loss heatmap at three measurement planes. It can be concluded that packets were received without packet dropout at all locations, except at A1 and G1 locations of plane 3 where packet dropouts were observed due to the presence of deep null. At locations G1 and A1 of plane 3, insertion loss was greater than 30 dB. The link budget shown in Section 4.3.1, suggests that telemetry packets may be lost at the locations inside the cage where the insertion loss is higher than 30 dB. We found a similar trend in PER measurements.

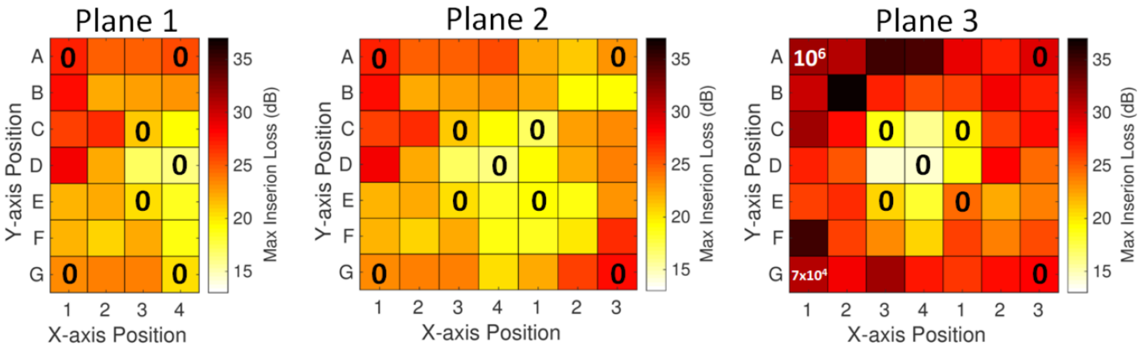

Figure 4.17: PER measurements at three measurement planes. Results are in agreement with the link budget.

4.10.3 Measured reflection coefficient of BCI ceramic antenna

As shown in Fig. 4.18, the reflection coefficient $|S_{11}|$ (dB) of the BCI antenna is better than -10 dB across the 921.5 – 924 MHz band (2.5 MHz BW) for two out of nine positions of measurement plane 2, while in seven out of the nine test locations the -10 dB bandwidth was around 921.5 to 928 MHz (6.5 MHz BW). This suggests that the matching of BCI antenna does not change drastically with the change in antenna position inside the cage.

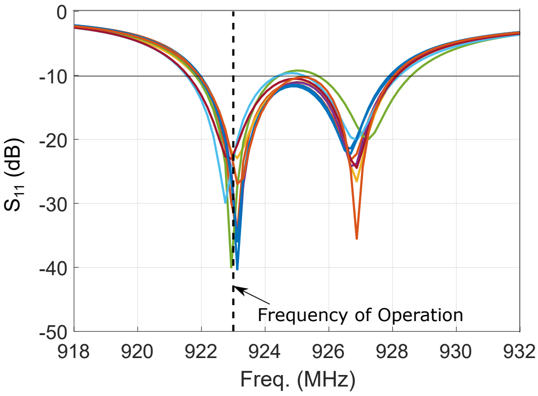

Figure 4.18: Measured S_{11} (dB) of the BCI antenna at nine different locations of measurement plane 2. In 2 of the 9 locations, the -10 dB bandwidth was ≈ 921.5 -924 MHz, and for the remaining 7 locations, the -10 dB bandwidth was ≈ 921.5 -928 MHz.

4.10.4 Orientation sensitivity analysis

The BCI antenna was characterized for the orientation sensitivity relative to the cage antenna. The saline phantom and the BCI assembly were placed in the center of measurement plane 2 (location D4), and rotated along their vertical Z-axis with a step of 45^{o} ranging from 0^{o} - 330^{o} and along an elevation angle with a step of 30^{o}, ranging from 0^{o} - 90^{o}. The results are depicted in Fig. 4.19, showing a maximum orientation impairment of 3 dB along the vertical Z-axis and a maximum orientation impairment of 7 dB along the elevation angle. Hence, we can say that the presence of NHP is not the only problem inside the cage, if the antenna orientation changes the insertion loss can increase which can make the system more sensitive.

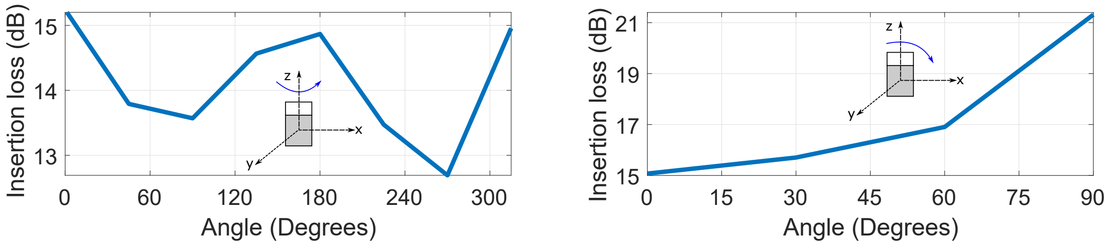

(a)

(b)

Figure 4.19: Measured insertion loss at 923 MHz. (a) Rotation along z-axis. (b) Elevation angle from z-axis to x-axis

4.11 Understanding measured results inside the cage

Experimental results measured at three planes, showed that the insertion loss was generally higher where the 3 dB bandwidth was higher and lower at the locations where 3 dB bandwidth was small. For example, Fig. 4.15 shows that at position D4, the insertion loss was 14 dB and the 3 dB bandwidth was 6 dB. While at position B2 the insertion loss was 37 dB and the 3 dB bandwidth was 22 MHz. Similar relationship between insertion loss and bandwidth can be noticed in mode-stirred reverberant chambers (RC).

RCs are large, cavity resonator with high quality factor and are commonly used for electromagnetic compatibility (EMC) testings as well as for measuring antenna efficiency. Electric and magnetic field distributions inside RC are highly inhomogeneous due to the presence of dense multipath. To generate uniform field distribution inside the chamber, mechanical mode-stirrers are used, such as metallic rotating plates (as shown in Fig. 4.20) [122].

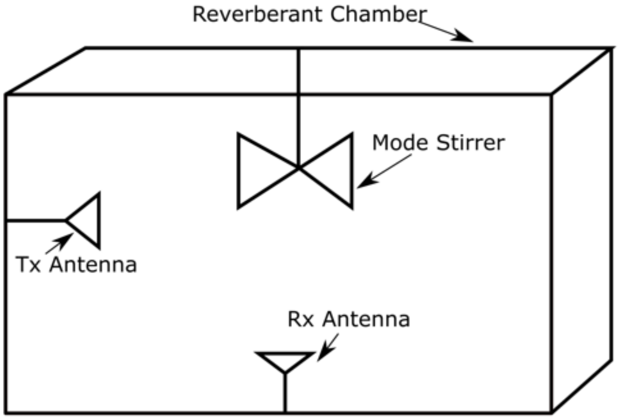

Figure 4.20: Block diagram of reverberant chamber.

The relationship between transmission coefficient and the bandwidth inside RC can be obtained from the quality factor (Q). The quality factor can be written as

$$Q = \omega \frac{U}{P_d} = \frac{f}{\Delta f} \tag{4.2}$$

where ω is the angular frequency, U is the stored energy inside the cavity, P_d is the dissipated power in cavity, f is the operating frequency and Δf is the bandwidth.

Quality factor for a reverberant chamber (RC) can be defined using following equation [123]

$$Q = \frac{16\pi^2 V}{\lambda^3} \Big(\frac{< P_r >}{P_t} \Big) \tag{4.3}$$

where $< P_r >$ is average received power for all stirred angles, and P_t is the transmitted power. The Q inside the cavity can be obtained statistically based on experiments where transmitter antenna is connected to one port of VNA and the receiver antenna connected to the other port of VNA [124]. For VNA measurements Eq. 4.3 can be modified to [125]

$$Q = \frac{16\pi^2 V}{\lambda^3} \frac{< |S_{21}|^2 >}{< (1-|S_{11}|^2) >< (1-|S_{22}|^2) > \eta_1\eta_2} \tag{4.4}$$

where <·> represents the average over different stirrer positions, η_1 is the radiation efficiency of the antenna connected to port 1, η_2 is the radiation efficiency of the antenna connected to port 2. For well-matched antennas Eq. 4.4 can be modified to

$$Q = \frac{16\pi^2 V}{\lambda^3} \frac{< |S_{21}|^2 >}{\eta_1\eta_2} \tag{4.5}$$

Eq. 4.5 suggests that the quality factor inside the reverberant chamber is proportional to the transmission coefficient (S_{21}). This equation suggests that, at the location with deep nulls where S_{21} is small, the Q will be low and the Q will be high at the locations of hot spots where S_{21} is maximum. As Q is inversely proportional to the bandwidth, it can be concluded that the bandwidth will be higher at location of deep nulls and smaller at hot spots. We found similar relationships between bandwidth and S_{21} inside the cage for all three measurement planes. Hence, we assume that the movement of NHP acts as a mode-stirrer inside the cage and can be compared with RCs.

4.11.1 Justification through simulations

Simulations were performed to check E-field distribution at various locations of saline proxy and BCI antenna inside the cage. As shown in Fig. 4.21, location (b) has a hot spot (peak E-field) in the area surrounding BCI assembly, and locations (a) & (c) have low E-field concentration in the area surrounding BCI assembly. Transmission coefficient was highest at location (b) due to high E-field concentration and lowest at location (c). The simulated

3-dB bandwidth was 15 MHz, 13 MHz, 19 MHz, 18 MHz at locations (a), (b), (c), and (d), respectively. Simulations suggest that if BCI assembly is in the hot spot then the transmission coefficient will be higher and the 3-dB bandwidth will be lower.

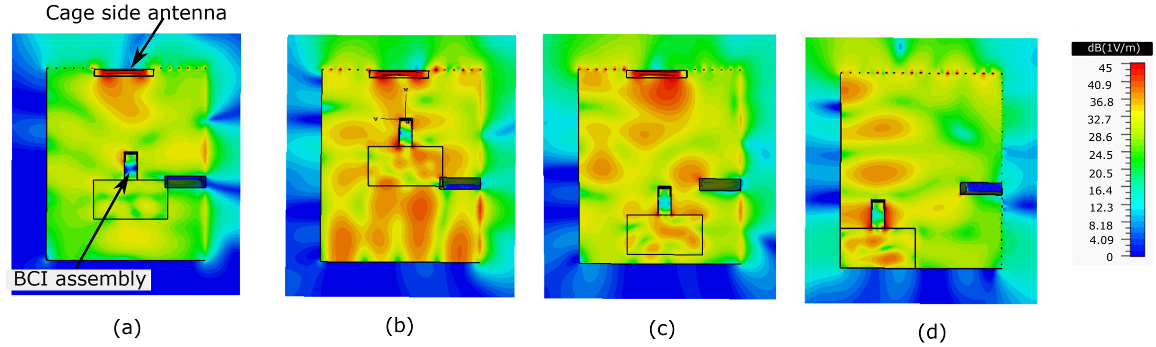

Figure 4.21: Simulated time domain E-field along x-axis inside the cage at locations (a), (b), (c), and (d).

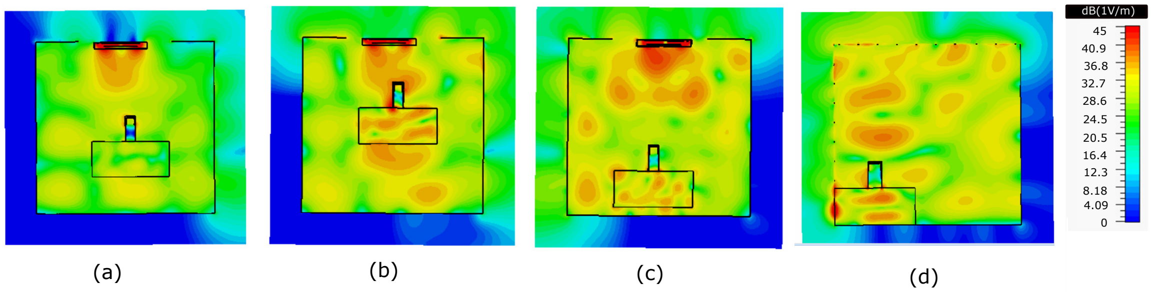

Figure 4.22: Simulated time domain E-field along y-axis inside the cage at locations (a), (b), (c), and (d).

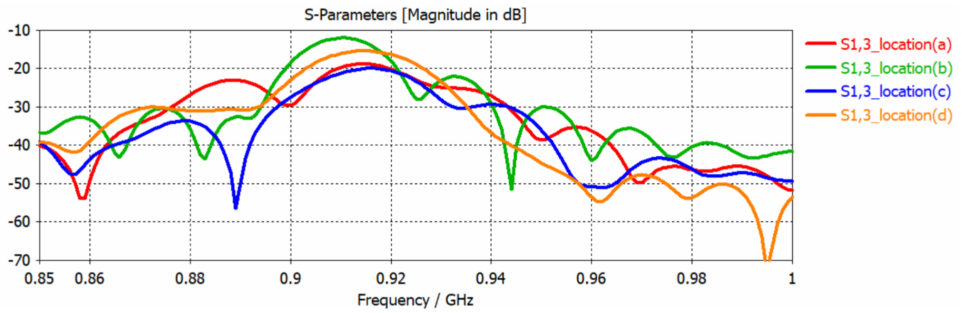

Figure 4.23: Simulated S-parameters at different at locations (a), (b), (c), and (d) .

4.12 Design 1: *in-vivo* recordings using ceramic BCI antenna

In-vivo recordings were performed on an anesthetized pigtail macaque (*Macaca nemestrina*) to validate the performance of wireless backscatter uplinks. The experiments were conducted at the Washington National Primate Research Center, Seattle, Washington, USA, with the support of the UW Department of Physiology and Biophysics, and all experimental procedures were approved by the UW Institutional Animal Care and Use Committee. The BCI assembly containing ceramic antenna was connected via a 17 cm of shielded single-ended cabling to a chronically-implanted 96-channel Utah Array (Blackrock Microsystems), previously implanted in the primary motor cortex (M1). The monkey rested on a plastic surgical cart, and the BCI assembly was placed horizontally at the edge of the cart so that the BCI antenna had a clear line-of-sight to an external system patch antenna placed 30 cm away (Fig. 4.24).

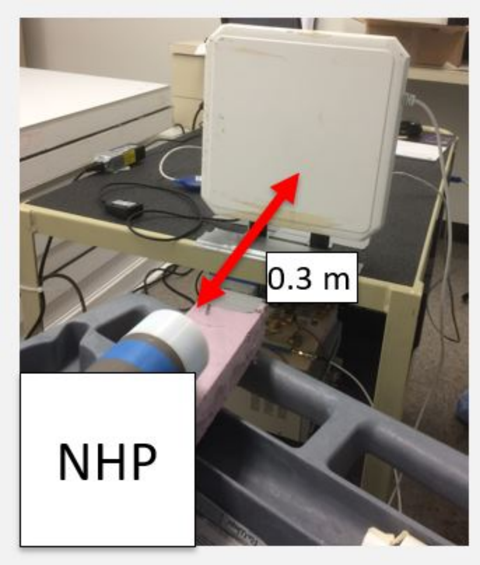

Figure 4.24: Photo of *in-vivo* experimental setup *(image courtesy of James Rosenthal).*

For this experiment, the BCI assembly was configured to sample eight channels at 5 kHz with a 1 Hz - 2 kHz band- pass filter as well as a 1.6 Hz DSP high-pass filter. Sampled data was able to uplink towards the external system with a rate of 6.25 Mbps. The received data, which was plotted in MATLAB, is shown in Fig. 4.25.

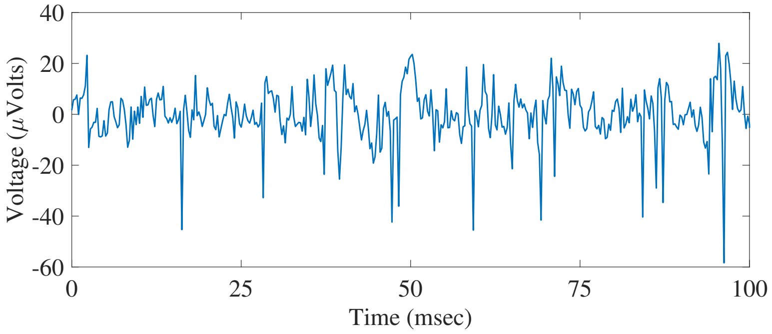

Figure 4.25: Example of wirelessly uplinked *in-vivo* neural spike recordings from the primary motor cortex of a pigtail macaque.

4.13 Design 2: BCI antenna system using wide-band μSP antenna for communication

In previous work, the maximum wireless uplink rate was limited to 6.25 Mbps due to a -10 dB antenna bandwidth of 1 MHz in free space. The BCI antenna presented in this section is designed to have a wider bandwidth of 12.5 MHz to support higher data rates. The antenna element used in this work was the Linx Technologies (Merlin, OR) Ant-916-μSP antenna whose dimensions are 12.7 mm x 9.2 mm x 2.8 mm (width x length x height) where μSP stands for embedded SP Series Splatch. These commercial antennas are great for remote controls and other compact devices [126]. The layout of the μSP antenna is shown in Fig. 4.26.

The μSP antenna was connected to the top layer of the PCB with three connection pads; one pad was connected to a 50 Ω microstrip feed line, and the other two were connected to the ground plane. The bottom layer of the antenna PCB consists of a ground plane, UHF matching network, and UMC connectors. The matching circuit connected to the μSP antenna is shown in Fig. 4.27. The antenna PCB is a two-layer board whose outer diameter is 55 mm outer. It was designed on a 1.6 mm-thick FR–4 substrate with 30 μm thick copper. The μSP antenna was chosen for communication due to its low cost, compact form factor, and wide bandwidth.

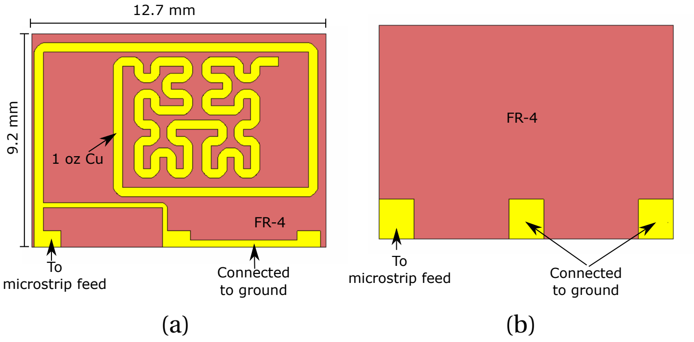

(a) (b)

Figure 4.26: Layout of μSP antenna. (a) Top View. (b) Bottom View.

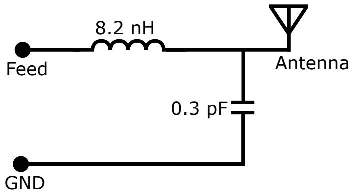

Figure 4.27: Matching network connected to μSP antenna.

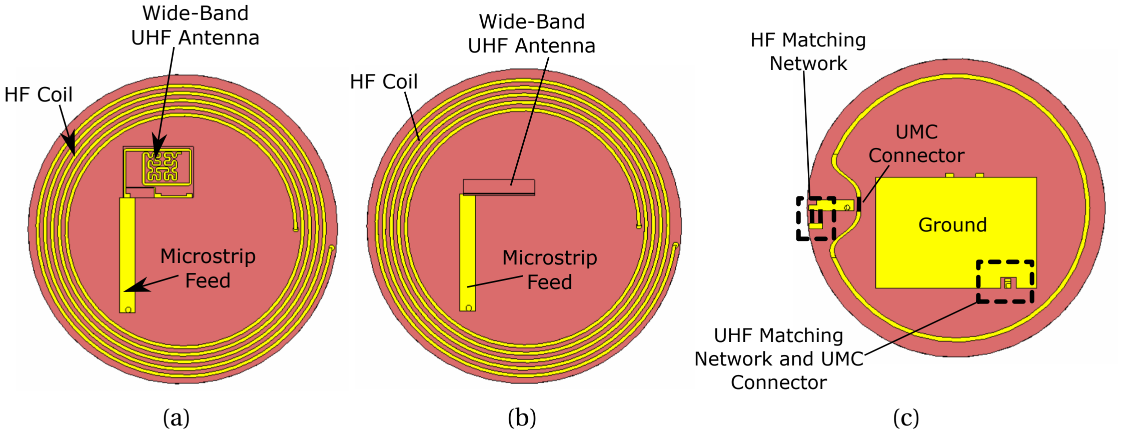

(a) (b) (c)

Figure 4.28: (a) μSP antenna parallel to PCB (b) μSP antenna perpendicular to PCB. (c) Bottom view.

4.14 Design 2: simulated coupling between BCI HF and UHF antennas

In this section, two antenna configurations were considered for simulations: μSP antenna parallel to the plane of PCB as shown in Fig. 4.28 (a), and μSP antenna perpendicular to the plane of PCB as shown in Fig. 4.28 (b). Fig. 4.29 presents a time-domain simulation of surface current for both configurations of μSP antenna in PCB. The surface current induced in HF coil from μSP antenna is much higher when the antenna was parallel to PCB, as compared to the case when the antenna was perpendicular to PCB. Higher coupling is observed between HF and μSP antennas in the case of parallel μSP antenna, as the E-field is parallel to the plane of the PCB.

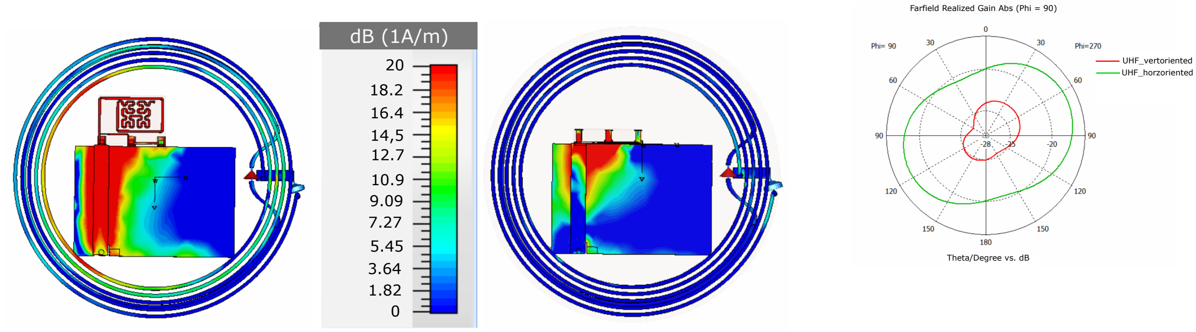

(a) (b) (c)

Figure 4.29: (a) Simulated frequency domain surface current at 923 MHz when μSP antenna was parallel to PCB. (b) Simulated frequency domain surface current at 923 MHz when μSP antenna was perpendicular to PCB. (c) Simulated gain pattern at 923 MHz for μSP antenna at both locations.

The μSP antenna has a meander shape. The advantage of meandering the antenna is that the overall antenna area can be reduced with the same electrical length. The antenna gain is proportional to the area and meander antennas have smaller area. As a result the gain of meander antenna is small. The simulated peak gain of perpendicular μSP antenna was -15 dB and that of parallel μSP antenna was -22 dB. The simulated -10 dB bandwidth of μSP antenna for both configurations is from 907 MHz to 922 MHz, which is much higher than the bandwidth of ceramic antenna proposed in previous sections. The BCI antenna PCB which was used for experiments contains μSP antenna perpendicular to PCB to achieve better gain and less coupling with the HF coil.

4.15 Design 2: Experiments inside NHP cage using μSP antenna

In this experiment, a commercially available Laird Technologies S9028PCR antenna was connected inside the top wall of the cage similar to the setup mentioned in section 4.4, and a BCI assembly containing μSP antenna was placed inside Teflon cap of Ti enclosure. The BCI assembly was placed on a saline solution tissue proxy container and the container was moved along 3 different measurement planes.

4.15.1 Measured reflection coefficient of μSP antenna

Fig. 4.30 shows a reflection coefficient of μSP antenna inside the cage measured at eight different location points of measurement plane 2. It can be concluded from the results that $|S_{11}|$ dB do not vary much inside the cage. The overall measured bandwidth of a μSP antenna is from 910 MHz to 923 MH i.e. 13 MHz.

4.15.2 Estimation of usable bandwidth and insertion loss

Similar to the section 4.10, the BCI ceramic antenna performance was characterized in terms of its 3 dB bandwidth (MHz), insertion loss (dB), and orientation sensitivity. The bandwidth and the insertion loss were measured at three different measurement planes.

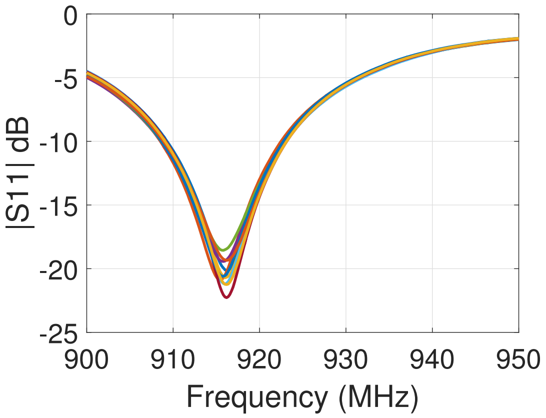

Figure 4.30: (a) Measured $|S_{11}|$ (dB) of the μSP antenna inside the cage at eight different locations of measurement plane 2. The -10 dB bandwidth is ≈ 910 MHz-923 MHz at all 8 locations.

Figs. 4.31-4.33 depict the aggregated results where darker colors indicate smaller bandwidth or higher insertion loss. The mean 3 dB bandwidth (which is considered to be the "usable" bandwidth) found to be 23.8 MHz, 22.9 MHz, and 23.9 MHz for measurement planes 1, 2, and 3, respectively. The mean insertion loss inside the 3 dB bandwidth was measured as 33.9 dB, 33.3 dB, and 35 dB for measurement planes 1, 2, and 3, respectively. It is important to note that, due to the cavity effects, the 3 dB bandwidth across all 126 measurement locations varied from 11 MHz to 56 MHz, and the best and worst case insertion loss were 21 dB and 42 dB, respectively.

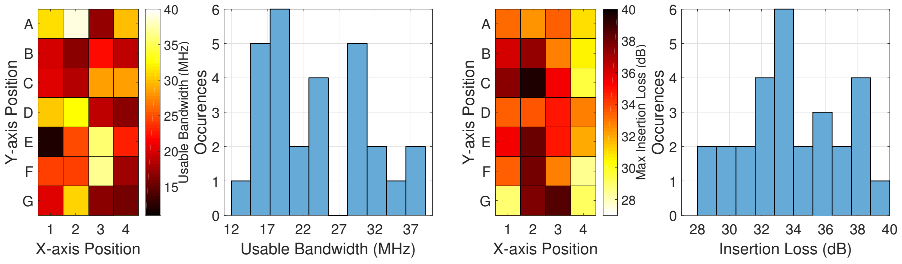

(a) (b) (c) (d)

Figure 4.31: Experimental results using μSP antenna, at measurement plane 1 showing (a) Heatmap and (b) Histogram of usable bandwidth. (c) Heatmap and (d) Histogram of maximum insertion loss. In all heatmap images, darker colors indicate worse performance.

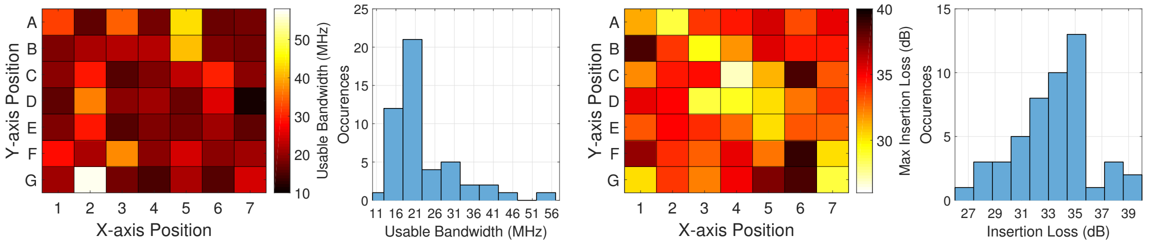

(a) (b) (c) (d)

Figure 4.32: Experimental results using μSP antenna, at measurement plane 2 showing (a) Heatmap and (b) Histogram of usable bandwidth. (c) Heatmap and (d) Histogram of maximum insertion loss. In all heatmap images, darker colors indicate worse performance.

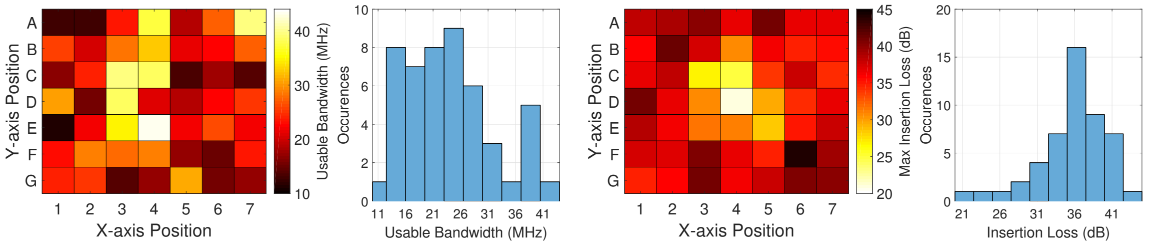

(a) (b) (c) (d)

Figure 4.33: Experimental results using μSP antenna, at measurement plane 3 showing (a) Heatmap and (b) Histogram of usable bandwidth. (c) Heatmap and (d) Histogram of maximum insertion loss. In all heatmap images, darker colors indicate worse performance.

Table 4.3: Summary of measured results using μSP antenna.

Parameter	**Value**
Mean bandwidth (measurement plane 1) in MHz	23.8
Worst case insertion loss (measurement plane 2) in dB	-40
Mean bandwidth (measurement plane 1) in MHz	22.9
Worst case insertion loss (measurement plane 2) in dB	-40
Mean bandwidth (measurement plane 3) in MHz	23.9
Worst case insertion loss (measurement plane 3) in dB	-42

4.15.3 Orientation sensitivity analysis

For the orientation sensitivity analysis, saline phantom and the BCI assembly were placed in the center of measurement plane 2 (location D4), and rotated along their vertical Z-axis with a step of 45^{o} ranging from 0^{o}- 330^{o} and along an elevation angle with a step of 30^{o}, ranging from 0^{o}- 90^{o}. The results are depicted in Fig. 4.34, showing a maximum orientation impairment of 6 dB along the vertical Z-axis and a maximum orientation impairment of 11 dB along the elevation angle.

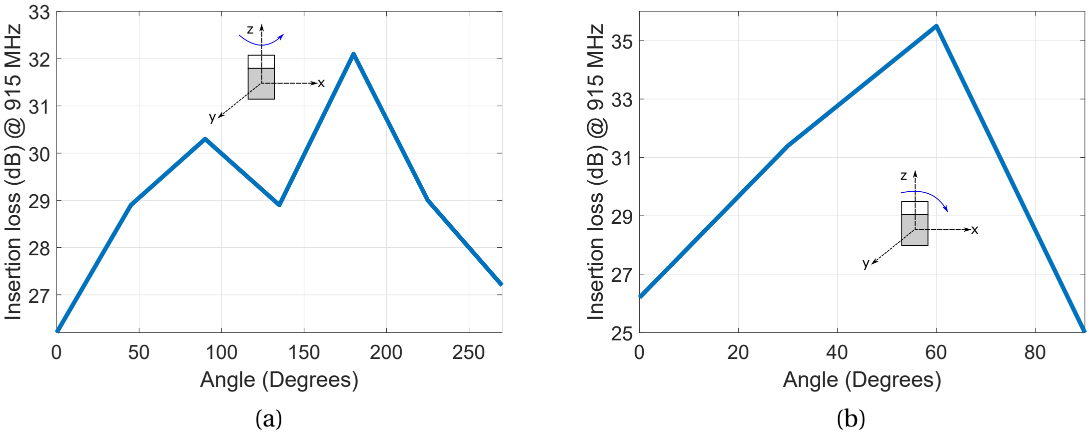

Figure 4.34: Measured insertion loss at 915 MHz using μSP antenna. (a) Rotation along z-axis. (b) Elevation angle from z-axis to x-axis

4.16 Design 2: *in-vivo* recordings using μSP antenna

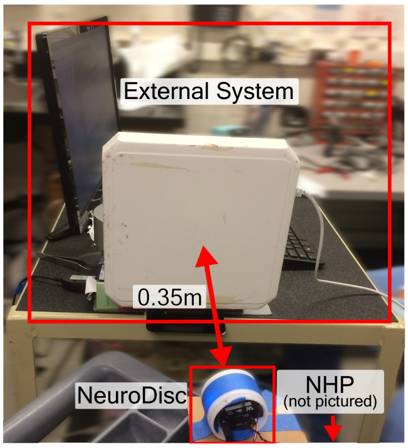

Figure 4.35: Photo of the *in-vivo* experimental setup *(image courtesy of James Rosenthal).*

The BCI assembly was placed on a plastic surgical table at a distance of 35 cm from the external patch antenna. The experimental setup is shown in Fig. 4.35. The neurochip used in the experiment has 16 recording channels which were connected to the monkey's implanted electrode via a 17 cm shielded cable. Recordings from all 16 channels were pre-configured with a sampling rate of 20 kSps with 16-bit resolution per channel. To remove low-frequency offsets from the data, the biosignal front-end was configured with a 1 Hz – 7.5 kHz band-pass filter and a 1.6 Hz digital high-pass filter.

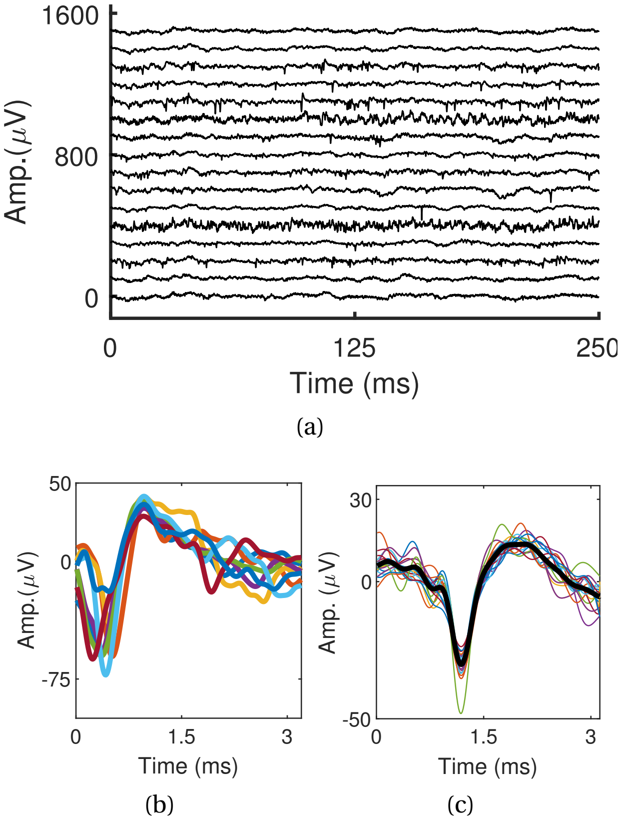

Figure 4.36: *In-vivo* data was uplinked to the External System. (a) Time series plot of all 16 channels of measured neural data. Offline spike sorting was then performed on the data based on [7] (b) Plot of five mean spike waveforms identified in one channel of the data. (b) Plot of the spikes identified identified within one cluster overlaid with the mean waveform.

The recorded neural signals were uplinked to the external system with a data rate of 25 Mbps, which were then decoded and plotted offline using Matlab. A time-series plot of the recording channels is shown in Fig. 4.36(a). The data shows low-frequency fluctuations corresponding to local field potentials (LFPs) as well as higher-frequency neural spikes. Some channels,such as the fifth channel from the bottom in Fig. 4.36(a), exhibited higher noise that could be attributed to neural cell loss or glial scarring due to the chronically-implanted micro-electrode array. Spike sorting was applied to the data set, using methods presented in [7], to validate that the neural recordings captured biologically relevant signals. Several neural spike families were identified in the data (Fig. 4.36(b) and (c)). Summary of implant antenna and head-stage antennas, designed in this work are shown in Table 4.4.

Table 4.4: Summary of BCI antennas designed in this work

BCI UHF antenna	**Distance between external and BCI antennas (cm)**	**BCI antenna -10 dB BW in free space (MHz)**	**BCI antenna dimensions (cm × cm × cm)**	**BCI antenna gain (dBi)**	**Data rate achieved (Mbps)**
Ceramic Antenna	30	1	2.5 × 2.5 × 2.5	-0.4	6.25
μSP Antenna	35	12.5	1.27 × 0.92 × 0.28	-13.6	25
Implant Annular Ring Antenna	1.5	18	Diam. 1.46 × thickness 0.3	-25	5

4.17 BCI antenna behavior between air and the cavity environment

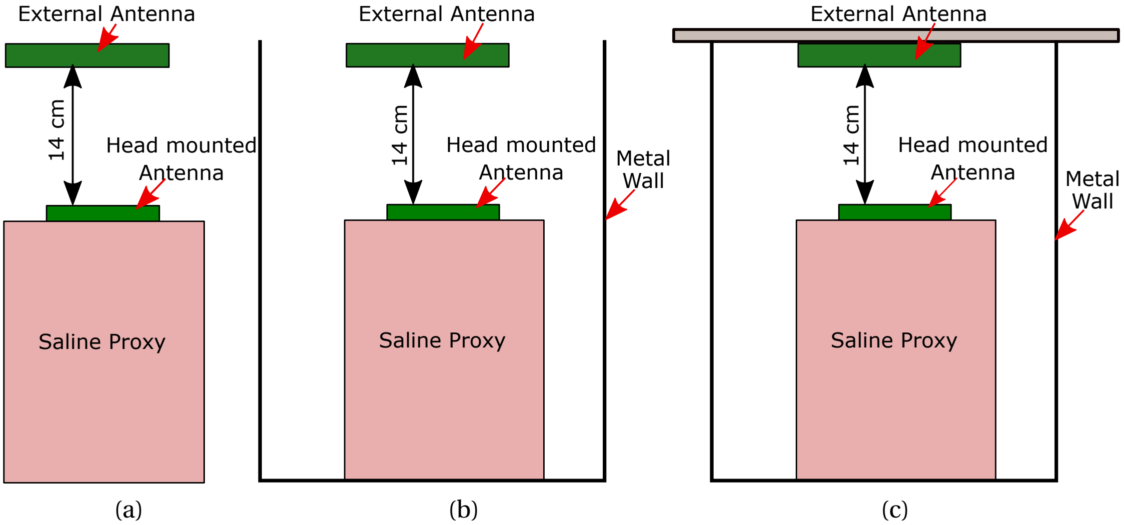

Figure 4.37: Block diagram of experimental setup: (a) antennas in free space, (b) antennas in open cavity from the top, and (c) antennas inside closed cavity.

This section presents the performance of BCI antenna in three different environments: (a) free space, (b) open cavity from the top, and (c) closed cavity. In the experiments, patch antenna was used as an external antenna whose design description is mentioned in Section.

4.4, and ceramic antenna was used as a head-stage BCI antenna. A detailed description of ceramic BCI antenna is mentioned in Section. 4.6.

The BCI antenna was inserted into a head-stage canister placed on the top of a plastic container containing saline solution serving as a primate proxy. Experiments were performed inside a cardboard box whose dimensions were comparable to the Washington National Primate Research Center's NHP cage mentioned in Section. 4.2. To emulate an open cavity, we attached aluminum foil on the side and bottom walls of the cardboard box leaving the top wall open as shown in Fig. 4.37 (b). For a closed cavity, aluminum foil was attached to all six walls as shown in Fig. 4.37 (c). At UHF band, cardboard is transparent to EM waves. Hence, experiments in the box without attaching aluminum foil to all walls emulate free space.

The external antenna was placed inside the top wall of the cardboard box, and the BCI antenna was placed 14 cm below the external antenna on the top of saline container. Both antennas were connected to a VNA. The primate proxy container was placed on a grid of 40 location points inside the cardboard box. For each location, two data sets were collected : the transmission coefficient between the antennas ($|S_{21}|$ dB) and the 3 dB usable bandwidth in 915 MHz ISM band. Identical tests were performed in free space, closed, and open cavities.

Measurement results showed that the mean bandwidth was 12.6 MHz, 12.5 MHz, and 14.5 MHz in free space, open cavity, and closed cavity, respectively. Measured mean insertion loss was 43.3 dB, 37.7 dB, 26.1 dB in free space, open cavity, and closed cavity, respectively.

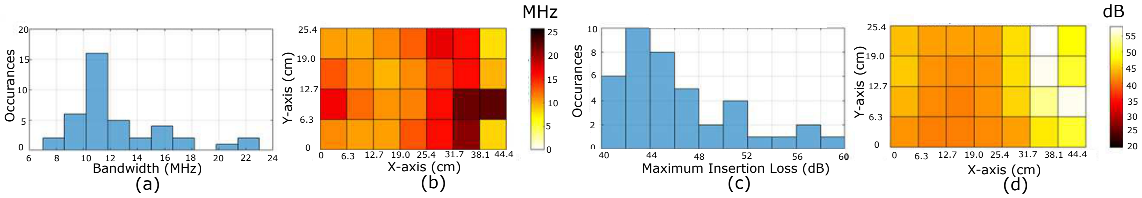

Figure 4.38: Experimental results in free space showing (a) Heatmap and (b) Histogram of usable bandwidth. (c) Heatmap and (d) Histogram of maximum insertion loss. In all heatmap images, lighter colors indicate worst performance.

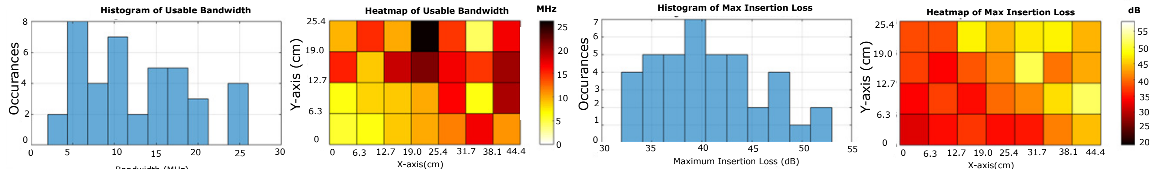

Figure 4.39: Experimental results in open cavity showing (a) Heatmap and (b) Histogram of usable bandwidth. (c) Heatmap and (d) Histogram of maximum insertion loss. In all heatmap images, lighter colors indicate worst performance.

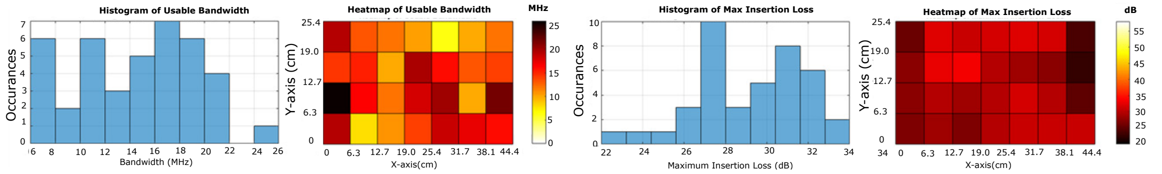

Figure 4.40: Experimental results in closed cavity showing (a) Heatmap and (b) Histogram of usable bandwidth. (c) Heatmap and (d) Histogram of maximum insertion loss. In all heatmap images, lighter colors indicate worst performance.

Insertion loss inside the cage depends on the location of BCI antenna. If the BCI antenna is in the hot spot then the insertion loss will be lower or if the BCI antenna is in the deep null caused by the multipath then the insertion loss will be higher.

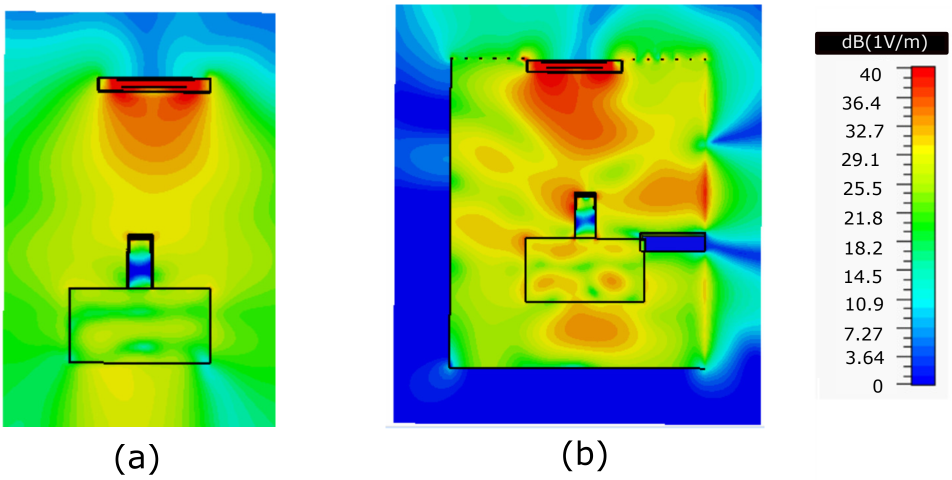

Figure 4.41: Time domain E-field plots at 915 MHz. (a) In free space. (b) In cage.

As shown in Fig. 4.41, E-field was higher in the area surrounded by BCI assembly inside the cage as compared to free space. Transmission coefficient was higher inside the cage as compared to free space environment (Fig. 4.42) with smaller 3 dB bandwidth.

This experiment suggests that the antenna system designed for a cavity environment can

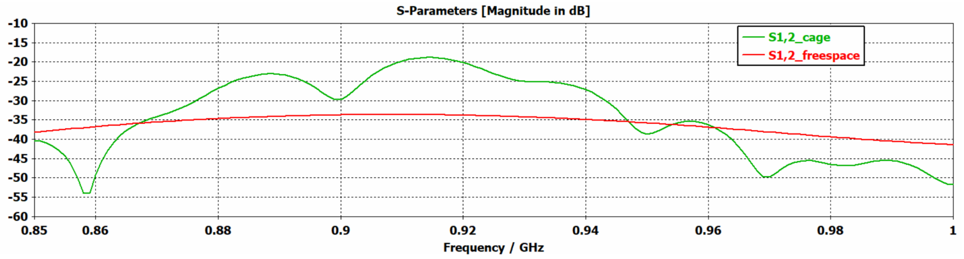

Figure 4.42: Transmission coefficients in free space and inside the cage

be inefficient in free space. Hence, for better performance, antennas should be designed according to the surrounding environment.

4.18 Conclusion

We presented a backscatter-based dual-band antenna system for the BCI device to be used with NHP's subjects. The goal of this work is to enable real-time data uplink from neuroscience experiments in freely behaving animals. In this chapter, two BCI antennas are proposed: a narrow-band ceramic antenna and a wide-band μSP antenna. The advantage of using a ceramic antenna is lower insertion loss between BCI and external antennas and that of a μSP antenna is wider bandwidth. Both the antennas were tested inside NHP cage using a saline solution-filled container.

Measurements with a saline tissue proxy at 126 surveyed locations inside an actual NHP cage indicated a typical 3 dB bandwidth of 6.56 MHz for ceramic antenna and 23.9 MHz for μSP antenna. The measured mean insertion loss for the ceramic antenna was 27.6 dB, 28.7 dB, and 37 dB for measurement planes 1,2, and 3, respectively. For μSP antenna the mean measured insertion loss was 33.9 dB, 33.3 dB, and 35 dB. The μSP antenna resulted in higher insertion loss as well as higher bandwidth as compared to the ceramic antenna. A higher bandwidth is required for higher data rates and large numbers of recording channels. The experimental results presented in Fig. 4.14 - 4.16 clearly show the presence of dense multipath inside the reverberate cavity environment of the metal animal cage. It is clear from these measurements that a system design assuming free-space propagation is doomed to be unreliable in a cage environment due to the deep nulls occurring only a few centimeters apart from each other. Cage experiments suggest that the bandwidth of the antenna depends highly on the location inside the cage. We found that insertion loss is higher inside the cage at the locations where the bandwidth is wider and lower where the bandwidth is smaller.

From the perspective of NHP animal safety, the simulated SAR values indicate that a carrier power of 10 dBm is safe for continuous exposure of the NHP animal subject. For our purposes, the 10 dBm carrier power level was sufficient to achieve the communication link quality goal and was comfortably within safe limits.

In-vivo recordings were performed with an anesthetized pigtail macaque in a benchtop-setup. All recording channels were uplinked successfully based on a backscatter communication to the external system with a data rate of the 25 Mbps from the μSP antenna and 6.25 Mbps data rate from the ceramic antenna.

CHAPTER 5

THESIS CONCLUSION AND FUTURE WORK

In this thesis, we presented innovative dual-band (HF and UHF (13.56 and 902–928 MHz)) antenna systems for wireless BCIs to enable short-range communication (over few millimeters between implanted and external systems) along with a capability of wireless charging. We have also presented antenna designs for head-stage BCI device to enable real-time neuroscience experiments on awake, freely moving animals.

To the best of my knowledge, the antenna designs presented in this work are the first dual-band (HF and UHF) co-planar antennas designed for wireless BCIs. In these devices, the HF band antennas are for powering the BCI system via inductive coupling and UHF band antennas are for data transfer based on backscatter communication. For the protection of biological tissue against implant PCB corrosion, the implant PCB was encapsulated inside biomedical grade silicone Dow Corning MDX4-4210. The encapsulation process was carefully done for void-free encapsulation which is required to prevent condensation inside the voids that can cause leakage current and corrosion. The detailed contributions presented in this thesis are mentioned in the next section.

5.1 Summary

- **Dual-band external and implant antenna system:** We designed, the first ever electrically-small dual-band co-planar HF and UHF (13.56 and 902–928 MHz) antenna system for implanted neural recording and/or stimulation devices. The implant diameter is 27 mm, and the thickness is 3 mm. The antenna is designed to be placed in the dura layer approximately 1 cm below the skin's surface. The external antenna, with a diameter of 85 mm and a thickness of 3 mm, is designed to be in close proximity (a few millimeters) from the skin's surface. The antennas are designed for the SAR below FCC limit defined for human exposure as well as for low port-to-port coupling between power and communication antennas.

  The antennas were tested using saline solution and with chicken muscle. We observed measurement results comparable to the simulation results. In saline solution, the measured power transfer efficiency in the HF band was 17 % when the distance between the external and the implant antenna was 1.5 cm. The maximum insertion loss at the UHF band in chicken muscle was 7 dB lower, as compared to saline tissue proxy, due to lower resistive losses in the protein and fat content of animal tissue as compared to a pure saline solution. Related work is published in [1] and in a patent [60].

- **Successful short distance WPT and backscatter communication using dual-band external and implant antenna system:** We achieved successful backscatter uplink at a data rate of 5 Mbps for an implant depth of 1 cm in saline solution. We expect a better communication link in animal tissue as compared to a saline solution. Related work is published in [61, 62].

- **Dual-band external and head-stage antennas for NHPs:** We designed the first ever dual-band (HF and UHF) co-planar BCI antenna devices for large NHPs located inside a metal housing cage, which acts as a reverberant chamber. The BCI antenna PCB is a two-layer board that is designed on a 5.5 cm diameter, 1.6 mm thick FR-4 dielectric. Related work is published in [63].

- **The first ever channel characterization inside a reverberant NHP cage:** We performed several experiments to understand the EM response inside the housing cage and to verify the behavior of the antennas in the cage environment. Inside the cage, we used a plastic container filled with a saline solution, to emulate tissue, instead of working with a live monkey. The cage side and head-stage antennas were chosen because of low SAR, as well as low port-to-port coupling between the HF and UHF systems.

  We found that the insertion loss and bandwidth varies from one location to another inside the cage, because of the variation in field distribution caused by the multipath. Experimental results presented in this work showed that backscatter communication using proposed antennas can perform well inside the volume of the reverberant cavity cage, despite the presence of significant multipath. Related work is published in [63].

- **A 6.26 Mbps and 25 Mbps backscatter uplink through *in-vivo* measurements with an anesthetized pigtail macaque using benchtop setup:** Neural recordings from 16 channels were successfully uplinked to the external system using proposed antennas with a maximum data rate of 25 Mbps. The distance between the external and head-stage antenna was 35 cm. Related work is published in [64] along with a paper under review [65].

5.2 Future Work

There can be numerous future improvements in the antenna design for wireless BCI systems.

5.2.1 Implantable BCI antennas

- **Need of implant packaging for long – term usage of implants** : In this work, we used bio-compatible silicone for the encapsulation of implants. It is essential to study various dielectric materials for packaging, with better material properties as that of silicone, to increase the lifetime of the proposed implantable device.
- **Methods for improving the bandwidth of the antennas for data rate ≈ 100 Mbps for real-time recording and stimulation** : Improvements in antenna design is needed for wider bandwidth without heating biological tissues.
- **Design of implant and external antennas using flexible material or WPT range improvement using flexible metamaterial lens** : The work can be continued for designing antennas on thin flexible material for the reduction of overall implant device size. WPT range can be improved by installing metamaterial lens between implant and external antennas similar to the work mentioned in [127].
- **Long – range communication and WPT over an entire room** : In this work, we showed the possibility of using wireless BCI systems based on backscatter communication for small – range communication of few centimeters between the implant and the external device. The practicability of implanted BCI systems for long distance (where the external antenna is located at a distance of a few meters from the implant antenna) WPT and communication is unknown and further study is required.

5.2.2 Antennas for NHP in a metal housing cage

- **BCI recording from an awake moving monkey inside metal housing cage** : In this thesis, we were able to record neural activity successfully using proposed antenna systems at a data rate of 25 Mbps, with an anesthetized macaque monkey, in a benchtop setup. The next step is to perform neural recording from a freely moving monkey inside its housing cage.

- **Methods for improving bandwidth of the antennas for higher data rate** : Further study is required for improving antennas for wider bandwidth.

- **Modification of cavity to achieve uniform field distribution inside the cage or use of multiple receiver antennas** : To ensure continuous neural recordings or stimulation and to avoid blind spots, an array of dual-band cage antennas can be designed so that each element has a switching capability relative to the position of the BCI antenna inside the cage, similar to the work mentioned in [114]. This switching capability for a cage array is an efficient way to reduce input power because only a few elements could be activated at a time instead of having the whole array always need to be on.

  Another method could be by installing a mechanical or electrical mode-stirrer inside the cage for homogeneous field distribution. This concept is commonly and effectively used in microwave ovens or reverberating chambers [128].

BIBLIOGRAPHY

[1] A. Sharma, E. Kampianakis, and M. S. Reynolds, “A dual-band HF and UHF antenna system for implanted neural recording and stimulation devices,” *IEEE Antennas and Wireless Propagation Letters*, vol. 16, pp. 493–496, 2017.

[2] Available at https://www.cst.com/Content/Events/UGM2007/05-Wittig.pdf.

[3] P. J. Dimbylow, “Fine resolution calculations of SAR in the human body for frequencies up to 3 GHz,” *Physics in Medicine and Biology*, vol. 47, no. 16, p. 2835, 2002.

[4] Z. Ahmad, “Polymer dielectric materials,” in *Dielectric Material.* InTech, 2012, ch. 01.

[5] Available at https://commons.wikimedia.org.

[6] Available at https://en.wikipedia.org/wiki/Southern pig-tailed macaque.

[7] F. J. Chaure., H. G. Rey, and R. Q. Quian, “A novel and fully automatic spike-sorting implementation with variable number of features,” *Journal of Neurophysiology*, vol. 120, no. 4, pp. 1859–1871, 2018.

[8] E. V. Evarts, “Temporal patterns of discharge of pyramidal tract neurons during sleep and waking in the monkey,” *Physiology*, vol. 27, no. 2, pp. 152–171, Mar. 1964.

[9] A. Jackson, J. Mavoori, and E. E. Fetz, “Correlations between the same motor cortex cells and arm muscles during a trained task, free behavior, and natural sleep in the Macaque monkey,” *Physiology*, vol. 97, no. 1, pp. 360–374, Jan. 2007.

[10] A. P. Georgopoulos, J. F. Kalaska, R. Caminiti, and J. T. Massey, “On the relations between the direction of two-dimensional arm movements and cell discharge in primate motor cortex,” *Journal of Neuroscience*, vol. 2, no. 11, pp. 1527–1537, 1982.

[11] P. D. Cheney and E. E. Fetz, “Functional classes of primate corticomotorneuronal cells and their relation to active force,” *Journal of Neurophysiology*, vol. 44, no. 4, pp. 773–791, 1980.

[12] T. N. Aflalo and M. S. A. Graziano, “Partial tuning of motor cortex neurons to final posture in a free-moving paradigm,” *Proceedings of the National Academy of Sciences of the United States of America*, vol. 103, no. 8, pp. 2909–2914, Feb. 2006.

[13] A. T. Tzallas, N. Giannakeas, K. N. Zoulis, M. G. Tsipouras, E. Glavas, K. D. Tzimourta, L. G. Astrakas, and S. Konitsiotis, “EEG classification and short-term epilepsy prognosis using brain computer interface software,” in *IEEE International Symposium on Computer-Based Medical Systems (CBMS)*, June 2017, pp. 349–353.

[14] M. Li and B. L. Lu, “Emotion classification based on gamma-band EEG,” in *2009 Annual International Conference of the IEEE Engineering in Medicine and Biology Society*, Sept 2009, pp. 1223–1226.

[15] A. Ferreira, R. L. Silva, W. C. Celeste, T. F. B. Filho, and M. S. Filho, “Human–machine interface based on muscular and brain signals applied to a robotic wheelchair,” *Journal of Physics: Conference Series*, vol. 90, no. 1, p. 012094, 2007.

[16] L. R. Hochberg, D. Bacher, B. Jarosiewicz, N. Y. Masse, J. D. Simeral, J. Vogel, and J. Donoghue, “Reach and grasp by people with tetraplegia using a neurally controlled robotic arm,” 2012, p. 372–375.

[17] P. A. Abhang, B. W. Gawali, and S. C. Mehrotra, *Introduction to EEG- and Speech-Based Emotion Recognition*, 1st ed. Orlando, FL, USA: Academic Press, Inc., 2016.

[18] J. Virkkala, R. Velin, S. L. Himanen, A. Varri, K. Muller, and J. Hasan, "Automatic sleep stage classification using two facial electrodes," in *2008 30th Annual International Conference of the IEEE Engineering in Medicine and Biology Society*, Aug 2008, pp. 1643–1646.

[19] P. Massotte and P. Cors, *Brain communication: telesympathy and telepathy*, 1st ed. Wiley-ISTE, 2015, ch. 12.

[20] R. Tadeusiewicz and P. Rotter, "From cochlear implants to brain-computer interfaces," in *Bio-Algorithms and Med-Systems BAMS*, vol. 8, 2012, pp. 267–286.

[21] R. Coffey, "Deep brain stimulation devices: a brief technical history and review," *Artifical Organs*, vol. 33, no. 33, pp. 208–220, 2009.

[22] T. Libery and E. E. Fetz, "Open-source, low cost, free-behavior monitoring, and reward system for neuroscience research in non-human primates," *Frontiers in Neuroscience*, vol. 11, p. 265, 2017.

[23] C. A. Chestek, V. Gilja, P. Nuyujukian, R. J. Kier, F. Solzbacher, S. I. Ryu, R. R. Harrison, and K. V. Shenoy, "Hermesc: low-power wireless neural recording system for freely moving primates," *IEEE Transactions on Neural Systems and Rehabilitation Engineering*, vol. 17, no. 4, pp. 330–338, Aug 2009.

[24] S. B. Lee, H. M. Lee, M. Kiani, U. Jow, and M. Ghovanloo, "An inductively powered scalable 32-channel wireless neural recording system-on-a-chip for neuroscience applications," *IEEE Transactions on Biomedical Circuits and Systems*, p. 360–371, 2010.

[25] M. Yin, D. A. Borton, J. Aceros, W. R. Patterson, and A. V. Nurmikko, “A 100-channel hermetically sealed implantable device for chronic wireless neurosensing applications,” *IEEE Trans. Biomed. Circuits Syst.*, vol. 7, no. 2, pp. 115–128, April 2013.

[26] M. Zargham and P. G. Gulak, “Maximum achievable efficiency in near-field coupled power-transfer systems,” *IEEE Transactions on Biomedical Circuits and Systems*, vol. 6, no. 3, pp. 228–245, June 2012.

[27] A. S. Y. Poon, S. O’Driscoll, and T. H. Meng, “Optimal frequency for wireless power transmission into dispersive tissue,” *IEEE Transactions on Antennas and Propagation*, vol. 58, no. 5, pp. 1739–1750, May 2010.

[28] X. Shi, B. H. Waters, and J. R. Smith, “SAR distribution for a strongly coupled resonant wireless power transfer system,” in *IEEE Wireless Power Transfer Conference (WPTC)*, May 2015, pp. 1–4.

[29] S. J. Thomas and M. S. Reynolds, “A 96 Mbit/sec, 15.5 pJ/bit 16-QAM modulator for UHF backscatter communication,” in *Proc. 2012 IEEE Intl. Conf. RFID (RFID)*, Apr. 2012, pp. 185–190.

[30] J. F. Ensworth and M. S. Reynolds, “Every smart phone is a backscatter reader: Modulated backscatter compatibility with Bluetooth 4.0 Low Energy (BLE) devices,” in *Proc. 2015 IEEE Intl. Conf. RFID (RFID 15)*, 2015.

[31] D. Seo, R. M. Neely, K. Shen, U. Singhal, E. Alon, J. M. Rabaey, J. M. Carmena, and M. M. Maharbiz, “Wireless recording in the peripheral nervous system with ultrasonic neural dust,” *Neuron*, vol. 91, no. 3, pp. 529–539, 2016.

[32] A. Ebrazeh and P. Mohseni, “30 pJ/b, 67 Mbps, centimeter-to-meter range data telemetry with an IR-UWB wireless link,” *IEEE Transactions on Biomedical Circuits and Systems*, vol. 9, no. 3, pp. 362–369, June 2015.

[33] E. Moradi, S. Amendola, T. Björninen, L. Sydänheimo, J. M. Carmena, J. M. Rabaey, and L. Ukkonen, “Backscattering neural tags for wireless brain-machine interface systems,” *IEEE Transactions on Antennas and Propagation*, vol. 63, no. 2, pp. 719–726, Feb 2015.

[34] T. Bjorninen, R. Muller, P. Ledochowitsch, L. Sydanheimo, L. Ukkonen, M. M. Maharbiz, and J. M. Rabaey, “Design of wireless links to implanted brain-machine interface microelectronic systems,” *IEEE Antennas and Wireless Propagation Letters*, vol. 11, pp. 1663–1666, 2012.

[35] Available at https://en.wikipedia.org/wiki/Specific absorption rate.

[36] E. Tanghe, W. Joseph, L. Martens, H. Capoen, K. V. Herwegen, and W. Vantomme, “Large-scale fading in industrial environments at wireless communication frequencies,” in *IEEE Antennas and Propagation Society International Symposium*, June 2007, pp. 3001–3004.

[37] T. S. Rappaport, “Characterization of UHF multipath radio channels in factory buildings,” *IEEE Transactions on Antennas and Propagation*, vol. 37, no. 8, pp. 1058–1069, Aug 1989.

[38] A. A. M. Saleh and R. Valenzuela, “A statistical model for indoor multipath propagation,” *IEEE Journal on Selected Areas in Communications*, vol. 5, no. 2, pp. 128–137, February 1987.

[39] S. Y. Seidel and T. S. Rappaport, “914 MHz path loss prediction models for indoor wireless communications in multifloored buildings,” *IEEE Transactions on Antennas and Propagation*, vol. 40, no. 2, pp. 207–217, Feb 1992.

[40] S. B. Lee, M. Yin, J. R. Manns, and M. Ghovanloo, “A wideband dual-antenna receiver for wireless recording from animals behaving in large arenas,” *IEEE Transactions on Biomedical Engineering*, vol. 60, no. 7, pp. 1993–2004, July 2013.

[41] O. Knecht, R. Bosshard, and J. W. Kolar, “High-efficiency transcutaneous energy transfer for implantable mechanical heart support systems,” *IEEE Transactions on Power Electronics*, vol. 30, no. 11, pp. 6221–6236, Nov 2015.

[42] U. M. Jow and M. Ghovanloo, “Design and optimization of printed spiral coils for efficient transcutaneous inductive power transmission,” *IEEE Transactions on Biomedical Circuits and Systems*, vol. 1, no. 3, pp. 193–202, Sept 2007.

[43] M. Kiani and M. Ghovanloo, “An RFID-based closed-loop wireless power transmission system for biomedical applications,” *IEEE Transactions on Circuits and Systems II: Express Briefs*, vol. 57, no. 4, pp. 260–264, April 2010.

[44] M. Zargham and P. G. Gulak, “A 0.13 μm CMOS integrated wireless power receiver for biomedical applications,” in *Proceedings of the ESSCIRC (ESSCIRC)*, Sept 2013, pp. 137–140.

[45] T. Björninen, R. Muller, P. Ledochowitsch, L. Sydänheimo, L. Ukkonen, and J. Rabaey, “Antenna design for wireless electrocorticography,” in *Proceedings of the 2012 IEEE International Symposium on Antennas and Propagation*, July 2012, pp. 1–2.

[46] L. Song and Y. Rahmat-Samii, "An end-to-end implanted brain-machine interface antenna system performance characterizations and development," *IEEE Transactions on Antennas and Propagation*, vol. 65, no. 7, pp. 3399–3408, July 2017.

[47] S. D. O'Driscol, "A mm-sized implantable power receiver with adaptive matching," in *IEEE Sensors*, Nov 2010, pp. 83–88.

[48] H. Bahrami, S. A. Mirbozorgi, R. Ameli, L. A. Rusch, and B. Gosselin, "Flexible, polarization-diverse UWB antennas for implantable neural recording systems," *IEEE Transactions on Biomedical Circuits and Systems*, vol. 10, no. 1, pp. 38–48, Feb 2016.

[49] Y. Liu, Y. Chen, H. Lin, and F. H. Juwono, "A novel differentially fed compact dual-band implantable antenna for biotelemetry applications," *IEEE Antennas and Wireless Propagation Letters*, vol. 15, pp. 1791–1794, 2016.

[50] Z. Duan, Y. X. Guo, M. Je, and D. L. Kwong, "Design and in vitro test of a differentially fed dual-band implantable antenna operating at MICS and ISM bands," *IEEE Transactions on Antennas and Propagation*, vol. 62, no. 5, pp. 2430–2439, May 2014.

[51] D. J. Young, "Wireless powering and data telemetry for biomedical implants," in *Annual International Conference of the IEEE Engineering in Medicine and Biology Society*, Sept 2009, pp. 3221–3224.

[52] R. Muller, H. P. Le, W. Li, P. Ledochowitsch, S. Gambini, T. Bjorninen, A. Koralek, J. M. Carmena, M. M. Maharbiz, E. Alon, and J. M. Rabaey, "A minimally invasive 64-channel wireless uECoG implant," *IEEE Journal of Solid-State Circuits*, vol. 50, no. 1, pp. 344–359, Jan 2015.

[53] C. S. Mestais, G. Charvet, F. Sauter-Starace, M. Foerster, D. Ratel, and A. L. Benabid, "WIMAGINE: Wireless 64-channel ECoG recording implant for long term clinical applications," *IEEE Transactions on Neural Systems and Rehabilitation Engineering*, vol. 23, no. 1, pp. 10–21, Jan 2015.

[54] R. Das and H. Yoo, "A multiband antenna associating wireless monitoring and non-leaky wireless power transfer system for biomedical implants," *IEEE Transactions on Microwave Theory and Techniques*, vol. 65, no. 7, pp. 2485–2495, July 2017.

[55] V. Talla, V. Ranganathan, B. Mahoney, and J. R. Smith, "Dual band wireless power and bi-directional data link for implanted devices in 65 nm CMOS," in *2016 IEEE International Symposium on Circuits and Systems (ISCAS)*, May 2016, pp. 658–661.

[56] G. Simard, M. Sawan, and D. Massicotte, "High-speed OQPSK and efficient power transfer through inductive link for biomedical implants," *IEEE Transactions on Biomedical Circuits and Systems*, vol. 4, no. 3, pp. 192–200, June 2010.

[57] D. Yeager, W. Biederman, N. Narevsky, E. Alon, and J. Rabaey, "A fully-integrated 10.5uw miniaturized (0.125mm2) wireless neural sensor," in *2012 Symposium on VLSI Circuits (VLSIC)*, June 2012, pp. 72–73.

[58] L. Jinliang, D. Qijun, H. Wenshan, and Z. Hong, "Research on quality factor of the coils in wireless power transfer system based on magnetic coupling resonance," in *2017 IEEE PELS Workshop on Emerging Technologies: Wireless Power Transfer (WoW)*, May 2017, pp. 123–127.

[59] M. S. Chae, Z. Yang, M. R. Yuce, L. Hoang, and W. Liu, "A 128-channel 6 mW wireless neural recording IC with spike feature extraction and UWB transmitter," *IEEE Transac-*

tions on Neural Systems and Rehabilitation Engineering, vol. 17, no. 4, pp. 312–321, Aug 2009.

[60] A. Sharma, E. Kampianakis, and M. S. Reynolds, "Antenna Elements, Implanted Devices, and Systems for Communication With Implanted Devices," *International patent application number PCT/US2017/016573*, 2017.

[61] E. Kampianakis, A. Sharma, J. Arenas, and M. S. Reynold, "A dual-band wireless power transfer and backscatter communication approach for real-time neural/EMG data acquisition," *IEEE Journal of Radio Frequency Identification*, vol. 1, no. 1, pp. 100–107, March 2017.

[62] E. Kampianakis, A. Sharma, J. Arenas, and M. S. Reynolds, "A dual-band wireless power transfer and backscatter communication approach for implantable neuroprosthetic devices," in *2017 IEEE International Conference on RFID (RFID)*, May 2017, pp. 67–72.

[63] A. Sharma, E. Kampianakis, J. Rosenthal, A. Pike, A. Dadkhah, and M. S. Reynolds, "Wideband UHF DQPSK backscatter communication in reverberant cavity animal cage environments," *IEEE Transactions on Antennas and Propagation*, pp. 1–1, 2019.

[64] J. Rosenthal, , A. Sharma, E. Kampianakis, and M. S. Reynolds, "A 6.25 mbps, 12.4 pj/bit DQPSK backscatter wireless uplink for the neurodisc brain-computer interface," in *2018 IEEE Biomedical Circuits and Systems Conference (BioCAS)*, Oct 2018, pp. 1–4.

[65] J. Rosenthal, A. Sharma, E. Kampianakis, and M. S. Reynolds, "A 25 Mbps, 12.4 pJ/bit backscatter data uplink for the neurodisc brain computer interface," *IEEE Transactions on Biomedical Circuits and Systems*, Under Review.

[66] S. Cruciani, V. D. Santis, M. Feliziani, and F. Maradei, "Cole-Cole vs Debye models for the assessment of electromagnetic fields inside biological tissues produced by wideband EMF sources," in *2012 Asia-Pacific Symposium on Electromagnetic Compatibility*, May 2012, pp. 685–688.

[67] P. Staebler, *Human Exposure to Electromagnetic Fields: From Extremely Low Frequency (ELF) to Radiofrequency*, 4th ed. ISTE, Limited, 2017.

[68] Z. P. Aguilar, "Chapter 7 - nanopharmacology," in *Nanomaterials for Medical Applications*, 1st ed. Elsevier, 2012, pp. 293 – 360.

[69] S. Drabowitch, A. Papiernik, H. Griffiths, J. Encinas, and B. Smith, in *Modern Antennas*, 2nd ed. Springer US, 2005, p. 677.

[70] B. Greenebaum, *Bioengineering and Biophysical Aspects of Electromagnetic Fields*, 4th ed. CRC Press, 2018.

[71] O. P. Gandhi, "State of the knowledge for electromagnetic absorbed dose in man and animals," *Proceedings of the IEEE*, vol. 68, no. 1, pp. 24–32, Jan 1980.

[72] J. C. Lin, *Electromagnetic field in biological systems*, 1st ed. CRC press, 2011.

[73] S. Wiak, A. Krawczyk, and M. Trlep, *Computer Engineering in Applied Electromagnetism*, 1st ed. Springer, 2005.

[74] D. M. Pozar, *Microwave engineering; 3rd ed.* Hoboken, NJ: Wiley, 2005.

[75] Z. Zakaria, R. R. Abdul, M. Mansor, S. Yaacob, N. M. Ayub, S. Z. Muji, M. H. Rahiman, and S. M. Aman, "Advancements in transmitters and sensors for biological tissue imaging in magnetic induction tomography," *Sensors (Basel)*, vol. 12, no. 6, pp. 7126–7156, 2012.

[76] R. Bansal, *Fundamentals of Engineering Electromagnetics*, 1st ed. CRC press, 2006.

[77] D. Voltmer, *Fundamentals of Electromagnetics 2: Quasistatics and Waves.* Morgan and Claypool, 2007. [Online]. Available: https://ieeexplore.ieee.org/document/6812558

[78] C. Polk and E. Postow, *Handbook of Biological Effects of Electromagnetic Fields*, 2nd ed. CRC press, 1996.

[79] S. Gabriel, R. W. Lau, and C. Gabriel, "The dielectric properties of biological tissues: III. parametric models for the dielectric spectrum of tissues," *Physics in Medicine and Biology*, vol. 41, no. 11, pp. 2271–2293, Nov 1996.

[80] K. S. Cole and R. H. Cole, "Dispersion and absorption in dielectrics 1. alternating current characteristics," *Journal of Chemical Physics*, April 1941.

[81] A. V. Vorst, A. Rosen, and Y. Kotsuka, "RF/microwave interaction with biological tissues," *John Wiley and Sons, Inc.*, 2006.

[82] P. R. Wainwright, "Localized specific absorption rate calculations in a realistic phantom leg at 1–30 MHz using a finite element method," in *Physics in Medicine and Biology*, vol. 4, 1998, pp. 1041–1052.

[83] S. Gabriel, R. Lau, and C. Gabriel, "The dielectric properties of biological tissues: I. literature survey," *Phys. Med. Biol., vol. 41, no. 11, pp. 2231–2249, Nov. 1996.*

[84] C. Gabriel, *Compilation of the Dielectric Properties of Body Tissues at RF and Microwave Frequencies.* Texas: Air Force material command, Brooks Air Force Base, 02 1996.

[85] X. Li, *Body Matched Antennas for Microwave Medical Applications.* Dissertation, Karlsruher Institut für Technologie (KIT), 2013.

[86] Dielectric properties of body tissues. [Online]. Available: http://niremf.ifac.cnr.it/tissprop/

[87] A. Stogryn, “Equations for calculating the dielectric constant of saline water (correspondence),” *IEEE Transactions on Microwave Theory and Techniques*, vol. 19, no. 8, pp. 733–736, Aug 1971.

[88] C. G. Malmberg and A. A. Maryott, “Dielectric constant of water from 0 to 1000 C,” *Journal of Research of the National Bureau of Standards*, vol. 56, no. 1, Jan 1956.

[89] E. Grant, T. Buchanan, and H. Cook, “Dielectric behavior of water at microwave frequencies,” *J. Chem. Phys.*, vol. 26, pp. 156–161, 1957.

[90] J. S. Besnoff and M. S. Reynolds, “Single-wire RF transmission lines for implanted devices,” in *2013 IEEE Biomedical Circuits and Systems Conference (BioCAS)*, Oct 2013, pp. 222–225.

[91] CST microwave studio simulation of a SAM phantom head model with mobile phone. [Online]. Available: https://www.cst.com/solutions/article/cst-microwave-studio-simulation-of-a-sam-phantom-head-model-with-mobile-phone

[92] J. Kim and Y. Rahmat-Samii, “Implanted antennas inside a human body: simulations, designs, and characterizations,” *IEEE Transactions on Microwave Theory and Techniques*, vol. 52, no. 8, pp. 1934–1943, Aug 2004.

[93] Hugo human body model. [Online]. Available: https://www.cst.com/solutions/article/hugo-human-body-model

[94] A. Christ, W.Kainz, E. G. Hahn, K. Honegger, M. Zefferer, E. Neufeld, W. Rascher, R. Janka, W. Bautz, and J. Chen, “The virtual family—development of surface-based anatomical

models of two adults and two children for dosimetric simulations," *Physics in Medicine and Biology*, vol. 55, no. 2, pp. N23–N38, dec 2009.

[95] H. Sun, T. M. Blakely, F. Darvas, J. D. Wander, L. A. Johnson, D. K. Su, K. J. Miller, E. E. Fetz, and J. G. Ojemann, "Sequential activation of premotor, primary somatosensory and primary motor areas in humans during cued finger movements," *Clinical Neurophysiology*, vol. 126, no. 11, pp. 2150–2161, Nov 2015.

[96] M. Patel and J. Wang, "Applications, challenges, and prospective in emerging body area networking technologies," *IEEE Wireless Communications*, vol. 17, no. 1, pp. 80–88, February 2010.

[97] E. Riggio, I. Ardoino, C. E. Richardson, and E. Biganzoli, "Predictability of anthropomorphic measurements in implant selection for breast reconstruction: a retrospective cohort study," *European Journal of Plastic Surgery*, p. 203–212, Jan. 2017.

[98] M. S. Chae, Z. Yang, M. R. Yuce, L. Hoang, and W. Liu, "A 128-channel 6 mW wireless neural recording IC with spike feature extraction and UWB transmitter," *IEEE Transactions on Neural Systems and Rehabilitation Engineering*, vol. 17, no. 4, pp. 312–321, Aug 2009.

[99] B. Yarman, *Design of Ultra Wideband Antenna Matching Networks: Via Simplified Real Frequency Technique*. Springer, 2008.

[100] W. Stutzman and G.A.Thiele, *Antenna Theory and Design*, 3rd ed. John Wiley and Sons, Inc., May 2012.

[101] Y. Joung, "Development of Implantable Medical Devices: From an Engineering Perspective," *International Neurourology Journal*, p. 98–106, Sept. 2013.

[102] T. Stöver and T. Lenarz, “Biomaterials in cochlear implants,” *GMS Current Topics in Otorhinolaryngology, Head and Neck Surgery*, 2009.

[103] H. Dinis, I. Colmiais, and P. Mendes, “Extending the limits of wireless power transfer to miniaturized implantable electronic devices,” *Micromachines*, vol. 8, no. 12, 2017.

[104] A. P. Sample, D. T. Meyer, and J. R. Smith, “Analysis, experimental results, and range adaptation of magnetically coupled resonators for wireless power transfer,” *IEEE Transactions on Industrial Electronics*, vol. 58, no. 2, pp. 544–554, Feb 2011.

[105] J. Garnica, R. A. Chinga, and J. Lin, “Wireless power transmission: From far field to near field,” *Proceedings of the IEEE*, vol. 101, no. 6, pp. 1321–1331, June 2013.

[106] P. V. Nikitin and K. V. S. Rao, “Theory and measurement of backscattering from RFID tags,” *IEEE Antennas and Propagation Magazine*, vol. 48, no. 6, pp. 212–218, Dec 2006.

[107] R. C. Hansen, “Relationships between antennas as scatterers and as radiators,” *Proceedings of the IEEE*, vol. 77, no. 5, pp. 659–662, May 1989.

[108] P. V. Nikitin, K. V. S. Rao, and R. D. Martinez, “Differential RCS of RFID tag,” *Electronics Letters*, vol. 43, no. 8, pp. 431–432, April 2007.

[109] A. Sharma, A. Pedross-Engel, D. Arnitz, C. M. Watts, D. R. Smith, and M. S. Reynolds, “A K-band backscatter fiducial for continuous calibration in coherent millimeter-wave imaging,” *IEEE Transactions on Microwave Theory and Techniques*, vol. 66, no. 1, pp. 431–438, Jan 2018.

[110] J. D. Griffin and G. D. Durgin, “Complete link budgets for backscatter-radio and RFID systems,” *IEEE Antennas and Propagation Magazine*, vol. 51, no. 2, pp. 11–25, April 2009.

[111] M. Mark, T. Björninen, L. Ukkonen, L. Sydänheimo, and J. M. Rabaey, “SAR reduction and link optimization for mm-size remotely powered wireless implants using segmented loop antennas,” in *2011 IEEE Topical Conference on Biomedical Wireless Technologies, Networks, and Sensing Systems*, Jan 2011, pp. 7–10.

[112] C. Goodman, V. Cohen, J. Thornby, and D. Netscher, “The life span of silicone gel breast implants and a comparison of mammography, ultrasonography, and magnetic resonance imaging in detecting implant rupture: a meta-analysis.” *Annals of Plastic Surgery*, vol. 41, no. 2, pp. 577–586, December 1998.

[113] P. E. K. Donaldson, “Hydrothermal stability of joints, using a silicone robber adhesive, for a range of adherends of interest to makers of surgically-implanted microelectronic devices,” *International Journal of Adhesion and Adhesives*, vol. 14, no. 2, April 1994.

[114] X. Shi and J. R. Smith, “Large area wireless power via a planar array of coupled resonators,” in *2016 International Workshop on Antenna Technology (iWAT)*, Feb 2016, pp. 200–203.

[115] S. J. Thomas, R. R. Harrison, A. Leonardo, and M. S. Reynolds, “A battery-free multichannel digital neural/EMG telemetry system for flying insects,” *IEEE Trans. Biomed. Circuits Syst.*, vol. 6, no. 5, pp. 424–436, Oct 2012.

[116] R. Passingham, “How good is the macaque monkey model of the human brain?” *Current Opinion in Neurobiology*, p. 6–11, Feb. 2009.

[117] C. Jacobsen, “Functions of frontal association area in primates,” *Archives of Neurology and Psychiatry*, vol. 33, no. 3, pp. 558–569, 1935.

[118] S. Zanos, A. G. Richardson, L. Shupe, F. P. Miles, and E. E. Fetz, “The Neurochip-2: an autonomous head-fixed computer for recording and stimulating in freely behaving monkeys,” *IEEE Trans. Neural Syst. Rehabil. Eng.*, vol. 19, no. 4, pp. 427–435, 2011.

[119] J. D. Griffin and G. D. Durgin, “Complete link budgets for backscatter-radio and rfid systems,” *IEEE Antennas and Propagation Magazine*, vol. 51, no. 2, pp. 11–25, April 2009.

[120] Available at https://www.lairdtech.com/products/s9028pcr.

[121] Available at https://www.wibotic.com/.

[122] Available at https://www.comtest.eu/components/mode-stirring-systems/.

[123] D. A. Hill. IEEE, 2009. [Online]. Available: https://ieeexplore.ieee.org/document/5396536

[124] T. Fromenteze, O. Yurduseven, F. M. Imani, J. Gollub, C. Decroze, D. Carsenat, and D. R. Smith, “Computational imaging using a mode-mixing cavity at microwave frequencies,” *Applied Physics Letters*, vol. 106, no. 19, p. 194104, 2015.

[125] Q. Xu and Y. Huang, *Applications in the Reverberation Chamber.* IEEE, 2018, pp. 185–282. [Online]. Available: https://ieeexplore.ieee.org/document/8538867

[126] Available at https://linxtechnologies.com/wp/product/sp series splatch antennas/ .

[127] A. Rajagopalan, A. K. RamRakhyani, D. Schurig, and G. Lazzi, “Improving power transfer efficiency of a short-range telemetry system using compact metamaterials,” *IEEE Transactions on Microwave Theory and Techniques*, vol. 62, no. 4, pp. 947–955, April 2014.

[128] M. Vollmer, “Physics of the microwave oven,” *Physics Education*, vol. 39, no. 1, p. 74, 2004.

Biography

Apoorva received the Ph.D. degree in Electronics and Computer Engineering from University of Washington in April 2019, M.Sc (tech) degree from International Institute of Information Technology Hyderabad India (IIIT-H) in 2011, and B.Tech degree in Electronics and Communication Engineering from Galgotias College of Engineering and Technology (GCET) India in 2009. From 2011 to 2013, she was working at Computer Simulation Technology (CST), India, where she held the position of Application Engineer and was responsible for technical support and benchmarks for CST Microwave Studio, Cable Studio, Particle Studio and Design Studio software. She also worked on improving the database of Antenna Magus.

While working on the Ph.D degree, Apoorva won a brainpower student competition award, was nominated for a best paper award, and won a best poster award. Apoorva worked at Google, Chicago for four months as an intern on the Pixel team, where she worked on designing, prototyping, and testing of GPS and MIMO antennas for a modern cellular handset. From 2018 to 2019, Apoorva worked part-time in Facebook as a surface wave designer. Till date, Apoorva has authored eight published journal articles, one journal currently under review, published six peer-reviewed conference proceedings articles, and submitted three patents. Her research interests include modeling and optimization techniques for RF devices, electromagnetics, antenna designs and biomedical devices.